uOttawa

L'Université canadienne
Canada's university

FACULTÉ DES ÉTUDES SUPÉRIEURES ET POSTOCTORALES

uOttawa

L'Université canadienne
Canada's university

FACULTY OF GRADUATE AND POSDOCTORAL STUDIES

Christopher C. Squires
AUTEUR DE LA THÈSE / AUTHOR OF THESIS

M.A.Sc. (Electrical and Computer Engineering)
GRADE / DEGREE

School of Information Technology and Engineering
FACULTÉ, ÉCOLE, DÉPARTEMENT / FACULTY, SCHOOL, DEPARTMENT

The Impact of Polarized MIMO Channels in Vehicular Based Communications
TITRE DE LA THÈSE / TITLE OF THESIS

C. D'Amours
DIRECTEUR (DIRECTRICE) DE LA THÈSE / THESIS SUPERVISOR

T. Willink
CO-DIRECTEUR (CO-DIRECTRICE) DE LA THÈSE / THESIS CO-SUPERVISOR

A. Yongacoglu

R. Hafez

Gary W. Slater
Le Doyen de la Faculté des études supérieures et postdoctorales / Dean of the Faculty of Graduate and Postdoctoral Studies

The Impact of Polarized MIMO Channels in Vehicular Based Communications

by

Christopher C. Squires

Thesis submitted to the
Faculty of Graduate and Postdoctoral Studies
in partial fulfillment of the requirements for the degree of
Master of Applied Science
in
Electrical and Computer Engineering

Ottawa-Carleton Institute for Electrical and Computer Engineering
Faculty of Engineering
School of Information Technology and Engineering
University of Ottawa

Your file Votre référence
ISBN: 978-0-494-65500-9
Our file Notre référence
ISBN: 978-0-494-65500-9

Abstract

Measurements of orthogonally polarized MIMO channels were conducted in downtown Ottawa with dual-polarized receive array elements positioned along the sides of a measurement vehicle. The measured channel data are used to analyze characteristics of the polarized channel including the angular distribution of received power, diversity, correlation and cross-polarization discrimination. It is shown that if spatially separated antennas are replaced with dual-polarized elements the cross-polarization discrimination results in a performance loss that is partially compensated for by improved cross-polar correlation characteristics. Further, it is observed that the locations of the array elements at the mobile has a significant impact on the channel characteristics measured. In areas where the received signal energy is highly directional, the orientation of the vehicle with respect to the location of the transmitter often results in channels with characteristics which are significantly different from one side of the mobile to the other. This is further influenced by the presence (or lack thereof) of buildings, which can act as reflective signal sources for elements of the array shadowed by the vehicle.

Acknowledgements

First and foremost, I would like to thank Dr. Tricia Willink, my supervisor at Communications Research Centre. As both a graduate student and professional, her encouragement, patience and advice has provided me with the confidence and drive to see this thesis through to completion. Without her support I may never have reached this point.

I would also like to thank Dr. Claude D'Amours, my academic supervisor at University of Ottawa, for the advice and support offered both before and after enrolling in the graduate studies program.

Further, I would like to express my appreciation to the CRC for providing me the opportunity to work and learn in an environment where the pursuit of knowledge and personal development is valued so highly. The many discussions held with the great people of CRC has laid the foundation for much of the work presented within this thesis. I would also like to acknowledge the CRC for providing both financial support and access to measurement equipment and data, without which this thesis would be much less than what it is.

Contents

List of Figures

List of Tables

List of Abbreviations

A/D	Analog to digital converter.
AOA	Angle of arrival.
API	Array power imbalance.
AWGN	Additive white Gaussian noise.
BER	Bit error rate.
cdf	Cumulative distribution function.
CRC-MCS	Communications Research Centre MIMO channel sounder.
D/A	Digital to analog converter.
DSA	Driver side array.
FPGA	Field programmable gate array.
EM	Electromagnetic.
GUI	Graphical user interface.
GPS	Global positioning system.
HP	Horizontal polarization.
HP-DSA	Horizontally polarized driver side array.
HP-PSA	Horizontally polarized passenger side array.
I & Q	In-phase and quadrature.
IF	Intermediate frequency.
IL	Insertion loss.
IR	Impulse response.
LNA	Low noise amplifier.
LOS	Line of sight.
LO	Local oscillator.
MIMO	Multiple input multiple output.
MISO	Multiple input single output.
MMSE	Minimum mean squared error.
MVDR	Minimum variance distortionless response.
NLOS	Non-line of sight.

OSTBC	Orthogonal space time block code.
PSA	Passenger side array.
QPSK	Quadrature phase shift keying.
SIMO	Single input multiple output.
SISO	Single input single output.
SM	Spatial multiplexing.
SNR	Signal to noise ratio.
V-BLAST	Vertical Bell Labs layered space time.
VP	Vertical polarization.
VP-DSA	Vertically polarized driver side array.
VP-PSA	Vertically polarized passenger side array.
VH-DSA	Vertically\Horizontally polarized driver side array.
VH-PSA	Vertically\Horizontally polarized passenger side array.
XPD	Cross polarization diversity.
ZF	Zero forcing.

List of Symbols

$E\{\cdot\}$	Expected value.
$\|\cdot\|_F$	Frobenius norm.
$det[\cdot]$	Determinant.
$\{\cdot\}^\dagger$	Hermitian.
$tr\{\cdot\}$	Trace.
N	Number of transmit elements.
M	Number of receive elements.
λ	Frequency wavelength.
α^V	VP channel coefficient.
α^H	HP channel coefficient.
$\mathbf{H}$	MIMO channel matrix.
$\mathbf{H}^V$	VP MIMO channel matrix.
$\mathbf{H}^H$	HP MIMO channel matrix.
$\mathbf{H}_d^V$	VP-DSA MIMO channel matrix.
$\mathbf{H}_d^H$	HP-DSA MIMO channel matrix.
$\mathbf{H}_p^V$	VP-PSA MIMO channel matrix.
$\mathbf{H}_p^H$	HP-PSA MIMO channel matrix.
$\mathbf{H}_d^{VH}$	VH-DSA MIMO channel matrix.
$\mathbf{H}_p^{VH}$	VH-PSA MIMO channel matrix.
ρ	Correlation coefficient.
$\mathbf{R}_{rx}$	Correlation matrix at the receiver.
$\mathbf{R}_{tx}$	Correlation matrix at the transmitter.
$\mathbf{R}_{MIMO}$	Complete MIMO correlation matrix.
$\mathbf{U}$	Matrix of eigenvectors.
$\mathbf{\Sigma}$	Diagonal matrix of eigenvalues.
σ^2	Eigenvalue.
$\mathbf{I}_M$	$M \times M$ identity matrix.
γ	Signal to noise ratio.

N_o	Noise variance.
C	Capacity.
$\bar{P}^V$	VP total received power.
$\bar{P}^H$	HP total received power.
P_d^V	VP-DSA total received power.
P_d^H	HP-DSA total received power.
P_p^V	VP-PSA total received power.
P_p^H	HP-PSA total received power.
XPD^V	XPD with respect to the VP.
XPD^H	XPD with respect to the HP.
$\hat{\mu}_{XPD}$	Mean of the XPD.
$\hat{\sigma}^2_{XPD}$	Variance of the XPD.
D^V	VP channel diversity.
D^H	HP channel diversity.
API^V	VP array power imbalance.
API^H	HP array power imbalance.

Chapter 1

Introduction

In multiple-input multiple-output (MIMO) communication systems, multielement antenna arrays are used at the transmitter and receiver to exploit diversity in order to increase data throughput and/or improve robustness to signal fading. When the fading characteristics at each array element are uncorrelated the diversity is maximized. Typically, this is realized by spatially separating elements of the array antennas. When the environment is rich in multipath, an element spacing of as little as half the signal wavelength may be adequate [1]. However, in order to achieve adequate levels of diversity in environments in which the angular spread of arriving multipath is small, a larger spacing between elements is required. As a result, the physical size of the antenna arrays can prove to be a practical limitation for the implementation of diversity systems, especially when the frequency is low or the device size is very small.

In vehicular communications systems, the impact of the array size as well as the arrangement of antennas at the mobile is of particular concern. MIMO channels become decorrelated when multipath components are received from all directions. This requires an antenna placement that maximizes the effective aperture of each antenna, avoiding any obstruction of the multipath components by the vehicle. However, in reality the location of array elements may be constrained by practical considerations ranging from aesthetics, in personal vehicles, to limitations resulting from the physical nature of the vehicle itself, in military or emergency response vehicles for example.

An alternative method to spatial diversity is polarization diversity. Polarization diversity exploits the multidimensional nature of electromagnetic wave propagation under the assumption that orthogonally polarized signals will be uncorrelated [2]. Hypothetically, this would allow a single dual-polarized antenna to replace two spatially separated antennas, reducing the overall size of the array and increasing the flexibility in which the elements of the array at the vehicle are positioned.

In this thesis, the performance of a vehicular mounted, dual-polarized MIMO system

is investigated. Measurements of polarized MIMO channels were performed in urban environments with dual-polarized elements of the receive array mounted along each side of the measurement vehicle. In many environments, the positioning of the array elements in this manner had considerable impact on the characteristics and performance of the polarized MIMO channels measured. Although, from a propagation point of view, the choice of array locations may not be ideal, the analysis of these channels provides useful insight into the impact of array location on vehicular MIMO communications.

1.1 MIMO Overview

Traditional single-input single-output (SISO) wireless communications systems, so named for their single transmit and receive antennas, often experience a significant performance degradation from multipath fading. Multipath fading is caused by the deconstructive combination of phase-delayed signal components and can often result in large reductions in the signal-to-noise ratio (SNR) at the receiver. The effects of fading can be combated using multielement arrays (MEAs) at either the transmitter, i.e., multiple-input single-output (MISO) systems, or at the receiver, i.e., single-input multiple-output (SIMO) systems. These systems exploit some form of diversity to improve performance of the wireless link [3]. However, when multiple element antennas are employed at the transmitter and receiver, the potential for both improving the system performance [4] and increasing data throughput is considerable [5]. These systems are commonly referred to as multiple-input multiple-output (MIMO) systems.

1.1.1 MIMO Channel Model

A typical MIMO system, as illustrated in Figure 1.1, exploits some manner of diversity using transmit and receive array antennas with N and M elements, respectively. At the transmitter, different signals are radiated from each array element simultaneously and in the same frequency bandwidth. As the signals propagate through the wireless channel they are scattered and reflected by physical objects within the environment which results in the creation of multipath components at the receiver. The multipath components are attenuated and phase-shifted replicas of the original transmitted signals, corrupted by interference and noise. Each element of the receive array sums the multipath contributions from each of the N transmitter elements. The resulting received signal vector $\mathbf{r}(t)$ at time t is given by

$$\mathbf{r}(t) = \mathbf{H}(t)\mathbf{s}(t) + \mathbf{n}(t), \tag{1.1}$$

where $\mathbf{n}(t)$ is a zero-mean complex additive white Gaussian noise (AWGN) vector with variance N_o and $\mathbf{s}(t)$ is the vector of transmitted symbols. The channel matrix $\mathbf{H}(t)$ encapsulates

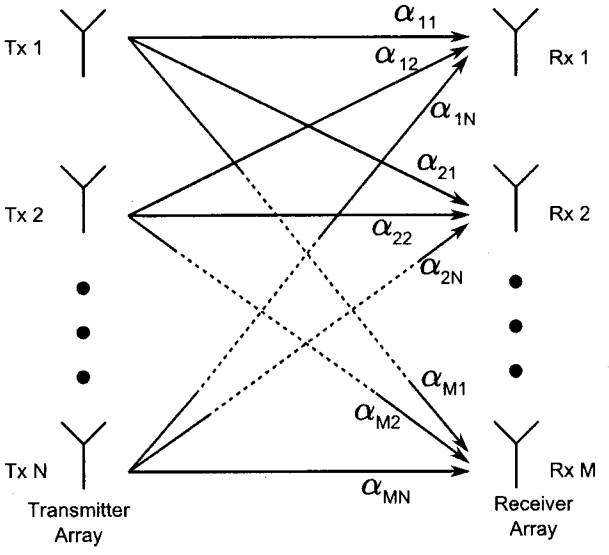

Figure 1.1: Typical $M \times N$ MIMO channel.

the complex subchannel fading coefficients $\alpha_{mn}(t)$ such that

$$\mathbf{H}(t) = \begin{bmatrix} \alpha_{11}(t) & \alpha_{12}(t) & \dots & \alpha_{1N}(t) \\ \alpha_{21}(t) & \alpha_{22}(t) & \dots & \alpha_{2N}(t) \\ \vdots & \vdots & \ddots & \vdots \\ \alpha_{M1}(t) & \alpha_{M2}(t) & \dots & \alpha_{MN}(t) \end{bmatrix}, \tag{1.2}$$

where $\alpha_{mn}(t)$ represents the subchannel at the m^{th} receiver element with respect to the n^{th} transmitter element[1].

In much of the theoretical work investigating MIMO communications, the coefficients of the MIMO channel matrix are modeled as independent and identically distributed (i.i.d.) complex Gaussian random processes [6]. In these ideal channel conditions, MIMO systems can achieve exceptional increases in capacity over traditional SISO systems [7]. However, in real channels, the subchannel characteristics are highly dependent on the physical environment and are often correlated or distributed differently. In the presence of these non-ideal characteristics, performance of a MIMO system can degrade significantly.

Uni-polarized MIMO Capacity

Perhaps the most exciting aspect of a MIMO communications systems is the potential for increased capacity. For a narrowband SISO communications system, Shannon's channel

[1]Note: herein the term *MIMO channel* refers to $\mathbf{H}(t)$ while the term *subchannel* refers to an individual fading coefficient $\alpha_{mn}(t)$.

capacity theorem states [8]

$$C_{SISO} = log_2(1+\gamma), \tag{1.3}$$

where C_{SISO} is the channel capacity for a single link, and the SNR $\gamma = \frac{P}{N_o}$ is the ratio of the signal power P to the noise variance N_o at the receiver. In an $M \times N$ MIMO system the transmitted data are first sliced into N separate streams and each is transmitted on a different antenna at the same time. Assuming the transmit power is the same for the SISO system, the resulting MIMO channel capacity is given by [9]

$$C = log_2(det[\mathbf{I}_M + \frac{\gamma}{N}\mathbf{H}\mathbf{H}^\dagger]), \tag{1.4}$$

where γ is the SNR at each element of the receiver, $\mathbf{I}_M$ is an $M \times M$ identity matrix and $\cdot^\dagger$ is the complex conjugation.

The capacity equation in (1.4) is highly dependent on the correlation of the elements within $\mathbf{H}$. For an $M \times N$ MIMO system the receive correlation matrix is

$$\mathbf{R}_{rx} = E\left\{\mathbf{H}\mathbf{H}^\dagger\right\} = \begin{bmatrix} \rho_{11}^{rx} & \rho_{12}^{rx} & \cdots & \rho_{1M}^{rx} \\ \rho_{21}^{rx} & \rho_{22}^{rx} & \cdots & \rho_{2M}^{rx} \\ \vdots & \vdots & \ddots & \vdots \\ \rho_{M1}^{rx} & \rho_{M2}^{rx} & \cdots & \rho_{MM}^{rx} \end{bmatrix}, \tag{1.5}$$

where $E\{\cdot\}$ is the expected value and ρ_{ij}^{rx} is the correlation coefficient between the i^{th} and j^{th} receiver. Similarly the correlation at the transmitter is

$$\mathbf{R}_{tx} = E\left\{\mathbf{H}^\dagger\mathbf{H}\right\} = \begin{bmatrix} \rho_{11}^{tx} & \rho_{12}^{tx} & \cdots & \rho_{1N}^{tx} \\ \rho_{21}^{tx} & \rho_{22}^{tx} & \cdots & \rho_{2N}^{tx} \\ \vdots & \vdots & \ddots & \vdots \\ \rho_{N1}^{tx} & \rho_{N2}^{tx} & \cdots & \rho_{NN}^{tx} \end{bmatrix}. \tag{1.6}$$

The effect of correlation on MIMO capacity is illustrated in Figure 1.2, which plots the cumulative distribution functions (cdfs) of capacity for a 4×4 MIMO system with increasing levels of correlation. For simplicity we assume that $\mathbf{R}_{rx} = \mathbf{R}_{tx}$ and use an exponential correlation model [10], then

$$\rho_{ij}^{rx} = \rho_{ij}^{tx} = \rho_s^{|i-j|}, \text{ where } 0 \leq \rho_s \leq 1. \tag{1.7}$$

The correlations are applied to the channel matrices using the correlation model presented in [11] in which the complete correlation of the MIMO channel is expressed as

$$\mathbf{R}_{MIMO} = \mathbf{R}_{tx} \otimes \mathbf{R}_{rx}, \tag{1.8}$$

where $\otimes$ is the Kronecker product. Letting $\mathbf{L}$ be the Cholesky factor of $\mathbf{R}_{MIMO}$, the correlated channel matrices $\mathbf{H}$ can be generated using

$$\mathbf{q} = \mathbf{L}\mathbf{g}, \tag{1.9}$$

where $\mathbf{g} = [\alpha_{11}, \alpha_{21}, \ldots, \alpha_{M1}, \alpha_{12}, \ldots, \alpha_{MN}]^T$, such that α_{mn} are i.i.d. circularly symmetric complex Gaussian random variables with zero mean and a unit variance. The channel matrix is then compiled from the correlated elements of $\mathbf{q}$ such that

$$\mathbf{H} = reshape\{\mathbf{q}\}_{M\times N}, \tag{1.10}$$

where $reshape\{\cdot\}_{M\times N}$ is a columnwise reshaping of the length-MN vector into an $M \times N$ matrix [11].

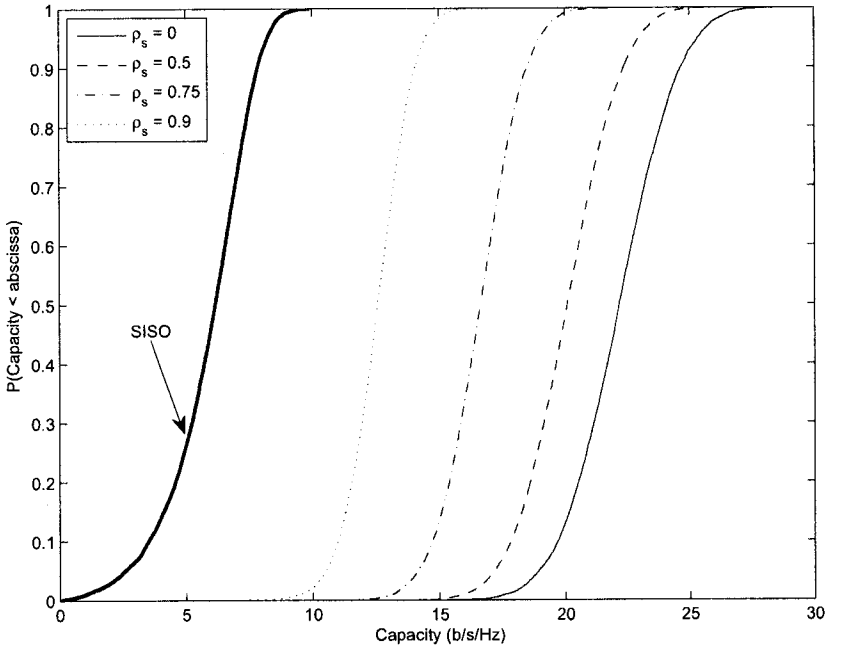

Figure 1.2: CDF of 4 x 4 MIMO capacity at 20 dB SNR for different antenna correlations (ρ_s).

As the correlation increases the capacity drops. When $\rho_s = 0$ the subchannels are completely independent and the median capacity is about 22 b/s/Hz. As the correlation rises the capacity drops to about 16 b/s/Hz and 12 b/s/Hz at $\rho_s = 0.75$ and $\rho_s = 0.9$, respectively. Included for reference is the capacity of a SISO system. Even in highly correlated channels, the capacity of the MIMO system exceeds that of the SISO system by about 6 b/s/Hz. In correlated channels, the improvement over a SISO system is due to the beamforming gain resulting from receiving on M antennas [3].

The reduction in capacity, caused by increased correlation, results from the effect correlation has on the structure of MIMO channel and can be understood by examining the eigenvalue decomposition of the channel's correlation matrix. The eigenvalue decomposition of a Hermitian matrix is [12]

$$\mathbf{H}\mathbf{H}^{\dagger} = \mathbf{U}\mathbf{\Sigma}\mathbf{U}^{\dagger} = \sum_{i=1}^{k} \delta_i^2 \mathbf{u}_i \mathbf{u}_i^{\dagger}, \tag{1.11}$$

where $\mathbf{\Sigma} = diag([\delta_1^2 \ \delta_2^2 \ \dots \ \delta_k^2])$ is the diagonal matrix of real positive eigenvalues δ_i^2, $\mathbf{U} = [\mathbf{u}_1 \ \mathbf{u}_2 \ \dots \ \mathbf{u}_k]$ is a unitary matrix of eigenvectors $\mathbf{u}_i$ and $k = min\{M, N\}$. Together, the eigenvectors and eigenvalues define the subspace structure of the channel. Each eigenvector represents an orthogonal subspace channel, or eigenmode, over which communication occurs. The eigenvalues are the powers associated with each subchannel.

In terms of the eigenvalues, capacity can be rewritten as

$$C = log_2(det[\mathbf{I}_M + \frac{\gamma}{N}\mathbf{\Sigma}]) = \sum_{i=1}^{k} [log_2(1 + \frac{\gamma}{N}\delta_i^2)]. \tag{1.12}$$

Assuming $M = N$ and constraining the total power such that $\|\mathbf{H}\|_F^2 = \sum_{i=1}^{N} \delta_i^2 = \Upsilon$, the capacity in (1.12) will be maximised when $\delta_i^2 = \frac{\Upsilon}{N} \ \forall \ i$. Such a scenario would arise when all the MIMO subchannels are orthogonal resulting in a diagonal correlation matrix $\mathbf{R}$. Under these conditions (1.12) would become

$$C = \sum_{i=1}^{N} [log_2(1 + \Upsilon\frac{\gamma}{N^2})] = Nlog_2(1 + \Upsilon\frac{\gamma}{N^2}). \tag{1.13}$$

Assuming a unit variance for each MIMO subchannel, $\|\mathbf{H}\|_F^2 = \Upsilon = MN = N^2$ and (1.13) simplifies to $C = Nlog_2(1 + \gamma)$ [12]. This represents an N times increase over the capacity of a SISO channel (1.3) with equal total transmit power. However, as the subchannels of $\mathbf{H}$ become correlated, the power will be much greater on a subset of the eigenmodes and (1.12) will be reduced. Take for example the extreme scenario where the all the elements of the array antennas are positioned very close together and the signal arrives at the receiver constrained in a very narrow angular spread. In this example, the channel fading coefficients will be highly correlated, constraining most of the transmit power to a single eigenmode. Assuming $\delta_i \approx 0 \ \forall \ i \neq 1$ (1.12) will become $C \approx log_2(1 + N\gamma)$ which is equivalent to a SIMO channel [3]. The capacity is still greater than that of a SISO channel due to the diversity gain resulting from the multiple transmit antennas.

1.1.2 Polarization Diversity

Numerous methods exist for achieving diversity in a MIMO system. Although using spatially separated antenna elements is often discussed, an alternative method is to exploit polariza-

tion diversity. Consider the case of a communications system with a single dipole antenna at both the transmitter and the receiver. The transmitting element emits an electromagnetic (EM) wave consisting of electric and magnetic fields in which the oscillation of each wave is orthogonal to the other and to the direction of travel, see Figure 1.3. Generally, in wireless communications, only the electric field portion of the EM wave is of interest. The polarization of the electric field is in the direction of the oscillation. For example, in free space, the polarization of an EM wave emitted by a dipole will be defined by the antenna's orientation. Assigning terms such as *vertical* and *horizontal* to the antenna orientation can be ambiguous, especially at the mobile where the positioning of the antenna is dependent upon the orientation of the mobile device. For this thesis however, vertical is considered to be the plane perpendicular to the earth and horizontal is the plane parallel to the earth. This terminology coincides with the orientations of the antennas used in the measurements discussed in later sections.

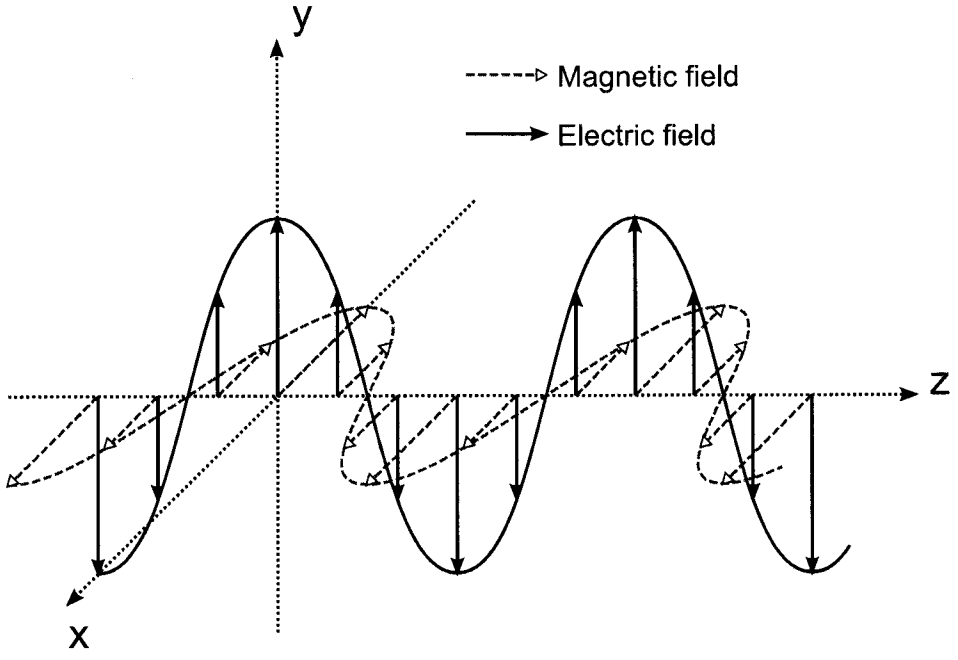

Figure 1.3: Electromagnetic wave.

In free space, an EM wave generated from a vertically oriented dipole antenna will retain a vertical polarization at the receiver. In real environments, however, the wave will encounter surfaces with random orientations. Smooth surfaces will result in reflections in which the energy and polarization of the reflected component is dependent on the dielectric constant of surface material and the angle of incidence with respect to the orientation angle of the surface. For rough surfaces, the signal component will be scattered, resulting in a number of

multipath components. This can be thought of as multiple reflections from a small irregular surface [13, Chapter 3.2] in which the directions of travel and polarizations of the reflected components are considered random. Before reaching the receiver, the transmitted signal may undergo a number of reflection and scattering events which results in multiple signal components with random polarizations at the receiver. The received signal is no longer vertically polarized, instead it is a combination of both vertically and horizontally polarized components. This process is referred to as depolarization. At the receiver each incident multipath component can be viewed as a electric field vector $\boldsymbol{E_I}$ in three dimensions as shown in Figure 1.4 and expressed by

$$\boldsymbol{E_I} = E_X\mathbf{x} + E_Y\mathbf{y} + E_Z\mathbf{z}. \tag{1.14}$$

This can be written in polar coordinates as

$$\boldsymbol{E_I}(\theta, \phi) = E_\theta(\theta, \phi)\boldsymbol{\theta} + E_\phi(\theta, \phi)\boldsymbol{\phi}, \tag{1.15}$$

where $E_\theta(\theta, \phi)$ and $E_\phi(\theta, \phi)$ are the electric fields in the vertical polarization (VP) and horizontal polarization (HP), respectively. Similarly, the antenna pattern can be modeled as

$$\boldsymbol{A_p}(\theta, \phi) = A_\theta(\theta, \phi)\boldsymbol{\theta} + A_\phi(\theta, \phi)\boldsymbol{\phi}, \tag{1.16}$$

where $A_\theta(\theta, \phi)$ is the vertically polarized antenna pattern and $A_\phi(\theta, \phi)$ is the horizontal.

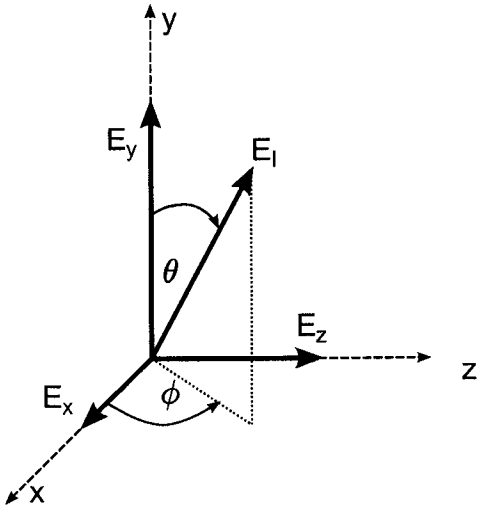

Figure 1.4: Cartesian and polar coordinates of an electric field vector.

The resulting open circuit voltage V_{oc} at the receive antenna is the sum total of incident energy projected onto each polarized antenna pattern [13]

$$V_{oc} = \iint \boldsymbol{E_I}(\theta, \phi) \cdot \boldsymbol{A_p}(\theta, \phi)\, d\theta\, d\phi. \tag{1.17}$$

For the measurements presented in this report the receiver used dual-linear polarized patch antennas with separate outputs for the vertically and horizontally polarized antenna patterns. Therefore, these antennas act as polarized filters separating $\boldsymbol{E_I}$ into its polarized components such that the vertically polarized V_{oc}^{v} and horizontally polarized V_{oc}^{h} signal components are given by

$$V_{oc}^{v} = \int E_{\theta}(\theta,\phi)A_{\theta}(\theta,\phi)\,d\theta \tag{1.18}$$

and

$$V_{oc}^{h} = \int E_{\phi}(\theta,\phi)A_{\phi}(\theta,\phi)\,d\phi. \tag{1.19}$$

Dual-polarized MIMO Capacity

For MIMO systems, dual-polarized antennas can be used to exploit polarization diversity resulting from the uncorrelated fading of orthogonally polarized subchannels. When a polarized signal propagates through a cluttered environment it interacts with obstacles and is reflected by smooth surfaces, scattered by rough surfaces and diffracted around edges. The effect each obstacle has on the incident signal component is a function of both its material properties (dielectric constant and surface roughness) and the orientation of the surface with respect to the signal's polarization. As a result the propagation characteristics for orthogonally polarized signal components are, theoretically, statistically independent [3, Chapter 13].

Figure 1.5 shows the array configuration of a MIMO system with spatially separated, uni-polarized transmit antennas and dual-polarized receive antennas. The dual-polarized channel

$$\mathbf{H}^{dp} = \begin{bmatrix} \mathbf{H}^{V} \\ \mathbf{H}^{H} \end{bmatrix}, \tag{1.20}$$

is modeled by stacking the $M_p \times N$ vertically polarized channel matrix $\mathbf{H}^{V}$and horizontally polarized channel matrix $\mathbf{H}^{H}$, where

$$\mathbf{H}^{V} = \begin{bmatrix} \alpha_{11}^{V} & \alpha_{12}^{V} & \dots & \alpha_{1N}^{V} \\ \alpha_{21}^{V} & \alpha_{22}^{V} & \dots & \alpha_{2N}^{V} \\ \vdots & \vdots & \ddots & \vdots \\ \alpha_{M_p1}^{V} & \alpha_{M_p2}^{V} & \dots & \alpha_{M_pN}^{V} \end{bmatrix} \tag{1.21}$$

and

$$\mathbf{H}^{H} = \begin{bmatrix} \alpha_{11}^{H} & \alpha_{12}^{H} & \dots & \alpha_{1N}^{H} \\ \alpha_{21}^{H} & \alpha_{22}^{H} & \dots & \alpha_{2N}^{H} \\ \vdots & \vdots & \ddots & \vdots \\ \alpha_{M_p1}^{H} & \alpha_{M_p2}^{H} & \dots & \alpha_{M_pN}^{H} \end{bmatrix}. \tag{1.22}$$

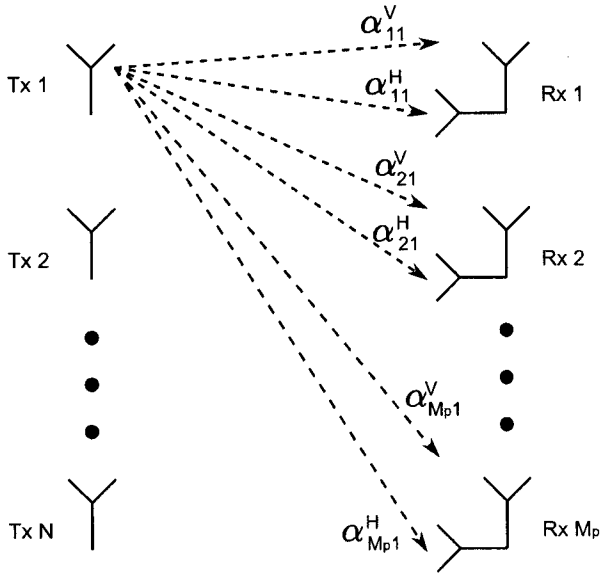

Figure 1.5: Dual-polarized MIMO channel.

The receive correlation matrix of dual-polarized channels $\mathbf{R}_{rx}^{dp}$ will be a combination of spatial correlations and cross-polar correlations. For example, a system with $N = 4$ transmit antennas and $M_p = 2$ dual-polarized receive antennas will have a correlation matrix defined by

$$\mathbf{R}_{rx}^{dp} = \begin{bmatrix} \rho_{11}^{vv} & \rho_{12}^{vv} & \rho_{11}^{vh} & \rho_{12}^{vh} \\ \rho_{21}^{vv} & \rho_{22}^{vv} & \rho_{21}^{vh} & \rho_{22}^{vh} \\ \rho_{11}^{hv} & \rho_{12}^{hv} & \rho_{11}^{hh} & \rho_{12}^{hh} \\ \rho_{21}^{hv} & \rho_{22}^{hv} & \rho_{21}^{hh} & \rho_{22}^{hh} \end{bmatrix}, \tag{1.23}$$

where ρ_{mn}^{ij} is the correlation between the m^{th} vertically ($i = v$) or horizontally ($i = h$) polarized element and the n^{th} vertically ($j = v$) or horizontally ($j = h$) polarized element. The ρ_{mn}^{vv} and ρ_{mn}^{hh} terms are spatial correlations, while the ρ_{mn}^{vh} and ρ_{mn}^{hv} terms are cross-polar correlations. If the cross-polar terms of $\mathbf{R}_{rx}^{dp}$ are low the channel will be guaranteed to have at least two strong eigenmodes regardless of the spatial correlations. This provides an improvement in diversity over a highly correlated uni-polarized system in which the signal is dominated by a single eigenmode.

The possible benefits of dual-polarized systems resulting from reduced correlations is offset, at least partially, by the cross polarization discrimination (XPD). When a polarized signal is transmitted, the power received on the orthogonal polarization is often less than that received on the transmitted polarization. The XPD is the ratio between these two powers. This power imbalance between the polarized receive branches represents a loss in total received power when compared to the power received with just spatial separations.

The effect of the combined spatial and cross-polar correlations on the average channel capacity of a $M_p = 2 \times N = 4$ MIMO system is plotted in Figure 1.6 as a function of the XPD. For the simulation, $\mathbf{R}_{MIMO}$ is composed of the transmit correlation matrix $\mathbf{R}_{tx}$ and the dual-polarized correlation matrix $\mathbf{R}_{rx}^{dp}$. As in (1.7), an exponential correlation model is used for the spatial correlations in $\mathbf{R}_{tx}$. Similarly, at the receiver $\rho_{mn}^{vv} = \rho_{mn}^{hh} = \rho_s^{|m-n|}$, however, the cross-polar terms are assumed to be independent such that $\rho_{mn}^{vh} = \rho_{mn}^{hv} = 0$. The correlated channels are generated as in (1.9) and (1.10), and the XPD is applied such that

$$\mathbf{H}^{dp} = \Xi\mathbf{H}, \tag{1.24}$$

where $\Xi = diag\{[1, 1, \sqrt{XPD^V}, \sqrt{XPD^V}]\}$, $diag\{\cdot\}$ is a diagonal matrix with the vector argument along the main diagonal and

$$XPD^V = E\left\{\frac{tr\{\mathbf{H}^V(\mathbf{H}^V)^\dagger\}}{tr\{\mathbf{H}^H(\mathbf{H}^H)^\dagger\}}\right\}. \tag{1.25}$$

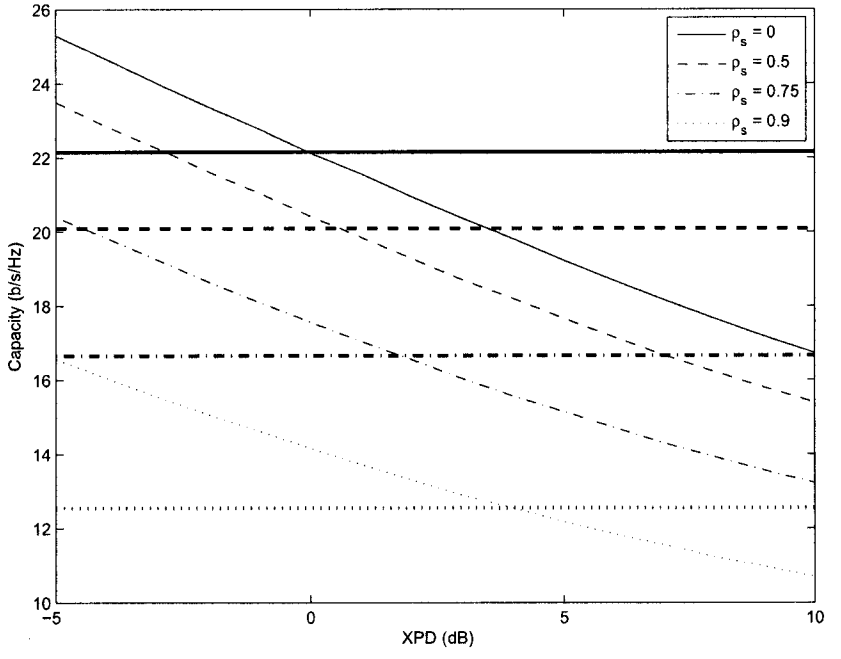

Figure 1.6: Capacity as a function of correlation and XPD. The bold lines show the average capacity for a uni-polarized 4×4 MIMO system.

When the spatial correlations are low, as in the $\rho_s = 0$ plot, the decreased cross-polar correlations offer no additional capacity gain for $XPD^V \geq 0$. However, as the correlation increases the capacity of the dual-polarized channels is greater than that of the uni-polarized channels for a range of XPD values that increases with the correlation. For $\rho_s = 0.75$ and

$\rho_s = 0.9$, the capacity of the dual-polarized channels are greater than that of the uni-polarized channels for $XPD^V \leq 2$ and $XPD^V \leq 4$, respectively. As the XPD increases, the capacity of the dual-polarized channels continues to drop due the reduced received power at the orthogonal polarization.

From Figure 1.6 it is evident that, even in the scenario with completely independent cross-polarized subchannels, polarization diversity can only provide a performance gain (in terms of capacity) over spatial diversity systems when the XPD is below a certain threshold. However, polarization diversity also offers the practical benefit of a reduced array footprint. In spatial diversity systems, an element separation of 0.5λ will provide a sufficient level of decorrelation in environments in which the number of multipath components is large and the distribution of the angles of arrival (AOA) is uniform. Such environments may be found in outdoor urban locations as well as many indoor settings. However, in rural settings, which tend to lack scatterers, or at tower mounted base stations, where the angular spread of the arriving signals tend to be narrow, an increased element separation will be required to provide an adequate level of decorrelation. This presents a number of practical challenges due to the expense of increasing the array footprint on antenna towers coupled with the trend toward miniaturization of the radio at the mobile. As a result a significant challenge in the implementation of MIMO systems is the design of compact antenna arrays which offer adequate diversity. A possible solution may be to exploit polarization diversity, even if it does not achieve the full potential of a spatially separated array.

1.2 Literature review

The use of orthogonally polarized channels as a method of achieving diversity is not a new idea. In [14], measurements of HF radio channels were used to investigate the daily variations of amplitude and phase in the linearily polarized components of an elliptically polarized signal. The possible benefits of polarization diversity was noted as the polarized channels generally exhibited independently fading Rayleigh characteristics. However the correlation between the two polarized components varied depending on the time of the day.

Later investigations looked at the applicability of polarization diversity in microwave systems. Lee and Yeh [2] investigated polarization diversity as a solution to reduce antenna separations at the base station and at the mobile using a two branch diversity system with both vertically and horizontally polarized antennas colocated at each end. They derived the correlation coefficient of the polarized squared envelopes based on the XPD and showed that for the correlation to be greater than 0.7 the XPD has to be less than 5 dB. Kozono et al. added the effect of AOA and the polarization angle into the correlation equation [15]. It was shown that increasing the polarization angle decreased the correlation but also

resulted in an overall decrease in signal level at the output of the diversity combiner. Similar results were reported by Vaughan [16] in which the envelope correlation coefficient was derived as a function of the XPD and polarization angle. It was observed that in suburban environments, where one polarization dominates over the other due to insufficient scattering, the XPD can be large and the diversity gain is minimal. However, lower levels of XPD in urban environments due to increased scattering can result in significant diversity gains.

Turkmani et al. [17] compared the impact of transmit antenna rotation when the receive system used either a dual-polarized antenna or two spatially separated uni-polarized antennas. In a mobile communications system, a particular orientation of the handset antenna cannot be assured. Turkmani et al. found that a rotation of the transmit antenna (handset) results in a loss of power at the spatially separated, uni-polarized receive antennas which resulted in a loss in diversity. However, if dual-polarized receive antennas were used, much of the power lost on one polarization, due to the orientation angle of the handset, was recovered on the orthogonal polarization.

Although early investigations primarily focused on transmit or receive diversity systems, observations of the polarized channel provide useful insight into the behaviour of MIMO systems in which similar propagation processes are exploited. MIMO has exploded in popularity in recent years but the overall amount of research related to measuring and characterizing the outdoor polarized MIMO channel has been comparatively small. Measurements at 1.9 GHz were performed by Martin et al. [18] in which capacity and correlation were characterized for a number of different polarized array configurations at the base station and mobile. Near theoretical capacities were measured using two dual-polarized antennas at both the transmitter and the receiver with $\pm$ 45° polarization angles and a 20 wavelengths spatial separation at the base station. Considerably lower levels of capacity were measured for the configurations in which the base station used polarized multibeam antennas due to the increased correlation when the mobile was in a single beam, however, between beams the capacity increased by as much as two times.

Extensive characterization of outdoor polarized MIMO channel parameters, including path loss, K-factor, XPD and correlation, were performed by Erceg et al. in [19, 20]. In [19], both the K-factor and XPD were observed to decrease with distance whereas the cross-polar correlations remained low regardless of the separation between the transmitter and receiver. This is in contrast to the spatial correlation which were observed to have a dependency on distance in [20]. On average, the K-factors measured on cross-polarized channels were lower than those of the co-polarized channels due to the scattering processes inherent in the depolarization of a polarized signal. In [20] comparisons of the channel correlation matrix condition number for spatial and polarization diversity systems revealed that in channels with high K-factor, polarization diversity can improve the condition number, indicating a

more favourable distribution of eigenvalues. However, the improvement is only beneficial assuming the XPD does not exceed a certain value.

Additional measurements have been reported in [21, 22, 23]. In [21], capacities were measured in outdoor and indoor uni-polarized and dual-polarized channels. Polarization diversity provided higher capacities than the uni-polarized system in the outdoor and, to a lesser extent, in the indoor environments. Measurements of polarized MIMO channels in a rural environment were performed in [22] and similar behaviours for pathloss, Doppler and angular spreads were observed on both the cross- and co-polarized channels. When compared to a vertically polarized system, the dual-polarized systems achieved capacities 30% higher in environments with low to moderate scattering. In [23] the results of the measured XPD values at 5.3 GHz were compared to ray tracing simulations where it was shown that accounting for scattering in the ray tracing simulations increases the accuracy of XPD predictions.

A significant body of work exists in which the indoor polarized MIMO channel is characterized for line-of-sight (LOS) and non-line-of-sight (NLOS) environments. A particular focus has been characterizing the distribution of eigenvalues [24, 25, 26], the cross-polar correlations [27, 28, 26, 29, 30, 31], and the XPD [26, 32, 28] as well as studying the effect these channel parameters have on MIMO capacity [27, 28, 25, 29]. An extensive study of the indoor channel was performed by Kyritsi et al. [27]. The indoor measurements were performed for large antenna arrays and the channel capacities achieved with uni-polarized (vertically or horizontally) transmit and receive antennas were compared to those of a system with orthogonally polarized array elements. For both the LOS and NLOS scenarios investigated, higher capacities were measured on the orthogonally polarized channels, a performance advantage attributed to the reduced subchannel correlation resulting from combining both spatial separation and orthogonal polarizations. In [25], the capacities with linear arrays of dual-polarized patch antennas in indoor environments were as high or higher than those measured on arrays with only a single polarization even with reduced power on the cross-polar channels. Again, this was attributed to the fact that in the dual-polarized channels, power in the two dominant eigenmodes is more evenly distributed than in the uni-polarized systems due to the low correlation of polarized channels. In [29], the capacity performance of just the cross-polarized channels (vertical to horizontal and horizontal to vertical) was observed to be worse than the co-polarized capacity in the same environment due to the high XPD values measured in the LOS (16 dB) and NLOS (8 dB) scenarios. In general, when comparing the performance of polarization diversity systems to spatial diversity systems the trade-off between decreased correlation and loss of power on the cross-polar subchannels must be accounted for. A number of studies indicate that, without a spatial separation between polarized elements, the performance benefits of polarized systems are reduced when

compared to spatially separated elements of a single polarization [28, 25].

The characteristics of polarized MIMO channels measured in indoor and outdoor environments suggests that polarization diversity may be a useful approach to improving performance in MIMO systems with reduced array footprint. In general, MIMO signal processing techniques fall into one of two categories: 1) spatial multiplexing for increasing spectral efficiency or 2) spatial diversity for improving bit error performance. The performance of both spatial multiplexing [33, 34, 26, 35] and spatial diversity [36, 33, 34, 35] has been investigated for dual-polarized MIMO systems. In [33], the methods for calculating the error performance of the Alamouti orthogonal space time block coding (OSTBC) scheme [4] and spatial multiplexing with $\pm$ 45° dual-polarized transmit and receive antennas were developed for Rayleigh and Ricean fading channels. It was shown that, for channels with both high and low spatial correlation, the error performance of OSTBC will worsen if polarization diversity is used due to the loss in power resulting from the XPD. However, in spatial multiplexing systems, the use of polarization diversity can improve error rates if the transmit or receive spatial correlations are high. Similar results were found by Oestges et al. in [35], however, for the Alamouti system it was noted that conditions may arise in the channel, which are dependent on the subchannel correlations and on the XPD, where polarization diversity achieves a higher diversity order than spatial diversity, though this does not necessarily imply improved error performance.

Insight has also been provided from parametrized stochastic and geometric models which predict the characteristics of the polarized MIMO channel. A 2D geometric model based on the stochastic arrangement of scatterers was presented in [37] in which the polarization effects of the channel are modeled via a scattering matrix which combines the XPD and the polarized reflection coefficients for each multipath component. In [19] a polarized channel model for Ricean channels is presented in which the K-factor and XPD are modeled as Gaussian random processes with non-zero, distance dependent means. In [32], a stochastic 3D scattering model in which the spatial and cross polar correlations of the multipath components distributed in elevation and azimuth are modeled as functions of the distance and delay dependent XPD.

The measurements and analysis of the polarized channel characteristics contained within this thesis offers additional insight into the use of polarization diversity in mobile MIMO communications systems operating in urban environments. Of particular focus is the heterogeneity of the channel as measured in different environments and at different locations on the mobile. The main contributions of this thesis are outlined in the following section.

1.3 Thesis contributions

Measurements of polarized mobile MIMO urban channels:

Although a number of measurements of polarized MIMO channels have been performed, few have investigated mobile terminals in urban environments. As such, a full characterization of polarized urban mobile MIMO channels is not complete. This thesis offers further insight into these channels through characterization of important propagation parameters such as received power, XPD, diversity and correlation. Additionally, the measurements performed consist of a number of scenarios in different channel environments, e.g. specular, NLOS, urban canyons and street intersections, the impact of which will also be discussed.

Comparisons of uni-polarized and dual-polarized channels:

The measurement system consists of a mobile receiver with arrays of dual-polarized patch antennas which enabled the near-simultaneous sampling of both vertical and horizontal polarizations. Comparisons between systems in which the receiver array is purely vertically polarized or horizontally polarized and when the array consists of a combination of elements with both polarizations are made.

The effect of the vehicular placement of array elements:

As a result of the placement of the antenna array elements on the vehicle, the subchannels measured at different elements of the array often exhibit unique channel characteristics. The practical issues of array placement on vehicles especially as it relates to the effect of vehicular shadowing on portions of the array is discussed.

Polarized MIMO system simulations:

The effects of antenna polarization, the propagation environment and the effect of vehicular array placement on the performance of MIMO detection techniques is discussed using simulations on measured channels.

1.4 Thesis Organization

This thesis is organized into eight chapters. The CRC MIMO channel sounder is described in Chapter 2 and an overview of the measurement campaign is provided. Chapter 3 discusses the polarized channel characteristics observed in each of the measurement environments. A detailed analysis of the angular distribution of power received at each side of the measurement vehicle is given in Chapter 4 and used to provide insight into the spatial and cross-polar

correlation discussion contained in Chapter 5. In Chapter 6, characteristics of the channels measured at each side of the mobile are considered separately and related to the channel characteristics discussed in Chapter 3. The results of system simulations, using the measured data, are provided in Chapter 7 and the performances on polarized and cross-polarized channels compared. Concluding remarks are made in Chapter 8.

Chapter 2

Measurement System

For the investigation contained within this thesis, measurements of polarized MIMO channels were performed using the CRC MIMO channel sounder. These measurements required that modifications be made to the measurement system to enable the near simultaneous acquisition of orthogonally polarized channel response data. This chapter discusses the measurement system and the necessary modifications that were made.

2.1 CRC MIMO Channel Sounder

The CRC MIMO channel sounder (CRC-MCS) is a wideband wireless channel measurement system. Operating as a true MIMO system, unique sounding sequences generated by the transmitter are radiated simultaneously on each element of the transmit array. At the receiver, the signal levels sensed by each receive array element are simultaneously captured and stored for later processing. The focus of the CRC-MCS project is to support research in wideband wireless mobile channels for both military and commercial applications. Often the communications techniques and operating environments of interest in military focused research are different from those of commercial applications. In an effort to meet the requirements for both types of research a design philosophy was adopted which centred on system flexibility and configurability. It was recognized early on that key measurement system specifications, such as the number of antennas, the operating frequency and the array geometry, would change depending on the focus of the research. Motivated by this requirement for flexibility, components were chosen to allow the system to operate in a broad range of scenarios with minimal hardware and software modifications. The result is a highly modular system which is adaptable to numerous research scenarios.

In its base configuration the sounder operates as an eight element transmitter and an eight element receiver synchronized using highly stable rubidium frequency standards. These standards provide frequency synchronization between the receiver and the transmitter and

serve as stable references for the digital and analog clock signals used in the up- and down-conversion networks.

To support the polarization diversity investigation presented herein the CRC-MCS was fitted with additional timing and switching circuitry to exploit eight dual-polarized patch antennas at the receiver. This expansion to the system allows for the near simultaneous acquisition of both horizontally and vertically polarized signals.

The following sections contains an overview of the design and operation of the CRC-MCS. It begins with a description of the transmitter and receiver hardware as used in a typical measurement. The chapter ends with a discussion of the measurement antennas and details modifications made to the receiver to perform the polarization measurements analyzed within this report.

2.1.1 Transmitter

A high level block diagram of the CRC-MCS transmitter is given in Figure 2.1. The transmitter back-end consists of two four-channel ICS660B digital-to-analog (D/A) converter cards mounted in a PC. The set of sounding sequences for each channel are preloaded into memory on the D/A cards by the control software. These are pseudo-noise sequences of 1023 samples designed to both minimize the maximum non-zero lag of the auto-correlation and to minimize the maximum of the cross-correlation between sequences [38]. Once started the system continuously loops over the stored sequence data at a rate of 50 Msamp/s, generating a 25 MHz analog baseband signal at each D/A channel output. Oversampling by the transmitter results in a chip rate of 12.5 MHz.

For generation of the baseband signal it is necessary is to ensure that the digital to analog conversion at each D/A card is synchronized. This is achieved using a rubidium frequency standard's highly stable 10 MHz clock signal multiplied up to 50 MHz and fed to each D/A card through external clock input ports.

Although the D/A cards can be started (or triggered) using a software command, attempting to trigger two cards in this manner may result in start delays between D/A cards on the order of 10 ms. Such delays are unacceptable as the receiver depends on accurate timing of the transmitted sequences to ensure that impulse responses measured from each transmit element are separable. Any pseudo-random timing delays could result in an overlap of the impulse response delay profiles at the receiver. As a result, determining the individual subchannel responses would be impossible. Instead of using a software trigger, the external trigger input port on each D/A card is connected to the PC parallel port. To start the cards, the control software generates a start signal on the parallel port which simultaneously triggers each card.

To generate the wideband RF output the transmitter uses direct conversion of the base-

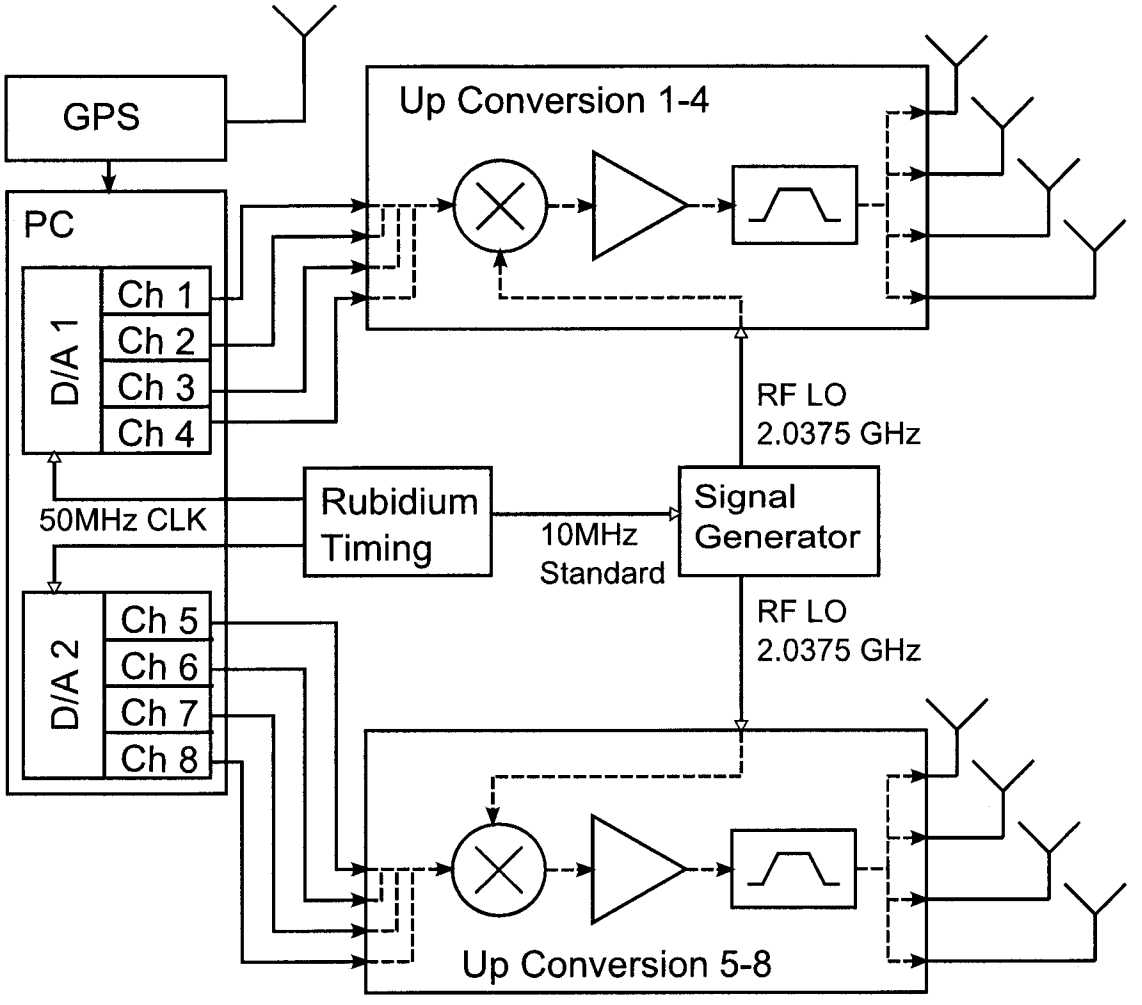

Figure 2.1: CRC-MCS transmitter block diagram.

band signal up to 2.0375 GHz. Within the up-conversion block, the baseband data modulates a 2.0375 GHz local oscillator (LO) generated by a Racal 3271 signal generator. The Racal 3271 is used as a tunable carrier wave source capable of supplying an LO signal from 9 kHz to 2.4 GHz at a power level up to 19 dBm. This provides considerable flexibility for the CRC-MCS operating frequency. To ensure that the LO frequency is stable and to minimize the offset between the transmitter and receiver centre frequencies the 10 MHz from the rubidium standard is supplied to the signal generator as a reference for generating the LO.

In the up-conversion portion of the CRC-MCS, modulation is performed using mixers with a high third-order intermodulation product (IP3) to minimize the effect of mixer nonlinearities. The baseband and LO signal levels are also tuned to minimize the formation

of harmonic components that may corrupt the output signal. This tuning is performed at the calibration stage prior to performing a measurement. The RF signals output at the mixers are then amplified and passed though bandpass filters before being radiated through drooping radial monopole antennas (Section 2.1.3).

A GPS unit is also integrated at the transmitter and is useful for logging the location of the transmitter during measurements. However, the GPS information is unreliable for the measurement environments discussed within due to the unavailability of satellite signals in urban canyons. Thus, the GPS information is not used for analyzing these measurements.

Transmitter Control Software

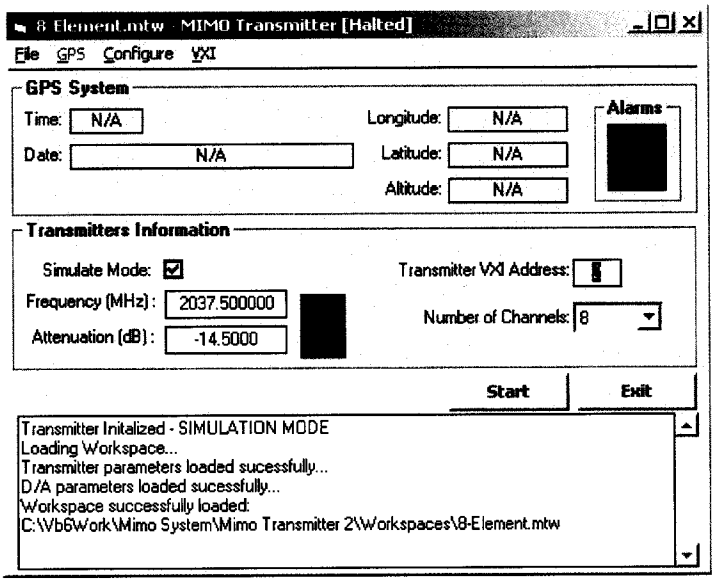

Figure 2.2: CRC-MCS transmitter control software main window.

Figure 2.2 shows the main graphical user interface (GUI) for operating the CRC-MCS transmitter. The control software was written in a combination of C++ and Visual Basic and allows the user to easily configure the system as required by the particular measurement campaign. For example, loading the sounding sequence data, changing the number of elements to transmit on, modifying the transmit frequency and adjusting the output power can all be accomplished through the software interface. Extended configuration options for fine tuning the transmitter settings are accessed though the configuration windows shown in Figure 2.3, Figure 2.4 and Figure 2.5. Once configured, the settings can be saved through the main GUI and stored in a workspace file which can be reloaded at a later point to repeat a given experiment.

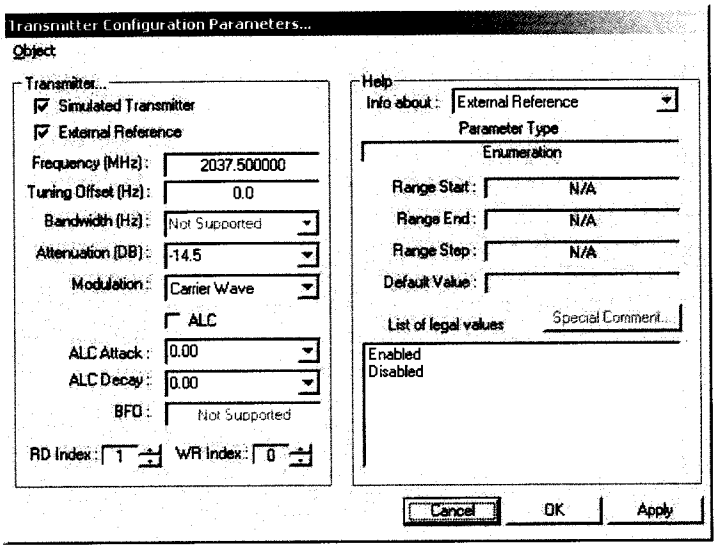

Figure 2.3: The CRC-MCS carrier frequency configuration window.

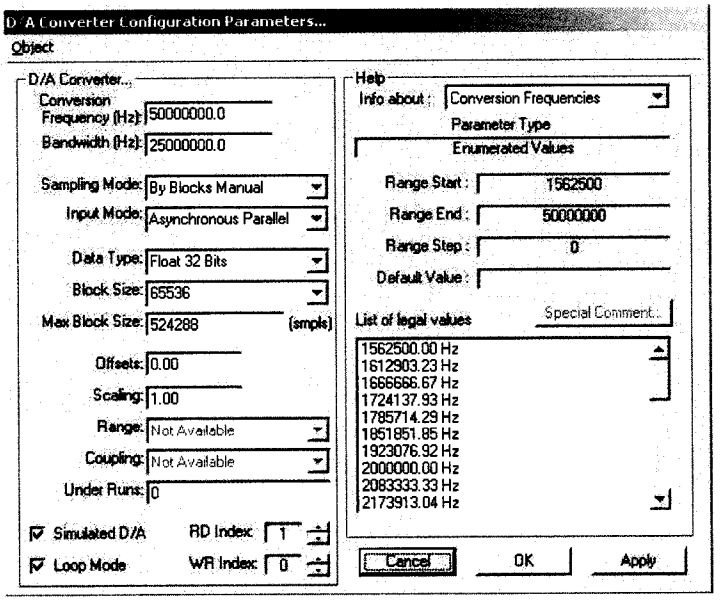

Figure 2.4: The CRC-MCS configuration window for general D/A settings.

2.1.2 Receiver

A block diagram representing a high-level layout of the CRC-MCS is shown in Figure 2.6. The receiver implements a two-stage down-conversion. At the front-end, the signals output by the antenna array are amplified by low noise amplifiers and passed through bandpass filters before undergoing the first stage of down-conversion. This first stage is handled by

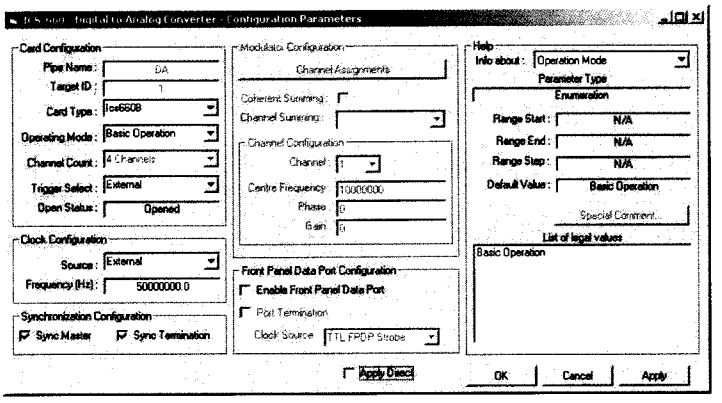

Figure 2.5: The CRC-MCS configuration window for ICS660 specific settings.

Watkins-Johnson 8633 (WJ-8633) receivers, one for each array antenna element. The WJ-8633 can process signals with bandwidths up to 80 MHz and can operate at a centre frequency anywhere from 70 MHz to 2.7 GHz. This broad frequency operation range contributes to the overall flexibility of the sounder system. As in the transmitter, a 10 MHz reference clock from a rubidium frequency standard is distributed to each WJ-8633 thus minimizing any offset in centre frequency between the transmitter and receiver.

The WJ-8633 down-converts the 25 MHz wide RF signal and outputs it at an intermediate frequency (IF) of 160 MHz. To perform complex down-conversion to baseband each IF signal is split and mixed with an in-phase and quadrature (I & Q) 160 MHz LO derived from the rubidium frequency standard. The baseband signal is then amplified by a bank of amplifiers which are tunable in both gain and DC offset. Prior to performing a measurement, these amplifiers are adjusted to ensure equal gain and zero DC offset on each RF chain. Finally, the baseband signal is filtered with lowpass filters to remove any high frequency mixing products or amplifier harmonics.

The baseband I & Q signals are sampled at 50 Msamp/s by eight 14-bit dual-channel analog-to-digital (A/D) converter cards, each operating within a separate PC. Due to the fast sampling rate, the length of time over which a continuous acquisition occurs must be limited. The A/D cards have 1 Msamp of memory for each channel so acquired data must be constantly transferred to the PC hard drives. Continuous acquisition of 14-bit complex data at 50 Msamp/s would require a sustained hard drive transfer rate of nearly 200 MB/s. Not only would this result in a massive amount of measurement data, the PCs are unable to sustain such enormous data write speeds to hard drive. To reduce the required transfer rate, the received signal is captured as a time series of short snapshots, each representing two sequence lengths of data. The minimum rate at which the snapshots must be captured is determined by the coherence time of the channel which is inversely proportional to the

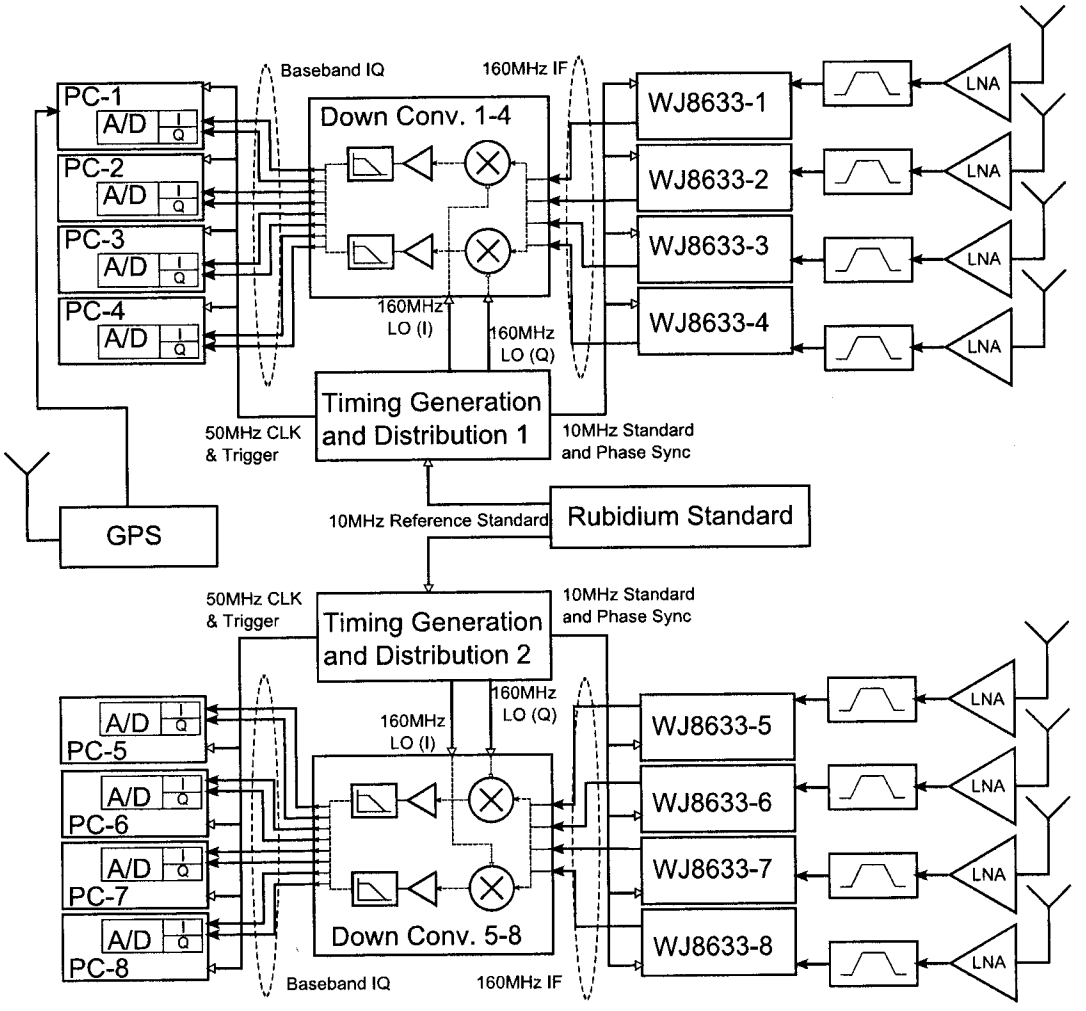

Figure 2.6: CRC-MCS receiver block diagram.

maximum Doppler frequency. For the measurements analyzed herein, the mobile is traveling at approximately 30 km/hr or 8.3 m/s. At these speeds the maximum Doppler frequency will be approximately 60 Hz requiring a minimum sampling frequency of 120 Hz to satisfy the Nyquist rate. To ensure adequate sampling, the rate at which the channel was captured was set to 250 Hz. Herein this is referred to as the trigger rate. Oversampling the channel at a faster capture rate offers little additional information as the adjacent impulse responses become highly correlated in time.

A number of steps were taken in the design of the CRC-MCS to ensure phase coherence between each RF chain of the receiver. Notably, within each WJ-8633 the signal undergoes an additional two-stage down-conversion using LOs generated internally to the WJ-8633. The phase of the WJ-8633 output will be dependent on the phases of these internal LOs.

Therefore, to ensure phase coherence within the system it was necessary to ensure phase coherence between these LOs. To achieve this, one WJ-8633 is configured as a master and the others slaved to it through an external LO distribution circuit. The internal LOs generated by the master are output through external ports and distributed to the slave receivers. As a result, all internal down-conversions are performed with essentially the same LO signal.

As in the transmitter, it is necessary to ensure that the sampling clocks are synchronized across each A/D card. Again, a 50 MHz clock signal is generated from the 10 MHz reference standard and supplied to the external clock input of each A/D card.

To synchronize the acquisition timing of each snapshot an external trigger signal is supplied to each A/D. The trigger signal is generated using an Altera FPGA. DIP switches on the FPGA board allow the user to program the trigger rate to a value from 1 Hz to 1500 Hz. Again, the trigger signal is derived directly from the rubidium 10 MHz reference.

The CRC-MCS receiver also integrates a GPS antenna for logging position information. When enabled, and the GPS signal is available, all acquired data are tagged with the current longitude and latitude before being stored to file. As in the transmitter, the GPS information is unreliable in the measurement environments considered within and therefore, not used.

Receiver Control Software

The main GUI of the CRC-MCS control software is shown in Figure 2.7. The graphical interface allows the user to operate in one of three modes: a general acquisition mode; an impulse response (IR) acquisition mode; and the data acquisition mode. In the general acquisition mode the time series and spectrum of the acquired data are displayed in real-time while in IR acquisition mode the channel impulse responses are displayed. The general acquisition mode is mainly used as a development and debugging tool while the IR mode is useful for doing power surveys of a measurement area prior to starting a series of channel acquisitions. In the data acquisition mode the captured data are tagged and streamed to files on each of the acquisition PCs. No significant processing of the data occurs in this mode.

The control software operates using a master-slave paradigm. One of the measurement PCs operates as the master or control PC and runs a control GUI through which the user can access a set of configuration dialog windows that encapsulates the settings for all WJ-8633s (Figure 2.8) and A/D cards (Figure 2.9 and Figure 2.10). The master PC is connected directly to each WJ-8633 and any configuration changes made by the user are written directly to each device. Control of the ICS652 A/D cards is more complicated as each card resides on a separate PC. For these cards, the control software uses a series of remote procedure calls to start server applications on each measurement PC. These server applications provide an

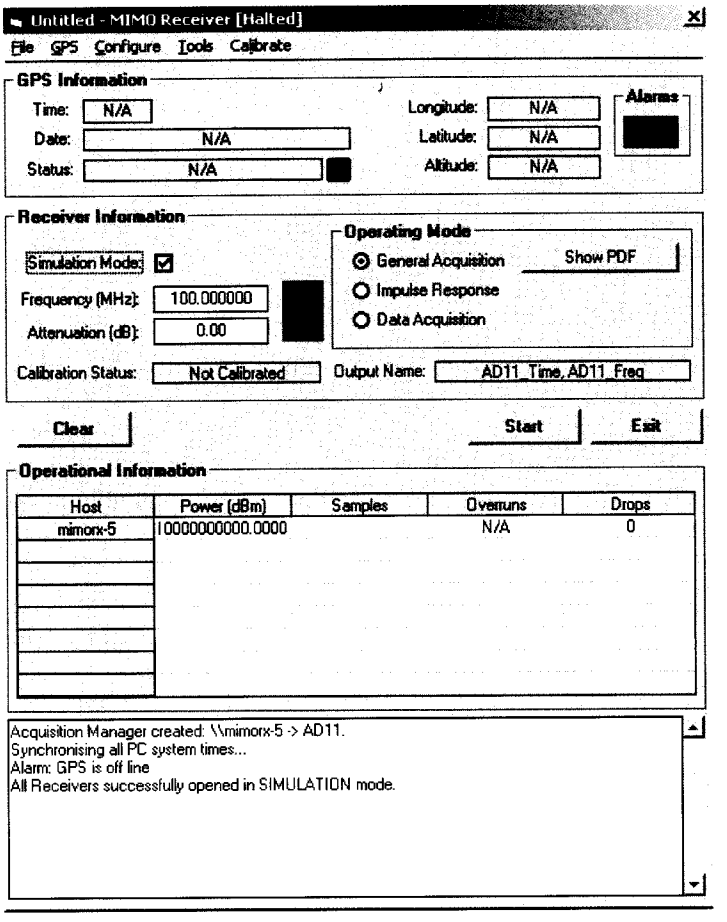

Figure 2.7: The CRC-MCS receiver control software main window.

interface layer between the control GUI and the A/D cards through network connections. Any configuration changes made by the user are sent to the slaved measurement PCs through the Ethernet connection which also allows the slave PCs to send back diagnostic data, such as measured signal strength and acquired sample counts, to the control GUI.

As in the transmitter the receiver control software allows the user to save and load the systems configuration settings to and from a workspace file.

2.1.3 Antennas

A typical set of measurements, performed with the CRC-MCS, uses arrays of drooping radial monopole antennas at both the transmitter and the receiver. However, for the measurements presented within, the receiver was modified to use dual-polarized patch antennas.

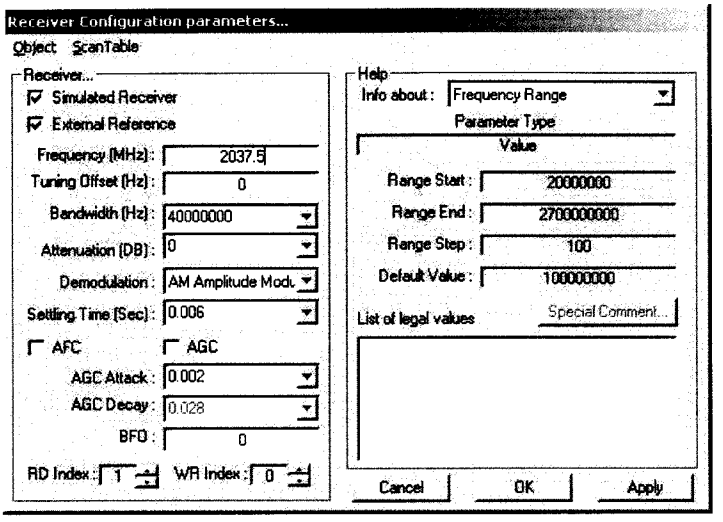

Figure 2.8: The CRC-MCS WJ-8633 configuration window.

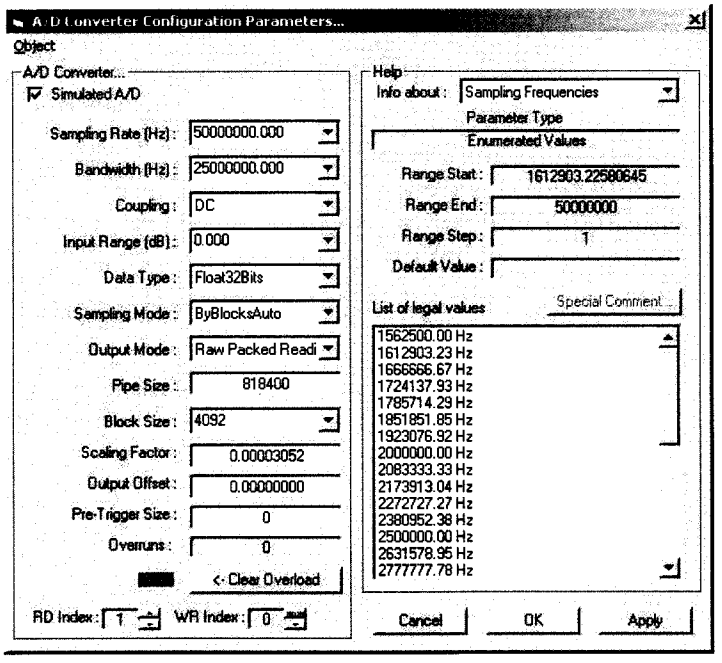

Figure 2.9: The CRC-MCS configuration window for general A/D settings.

Drooping radial monopoles

At the transmitter, eight drooping radial monopole antennas, shown in Figure 2.11, were aligned linearly and spaced by one wavelength to form the transmit array. The drooping radial antennas were designed and built at CRC and consist of a vertically mounted quarter-

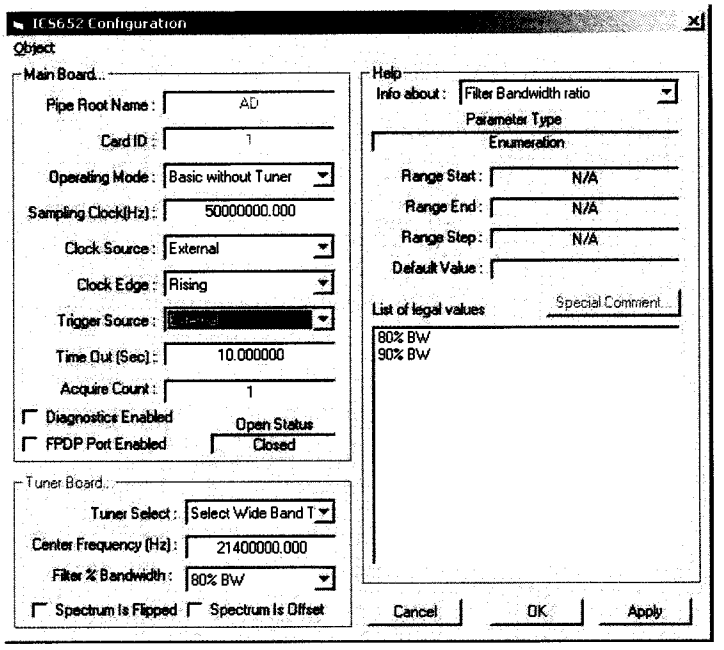

Figure 2.10: The CRC-MCS configuration window for ICS652 specific settings.

wavelength radiating element and four drooping radials which act as the ground plane. Drooping radials are well suited for measurements since the built-in ground plane allows the antennas to be easily mounted on a mast without affecting the shape of the radiation pattern [39]. These antennas are vertically polarized and have an isotropic radiation pattern. When the antennas are built the radiating element is cut slightly longer than required. Each antenna is manually tuned to the 2.0375 GHz centre frequency by monitoring the antenna's return loss (S11 parameter) on a network analyzer. The length of the radiating element is slowly trimmed until the return loss is minimized at the measurement centre frequency.

Dual polarized patch antennas

At the receiver, two linear arrays with elements separated by one wavelength, were attached to the driver and passenger sides of the measurement vehicle. Each array element was a dual linearly polarized patch antenna as shown in Figure 2.12. These antennas were designed and built by the Advanced Antenna Technology group at CRC to have a wide beam width and good isolation characteristics between vertical and horizontal ports. The specifications for these antennas are given in Table 2.1.

To facilitate mounting of the antennas, individual aluminum mounts were created to hold each patch antenna along with the integrated RF switching circuitry discussed below. The radiating side of the antennas was covered with an electromagnetically invisible plastic cover.

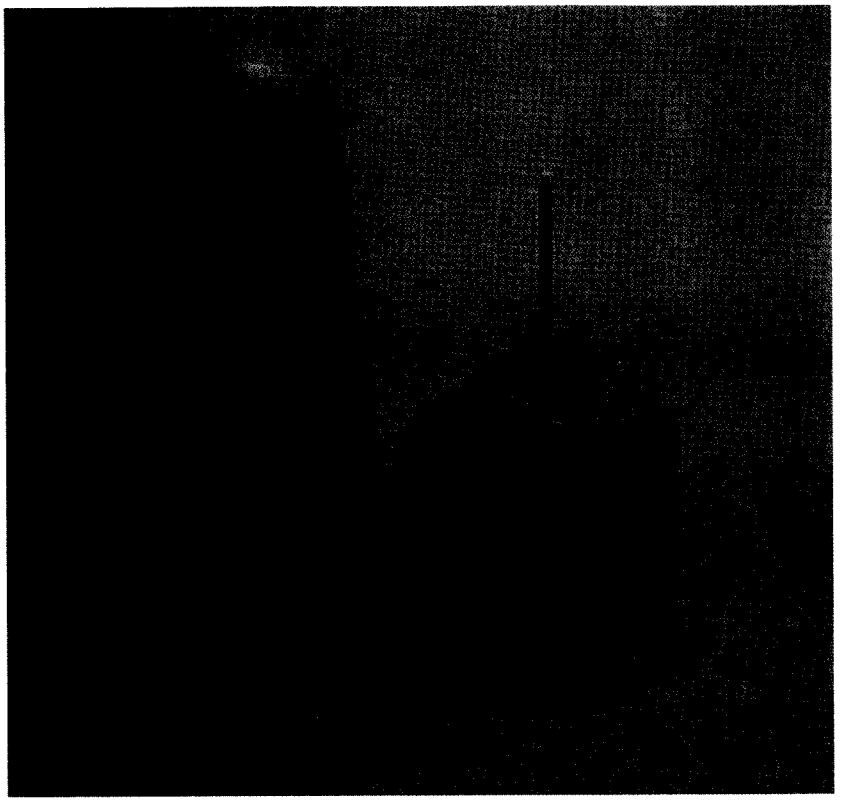

Figure 2.11: Drooping radial monopoles used at the transmitter.

	Min	Typical	Max	Units
Return loss (worse case)	14	15	16	dB
Isolation (worse case)	29	35	40	dB
Antenna gain	8.0	8.5	8.8	dBi
E-Plane 3 dB beam width	70	72	74	deg
H-plane 3 dB beam width	78	80	83	deg
E-Plane 10 dB beam width	133	134	-	deg
H-plane 10 dB beam width	144	145	147	deg
X-pol level (with respect to beam peak)	17	18	19	dB

Table 2.1: Dual linearly polarized patch antenna specifications.

Dual linearly polarized patch antenna specifications [40].

Three powerful rare-earth magnets, inset into the back of the antenna casings, were used to attach the antennas to the sides of the mobile. Each antenna was mounted such that the vertical polarization was perpendicular to the earth while the horizontal polarization was parallel.

Polarization Switching

Since the CRC-MCS was not designed to operate with dual-polarized antennas, i.e. antennas with two outputs, modifications had to be made to enable it to receive on each polarization without reducing the number of array elements from eight to four. This was a two-part modification involving: 1) RF switches at each antenna to allow the receiver to alternately record data on the vertical and horizontal polarizations; 2) circuitry to synchronize the RF switch control signals with the acquisition triggers.

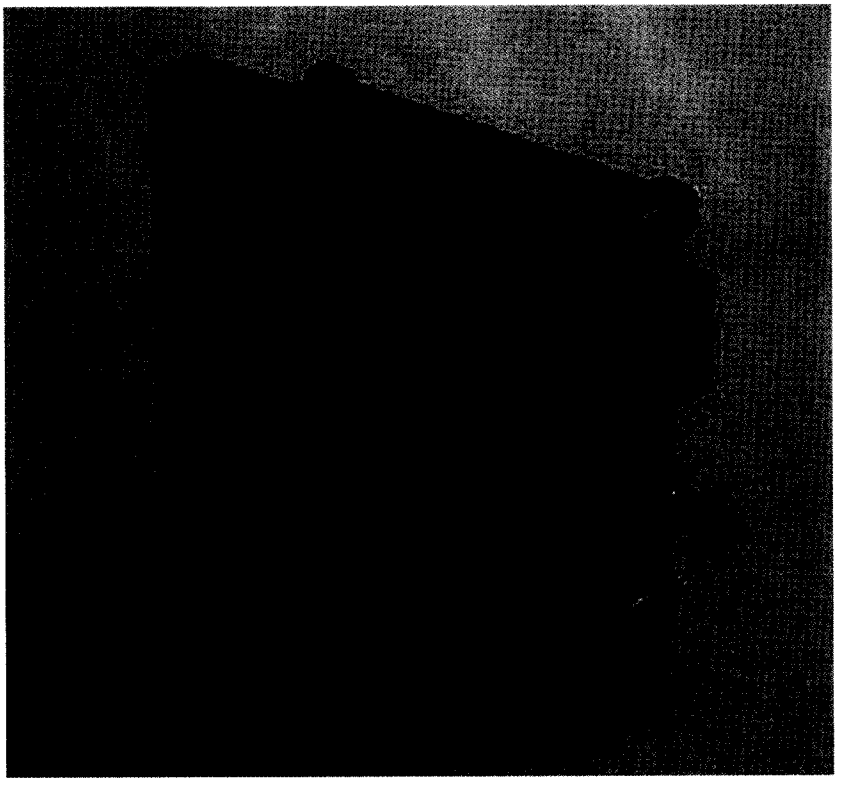

Figure 2.12: Dual-polarized patch antenna. The RF switch is mounted to the back of the antenna.

The RF switches, shown in Figure 2.13, allow the receiver to toggle between the vertically or horizontally polarized antenna ports while collecting data. As shown in Figure 2.14, these switches have very low insertion loss (top) and excellent isolation between input ports (bottom). The insertion loss (IL) on each input port is approximately 2 dB. Since these switches are positioned at the receiver front-end, directly after the antenna but before the low noise amplifier (LNA), any IL in the switch translates directly to an increase in the system's noise figure. Although not ideal, some IL is unavoidable and 2 dB does not result in a drastic increase to the system's noise figure.

The port isolation determines the amount of power coupled from one input port into

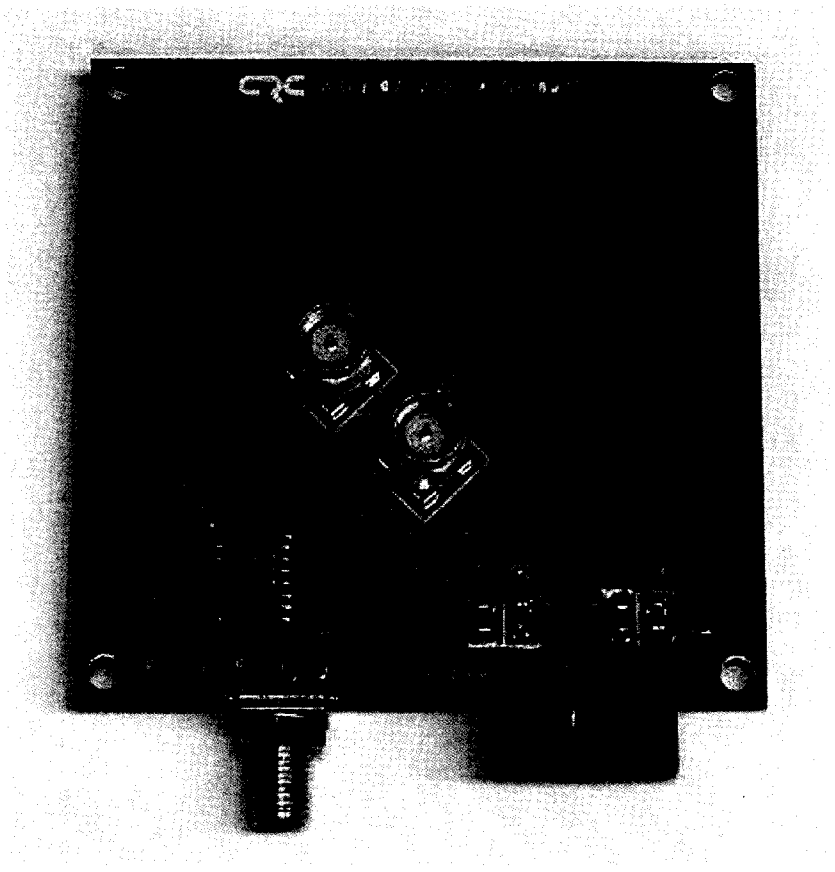

Figure 2.13: RF switch for dual-polarized patch antennas.

the other. For example, when the receiver is measuring the vertically polarized antenna output, the port isolation will determine the amount of horizontally polarized signal also being measured. The switch has good performance with approximately 35 dB and 40 dB of isolation depending on which port is enabled.

Because a single receiver chain was used to measure two antenna outputs the RF switch was toggled between input ports before each acquisition. The switching time was measured by applying a different sinusoidal signal to each switch input port and measuring the output as the switch was toggled. The transition time could then be calculated from the measured data. Figure 2.15 shows a typical result. These measurements were made at 50 Msamp/s so the transition time of approximately 5 sample periods is about 100 ns.

To ensure that the switch is settled by the time each acquisition begins the control signals operating the RF switches are synchronized with the acquisition trigger such that the switch is toggled between polarizations 200 ns in advance of the trigger signal. This allows the transient behaviours of the switches to settle before the signal is sampled. As illustrated

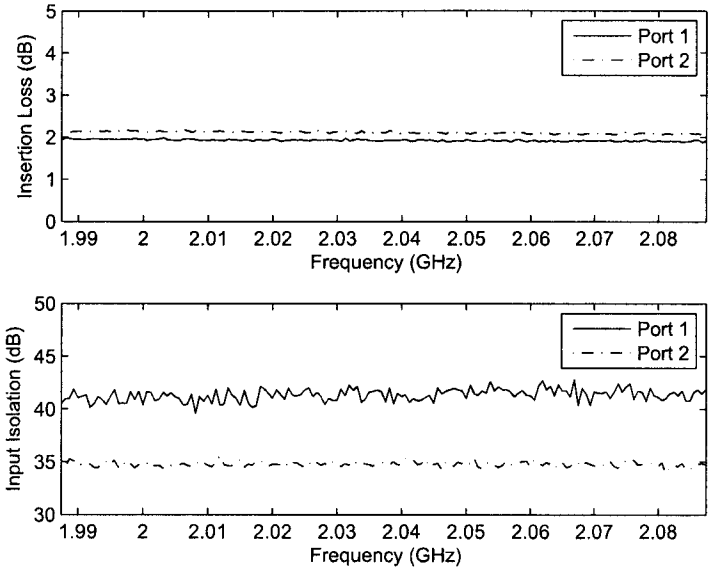

Figure 2.14: RF switch insertion loss (top) and port isolation (bottom).

in Figure 2.16, the resulting data files consist of an alternating sequence of vertically and horizontally polarized samples.

Since each polarization was sampled on every second assertion of the trigger, the acquisition trigger rate was increased to 500 Hz thus each polarization was sampled at 250 Hz. Although not sampled simultaneously, there is only a 2 ms offset between captures of each polarization which is much less than the coherence time, observed to be more than 10 ms (see Section 2.1.2). For the analysis presented herein we assume the channel is static over this time frame and each polarization is considered to be sampled simultaneously.

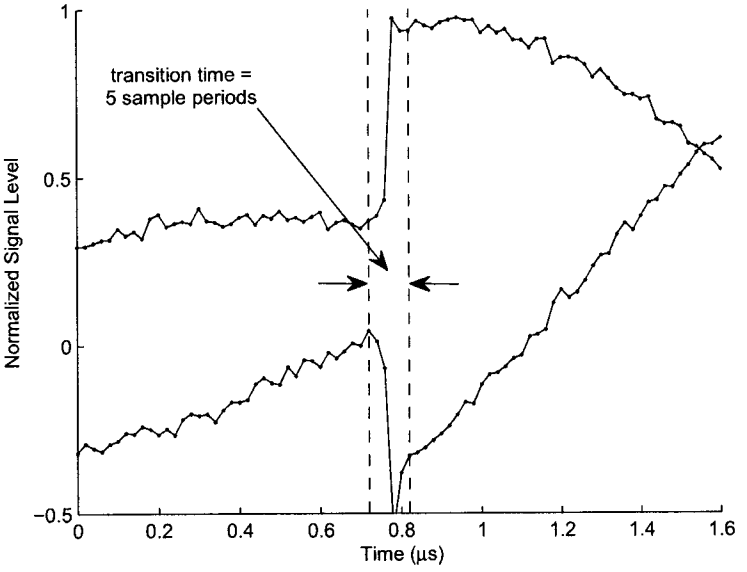

Figure 2.15: The transition time of the RF switch was measured to be approximately 100 $ns = \frac{5\ samp}{50\ Msamp/s}$.

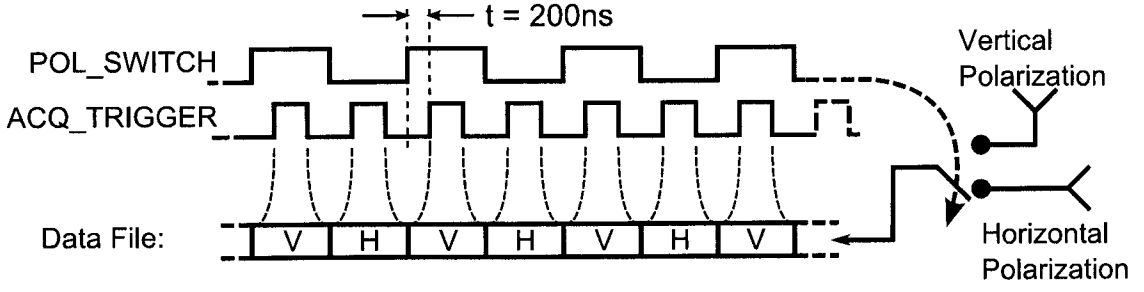

Figure 2.16: Timing diagram for dual polarization RF switch. POL_SWITCH selects between the vertical and horizontal antenna polarization. When ACQ_TRIGGER is high the signal on the selected polarization is sampled and stored to the data file.

2.2 Measurement Campaign

Channel measurements were performed in downtown Ottawa, Canada using the system discussed in Chapter 2. The measurement areas were urban streets generally lined by a dense distribution of tall office and apartment buildings. All measurements were performed around midday, during these times the traffic levels are considered moderate to high. A map of the measurement area indicating the location of the transmitter and the measurement routes is given in Figure 2.17.

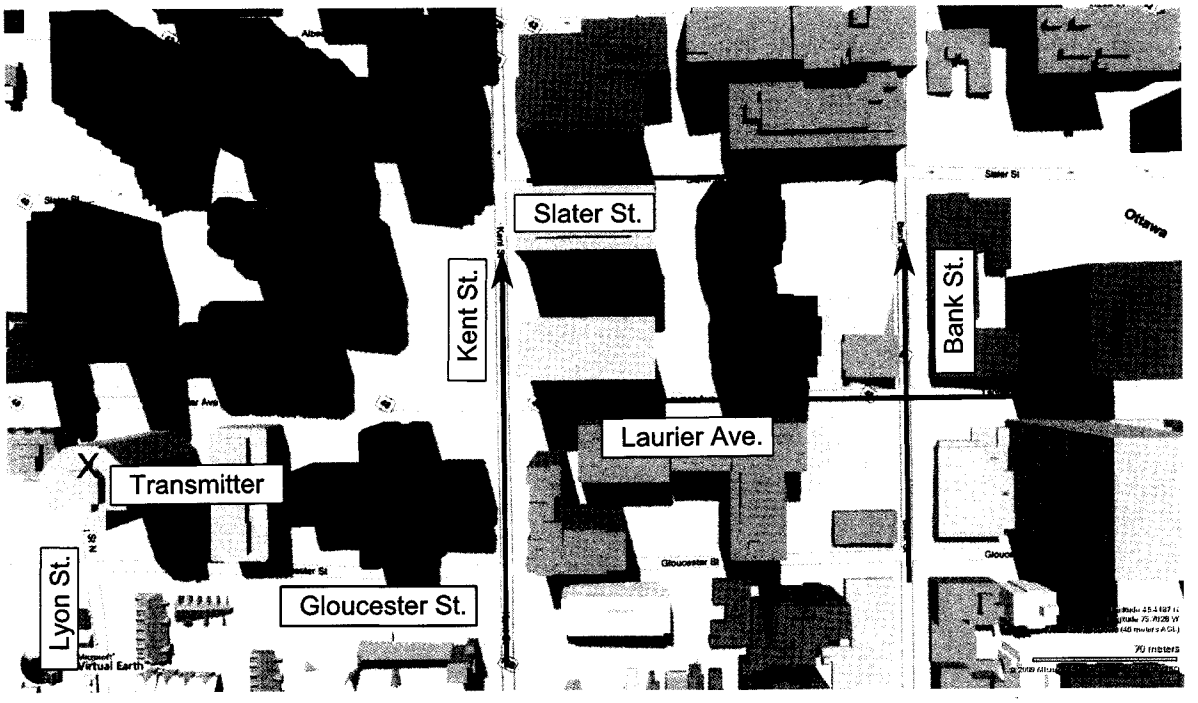

Figure 2.17: Map of measurement locations in downtown Ottawa. Note: the transmitter location is on the east side of Lyon St. with the array about 3m above street level.

The transmitter was mounted in a small trailer which was parked on Lyon St. next to the building indicated in Figure 2.17. The transmitter array, shown in Figure 2.18, consisted of eight VP drooping radial monopoles with one wavelength spacing arranged linearly. The array was mounted on a mast at approximately 3 m from the street level such that the axis of the array was perpendicular to the street.

The mobile receiver was mounted in a passenger van and a linear array was located on both the driver and passenger sides. Each array consisted of four dual-polarized patch antennas, as discussed in Section 2.1.3, with 1λ spatial separation. The driver side array is shown in Figure 2.19.

Figure 2.20 illustrates the measurement process. At the transmitter, vertically polarized

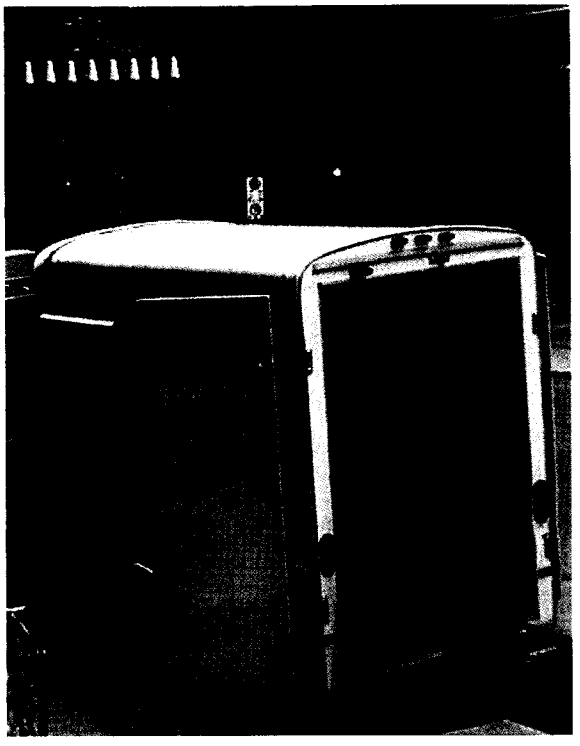

Figure 2.18: Linear array of drooping radial monopole antennas with one wavelength spacing located at the transmitter.

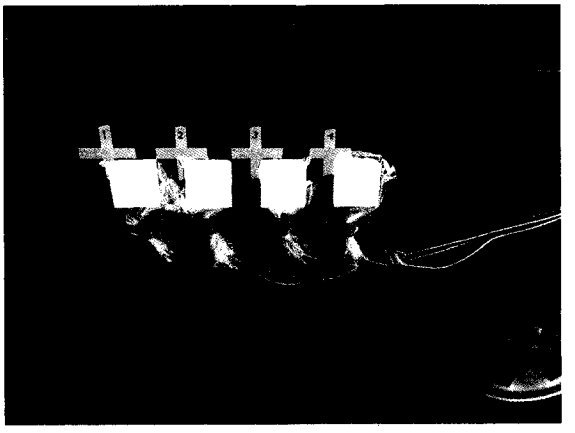

Figure 2.19: Linear array of dual-polarized patch antennas with 1λ spacing located on the driver side of the measurement van. An identical array was positioned on the passenger side.

signals are radiated into the wireless channel from the eight element linear array. As the transmitted signals propagate through the wireless channel, reflection, scattering and diffraction causes depolarization. At the receiver, the orthogonal polarizations of the depolarized channels are measured by the array elements mounted along the driver and passenger sides of the mobile. The VP and HP channels measured at elements 1, 2, 3, and 4 on the driver side are given by the 4×8 matrix of channel coefficients $\mathbf{H}_d^V$ (2.1) and $\mathbf{H}_d^H$ (2.2), respectively. Similarly, $\mathbf{H}_p^V$ (2.3) and $\mathbf{H}_p^H$ (2.4) are 4×8 matrices consisting of the VP and HP channels measured at elements 5, 6, 7, and 8 of the passenger side array.

$$\mathbf{H}_d^V(t) = \begin{bmatrix} \alpha_{11}^V(t) & \dots & \alpha_{1N}^V(t) \\ \alpha_{21}^V(t) & \dots & \alpha_{2N}^V(t) \\ \alpha_{31}^V(t) & \dots & \alpha_{3N}^V(t) \\ \alpha_{41}^V(t) & \dots & \alpha_{4N}^V(t) \end{bmatrix} \tag{2.1}$$

$$\mathbf{H}_d^H(t) = \begin{bmatrix} \alpha_{11}^H(t) & \dots & \alpha_{1N}^H(t) \\ \alpha_{21}^H(t) & \dots & \alpha_{2N}^H(t) \\ \alpha_{31}^H(t) & \dots & \alpha_{3N}^H(t) \\ \alpha_{41}^H(t) & \dots & \alpha_{4N}^H(t) \end{bmatrix} \tag{2.2}$$

$$\mathbf{H}_p^V(t) = \begin{bmatrix} \alpha_{51}^V(t) & \dots & \alpha_{5N}^V(t) \\ \alpha_{61}^V(t) & \dots & \alpha_{6N}^V(t) \\ \alpha_{71}^V(t) & \dots & \alpha_{7N}^V(t) \\ \alpha_{81}^V(t) & \dots & \alpha_{8N}^V(t) \end{bmatrix} \tag{2.3}$$

$$\mathbf{H}_p^H(t) = \begin{bmatrix} \alpha_{51}^H(t) & \dots & \alpha_{5N}^H(t) \\ \alpha_{61}^H(t) & \dots & \alpha_{6N}^H(t) \\ \alpha_{71}^H(t) & \dots & \alpha_{7N}^H(t) \\ \alpha_{81}^H(t) & \dots & \alpha_{8N}^H(t) \end{bmatrix} \tag{2.4}$$

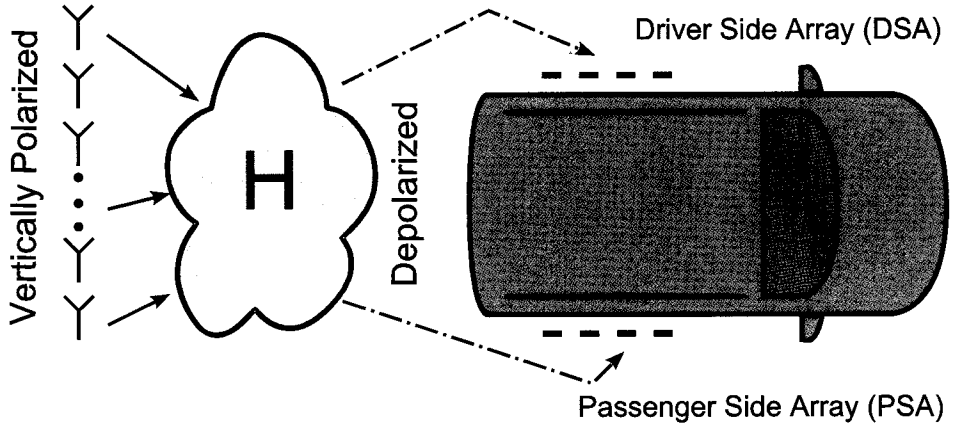

Figure 2.20: High level illustration of the polarized MIMO channel measurement process.

The investigation presented within this report focuses on the data collected as the measurement vehicle was driven along the four measurement routes labeled Laurier Ave., Slater St., Kent St. and Bank St. On each route there is no direct line-of-sight path from the transmitter to the receiver. However, the nature of the street canyons often limits the angles from which multipath components arrive at the receiver resulting in channels which sometimes exhibit specular behaviours.

On the Laurier Ave. and Slater St. measurements, the vehicle was moving away from the transmitter passing through the Kent St. intersection and, in the Laurier Ave. measurement, the Bank St. intersection. On these two routes, a steady decline received signal strength is observed. On the Bank St. and Kent St. routes, the vehicle is moving north, tangential to the transmitter, passing through the Gloucester St. and Laurier Ave. intersections. These routes exhibit significant increases in signal strength as the mobile enters the intersections.

Much of the analysis contained within this thesis involves calculation of the expectation over a number of channel instances. For such a calculation it is important to use enough channel samples such that the expectation is accurate, but few enough samples such that the channel remains wide sense stationary over the time duration considered [41]. Visual

inspection of the channel fading envelopes indicates that averaging over about 10 wavelengths of data leads to an accurate estimation of the means. Traveling at approximately 30 km/h and operating at a frequency of about 2 GHz with a channel capture rate of 250 Hz, 10 wavelengths is roughly equivalent to 40 samples which is, unless noted otherwise, the length of data generally used for the analysis contained within.

Chapter 3

8x8 Polarized Channel Characteristics

As discussed in Section 2.2, measurements using the CRC-MCS were performed along four streets in downtown Ottawa. To begin the investigation of the polarized channels in these environments we start with a general discussion of some key characteristics for both polarized channels and MIMO systems: the received power, the cross polarization discrimination (XPD) and the diversity measure.

3.1 Cross Polarization Discrimination

The XPD is a measure of the coupling between orthogonal polarizations and is the ratio of the powers received on each polarization with respect to a given polarization at the transmitter. For a multielement system with transmit and receive polarizations defined as vertical and horizontal the XPD between the n^{th} vertically polarized transmit antenna and the m^{th} dual-polarized receive element is given by

$$XPD_{mn}^{V} = \frac{E\left\{|\alpha_{mn}^{VV}(t)|^2\right\}}{E\left\{|\alpha_{mn}^{HV}(t)|^2\right\}}, \tag{3.1}$$

where $\alpha_{mn}^{VV}(t)$ is the fading coefficient between the VP transmit and receive elements and $\alpha_{mn}^{HV}(t)$ is the fading coefficient between the VP transmit element and the HP receive element. Similarly, the horizontal XPD is defined with respect to HP transmit power as the ratio of power received on the HP to the VP such that

$$XPD_{mn}^{H} = \frac{E\left\{|\alpha_{mn}^{HH}(t)|^2\right\}}{E\left\{|\alpha_{mn}^{VH}(t)|^2\right\}}. \tag{3.2}$$

For the measurements discussed within, all transmitted signals are vertically polarized. Thus, to simplify the notation, the second superscript on the α's is dropped and (3.1) is rewritten as

$$XPD_{mn}^{V} = \frac{E\left\{|\alpha_{mn}^{V}(t)|^2\right\}}{E\left\{|\alpha_{mn}^{H}(t)|^2\right\}}. \tag{3.3}$$

The XPD quantifies the extent to which a transmitted signal becomes depolarized. When reported in decibels, a positive XPD^V indicates that only a fraction of the VP transmitted signal has become HP, while a negative value occurs when the majority of the signal energy has moved into the horizontal polarization.

The performance impact of cross coupling between polarizations depends upon the arrangement and polarization of the antennas. Take, for example, a system similar to the measurement scenario discussed within this report. A uni-polarized transmit array is paired with a dual polarized receive array in an attempt to reduce the array size, either by moving dual-polarized array elements closer together or by colocating them. In such a scenario, high levels of XPD indicate an insufficient level of signal depolarization resulting in lower received power at one polarization compared to the other. This is equivalent to a having a power imbalance between diversity branches and will result in a loss of diversity [16].

A high XPD, however, could be beneficial in a scenario in which a multielement system uses equal length transmit and receive arrays with spatially separated dual-polarized antennas. Again a system might be set up in this manner to reduce the spacing between array elements and thereby reduce the size of the array. If the correlation between adjacent or colocated orthogonally polarized antenna elements is high the performance of the system may still be good if the XPD is also high. When the XPD is large, power from, for example, the vertically polarized elements is very attenuated at the horizontally polarized elements and vice versa. This results the formation of separate sets of transmission channels on each polarization resulting in little interference from the cross polarized channels [35].

Although of considerable importance, the XPD has not been fully characterized in an outdoor urban environment [42]. In this chapter, some insight is developed with respect to how XPD is impacted by the channel environment and by the relative locations of the transmitter and receiver.

Empirical XPD Characteristics

For each measurement route, Figure 3.1 shows the empirical cdfs of XPD^V_{mn} aggregated from the $M \times N$ subchannels where the expectation in (3.3) is estimated from 40 channel instances. In general these channels undergo significant depolarization. The Laurier Ave. and Bank St. measurements undergo the most with 50% of the measured XPD^V values being less than 3 dB on each. The most polarized of these channels are those measured on Kent St. and Slater St. where the medians of the cdfs are just less than 5 dB.

The range of XPD values measured in urban environments are dependent on the presence of LOS and the distance between the transmitter and receiver. Generally the XPD is greater in LOS channels than NLOS [17]. LOS suburban measurements exhibited a XPD of 12 dB in [16] while in NLOS urban measurements the XPD was reported to be on the order of 7 dB

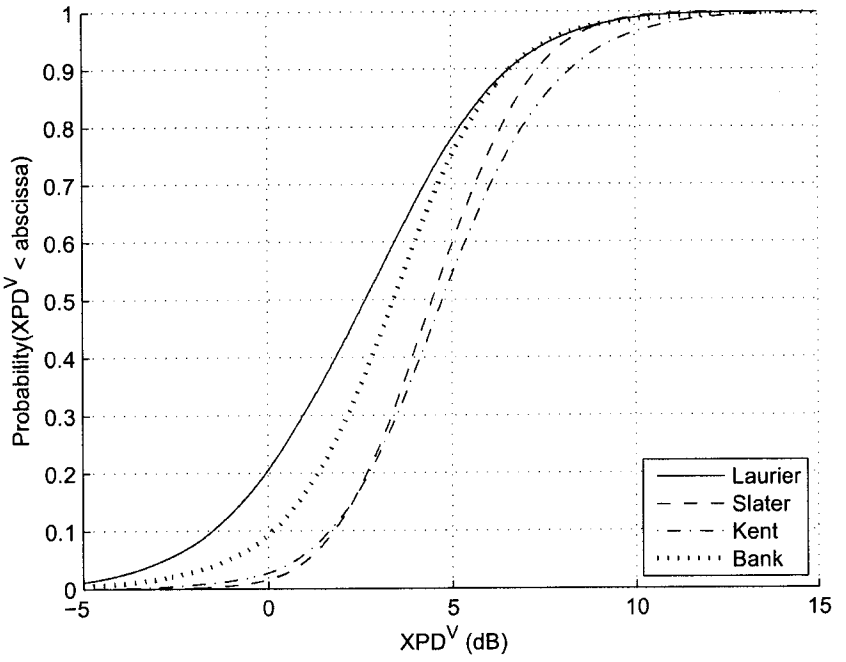

Figure 3.1: cdfs of XPD^V measured on each subchannel on Laurier Ave., Slater St., Bank St. and Kent St.

[16] and 6 dB [2], [15]. In [43], measurements were performed using mobile antennas polarized at $\pm 45°$ and the XPD in LOS channels ranged from 3-10 dB while in NLOS channels the XPD was on the order of 2 dB. In [44] an XPD of 7 dB was measured at a roof mounted antenna and 4 dB was measured at a hand held portable. Much higher XPD values of 12 dB were measured in mixed LOS and NLOS urban channels in [21]. A possible explanation for these higher values may be the short distance between the transmitter and receiver resulting in less depolarization of the transmitted signal [21] because of a lack of interactions with objects in the environment. Measurements have shown that the XPD drops as the distance between the transmitter and receiver increases. In [19] the mean XPD measured at 100 m from the transmitter dropped from 4 dB to 0 dB at 10 km. However, since the diminishing XPD is due to the depolarization of the signal due to reflection and diffraction, 0 dB is expected to be the lower limit on the mean XPD as a function of distance.

The average XPD values measured in the urban environments considered in this report fall within the 0 dB to 12 dB range depending on directional characteristics and the distance from the transmitter. These values correspond well with those measured in the previous investigations noted above.

It is important to note that the above cdfs are a generalization of the behaviour for each urban environment measured. However the impact of the immediate propagation environ-

ment often plays a critical role in determining channel behaviour at the local level. In real channels the effect of buildings, traffic and the orientation of the mobile can have significant impact on the observed channel characteristics. Further, it is often assumed that the fading coefficients of each subchannel are identically distributed. In practice however, this is often not the case [19]. The following section focuses on the variation of the measured channel characteristics in four urban environments.

3.1.1 Laurier Avenue

The Laurier Ave. measurement route is indicated in Figure 2.17. The transmitter is positioned on Lyon St. in the centre of the block between the Laurier Ave. and Gloucester St. intersections. Snapshots of the channel were collected at the receiver as the mobile moved east, away from the transmitter. For the initial 15 s and the last 7 s of the measurement the receiver is in an urban canyon formed by tall office buildings on both sides of the streets. Between 15-25 s the mobile is in or near the intersection with Bank St.

Figure 3.2 shows the average power, $\bar{P}^V$ and $\bar{P}^H$, measured on the vertical and horizontal polarizations, respectively, where

$$\bar{P}^V = E\left\{tr\{\mathbf{H}^V(\mathbf{H}^V)^\dagger\}\right\} \text{ and } \bar{P}^H = E\left\{tr\{\mathbf{H}^H(\mathbf{H}^H)^\dagger\}\right\} \tag{3.4}$$

and the expectation is calculated over 40 channel instances. On each polarization, a similar rate of power decay is measured as the mobile moves further away from the transmitter. For most of the measurement the difference in the two measured powers is less than 3 dB with the major exceptions being at the start where the difference is as high as 7 dB and as the mobile enters the second street canyon, at 20 s, where $\bar{P}^V$ is more than 4 dB greater than $\bar{P}^H$. In the portion of the measurement between 15-20 s the difference between the two measures decreases and is, for the most part, less than 2 dB.

Figure 3.3 plots the time series of the mean and the variance of the XPD measured along Laurier Ave. In each plot, the corresponding metric is estimated by averaging across the $M \times N$ subchannels such that the mean XPD^V is given by

$$\hat{\mu}_{XPD} = \frac{1}{NM}\sum_{m=1}^{M}\sum_{n=1}^{N} XPD^V_{mn} \tag{3.5}$$

and the variance of the XPD^V is estimated as

$$\hat{\sigma}^2_{XPD} = \frac{1}{NM-1}\sum_{m=1}^{M}\sum_{n=1}^{N}\left[(XPD^V_{mn})^2 - \hat{\mu}^2_{XPD}\right]. \tag{3.6}$$

In addition to showing the mean, the upper plot also contains the time series for the $XPD^V_{max} = max\{XPD^V_{mn}\}$ and $XPD^V_{min} = min\{XPD^V_{mn}\}$ values. Taken together these

plots show the variation of the XPD^V across the spatial subchannels as well as illustrating the substantial changes it undergoes over time on some of the measurement routes.

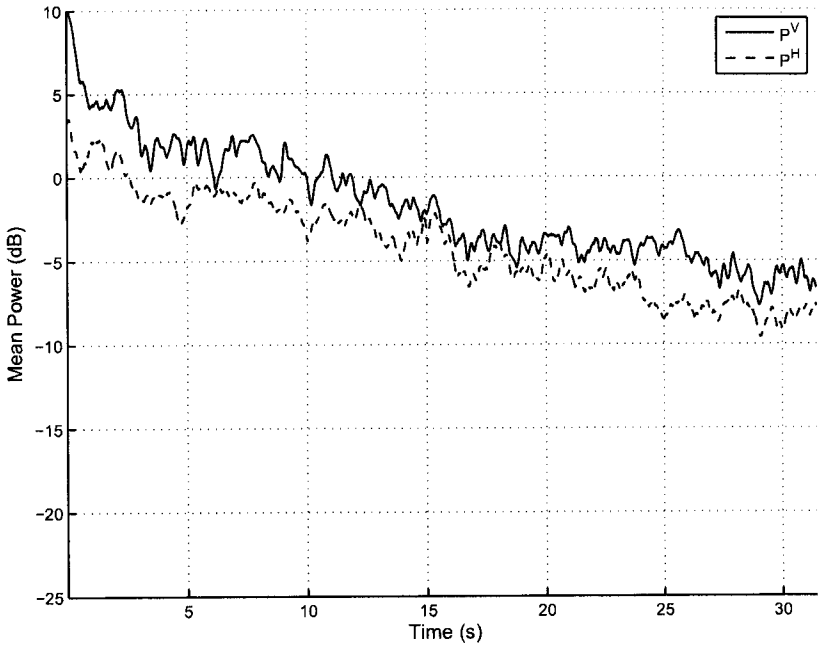

Figure 3.2: Signal power measured on Laurier Ave.

For the length of the Laurier Ave. measurement, $\hat{\mu}_{XPD}$ ranges from about 2-5 dB, however, there is considerable variation in the variance of the XPD^V across the array. For the initial 5 s the mean remains high at approximately 5 dB followed by a general downward trend reaching about 2 dB at 19 s. This is due to a drop in the $\bar{P}^V$ as the mobile approaches the Bank St. intersection. In general, the XPD^V on Laurier Ave. is less affected by the intersections than it is on the other streets, however, as the mobile enters the open area near the Laurier Ave. and Bank St. intersections it passes a number of openings between small buildings along the south side of Laurier Ave. These areas result in increased variance of the XPD (at 15 s and 20 s) as the strength of the VP and HP signals components fluctuates.

The variance of the XPD on Laurier Ave. ranges from 15 dB to -5 dB. On this set of measurements, the distribution of the XPD^V has the widest spread with 80% of the values falling within the range from -1.5 dB to 6.5 dB, indicating that for some subchannels, the strength of the VP is much greater than the HP while on other subchannels the HP receives more power.

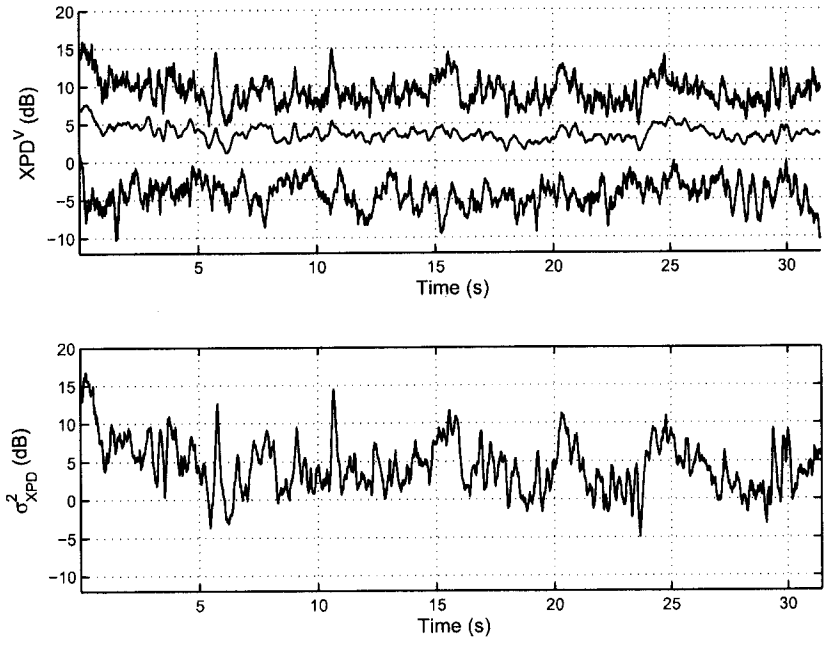

Figure 3.3: Time series of the $\hat{\mu}_{XPD}$, XPD^V_{max}, and XPD^V_{min} (top) and $\hat{\sigma}^2_{XPD}$ (bottom) measured on Laurier Ave.

3.1.2 Slater Street

The measurement route on Slater St., indicated in Figure 2.17, is similar to Laurier Ave. in that the receiver is moving east, away from the transmitter through a narrow urban canyon. However, for the Slater St. measurement the receiver does not pass through an intersection.

Plots of $\bar{P}^V$ and $\bar{P}^H$ are given in Figure 3.4. As on the Laurier Ave. measurement, the power decays on each polarization at a similar rate. On Slater St. the $\bar{P}^H$ is approximately 5 dB lower than the $\bar{P}^V$ resulting in higher XPD^V values on average than those measured on the other channels.

The time variation of the XPD^V and $\hat{\sigma}^2_{XPD}$ measured on Slater St. are shown in Figure 3.5. On Laurier Ave., about 20% of the XPD^V values measured across the subchannels are less than 0 dB. On Slater St. however, this only occurs on about 1% of the subchannels, whereas on both routes 98% of the measured values fall below 8 dB. This indicates that on Slater St. the occurrence of HP subchannels with signal levels greater than that of the corresponding VP subchannel is lower than Laurier Ave. In general, the variance on this set of measurements is lower than on the Laurier Ave. measurement with 80% of the observed XPD^V values falling within the 2-7.5 dB range.

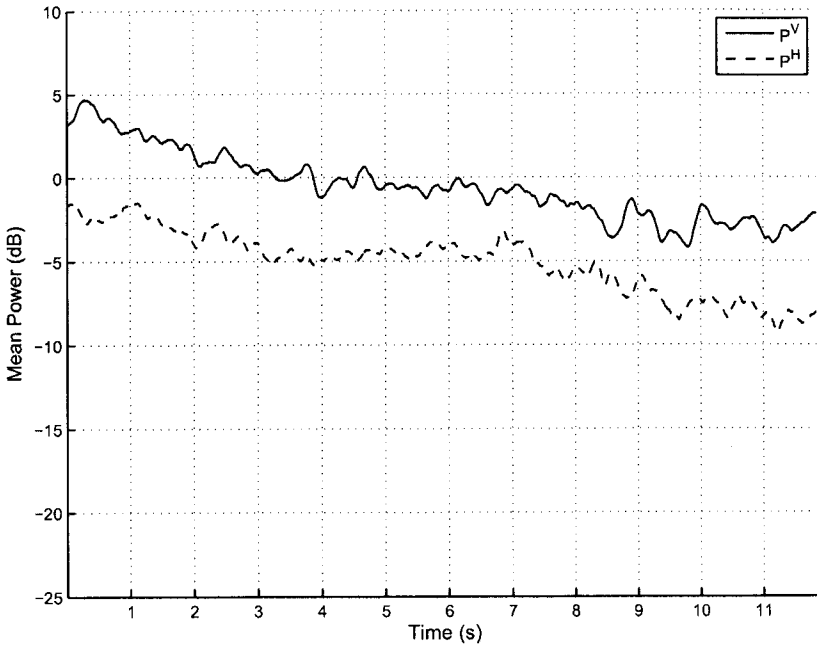

Figure 3.4: Signal power measured on Slater St.

3.1.3 Kent Street

Figure 3.6 plots $\bar{P}^V$ and $\bar{P}^H$ for the Kent St. measurement. Initially the power starts out low until the mobile approaches the open area around the intersection with Gloucester St. at around 8 s. As the mobile continues along this portion of Kent St. the power on both polarizations remains strong until, at 12 s, it begins to enter the shadow of the buildings located between Gloucester St. and Laurier Ave. Again the power drops off for the portion of time that the mobile is between intersections and shadowed by the buildings along Kent St. At about 16 s it approaches the intersection with Laurier Ave. and the power begins to increase on each polarization. The maximum power levels for the measurement are reached in the centre of the Laurier Ave. intersection between 18-20 s. As the mobile continues out of the intersection the power drops off once again.

In general the VP and HP power levels are highly correlated through the whole measurement with about a 5 dB difference between the two as indicated by the Kent St. cdf in Figure 3.1. The time series plot of the XPD^V and $\hat{\sigma}^2_{XPD}$ in Figure 3.7, however, shows the significant variations that occur on the subchannels when the mobile enters an intersection. In the Gloucester St. intersection the $\hat{\mu}_{XPD}$ increases to 10 dB and again to 8 dB in the Laurier Ave. intersection. The variance in the XPD^V across the subchannels is highest during these portions of the route. In the Gloucester St. intersection, the $\hat{\sigma}^2_{XPD}$ reaches more than 20 dB and about 18 dB in the Laurier Ave. intersection. A possible explanation for this

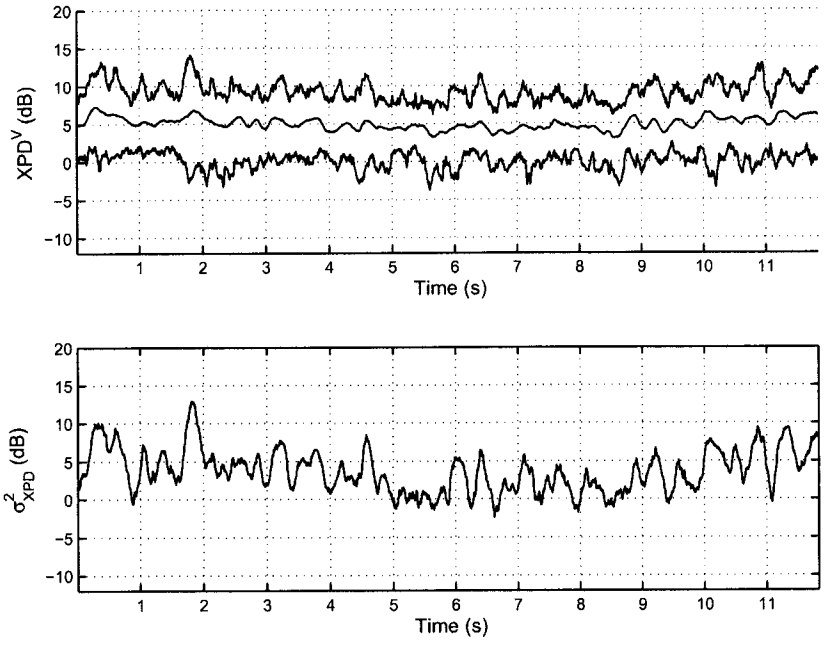

Figure 3.5: Time series of XPD measured on Slater St.

behaviour is presented in Chapter 6.

3.1.4 Bank Street

Plots of the received power for the Bank St. measurement are given in Figure 3.8. As in the Kent St. measurement, strong spikes in power on both polarizations are measured as the mobile passes through the intersections with Gloucester St., at 1 s, and Laurier Ave., at 11 s. Although the buildings surrounding Bank St. are generally lower than those on Kent St. they are still a source of significant shadowing at the mobile due to the relatively low height of the transmit and receive arrays.

For the Bank St. measurement the difference in the power on the two polarizations is less than that of the Kent St. and Slater St. measurements. In fact in the intersection with Laurier Ave. the average received power on the HP is at times equal to or greater than that of the VP. These regions, where $\bar{P}^V \approx \bar{P}^H$, exhibit large increases in $\hat{\sigma}^2_{XPD}$ as shown in Figure 3.9. As in the Kent St. measurement, the largest $\hat{\sigma}^2_{XPD}$ are measured in the intersections, however, on Bank St. the tendencies toward negative XPD^V values are much greater, reaching -10 dB at 1 s and -12 dB around 11 s.

Between intersections the variance of the XPD^V is much less than that measured within the intersections. Here the behaviour of the XPD^V is comparable to that of the Slater St. measurement.

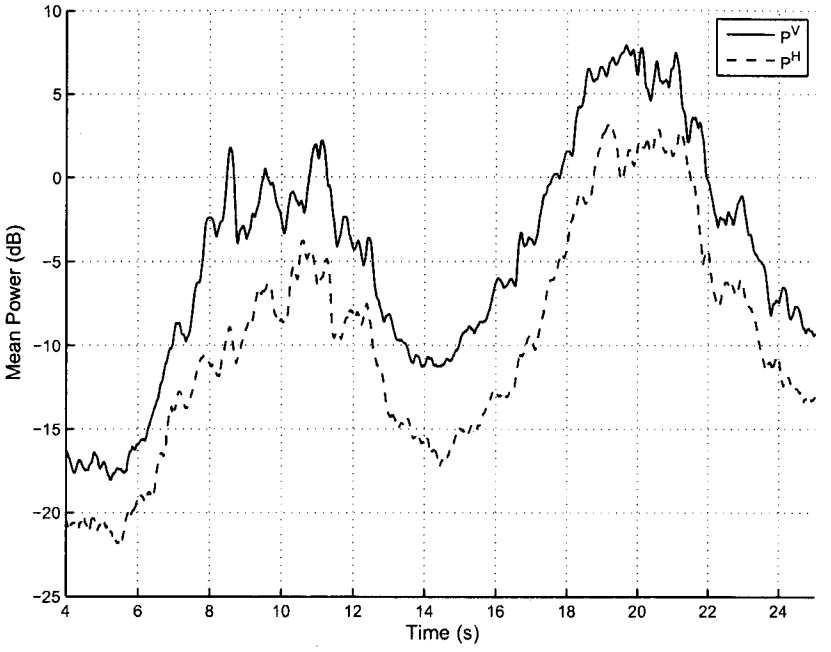

Figure 3.6: Signal power measured on Kent St.

3.2 Diversity Measure on Dual-Polarized Channels

The XPD is a key characteristic in the operation of dual-polarized communications. In the previous section the behaviour of the XPD was observed to vary considerably depending on the measurement environment and the location of the receiver relative to the transmitter. For MIMO communications the level of diversity present in the channel is also of critical importance. The design of dual-polarized MIMO systems must trade off the requirement for high diversity with the power imbalance in polarized receive branches. In this section, the channel diversity is discussed as it applies to the polarized channels measured in each measurement environment.

In [45], a method for quantifying channel diversity was introduced based on the eigenvalues of the channel's autocorrelation matrix $\mathbf{R_C} = E\left\{vec\{\mathbf{H}\}vec\{\mathbf{H}\}^\dagger\right\}$, where $vec\{\cdot\}$ is the vectorization of the matrix argument by stacking the columns on top of one another. For an 8×8 MIMO system, accurate calculation of $\mathbf{R}_c$ requires a large number of independent and stationary samples. Unfortunately, in complex urban environments assumptions of stationarity can only be made for short periods of time [41]. A modified version of this diversity measure which requires fewer samples to calculate is defined for the vertically polarized

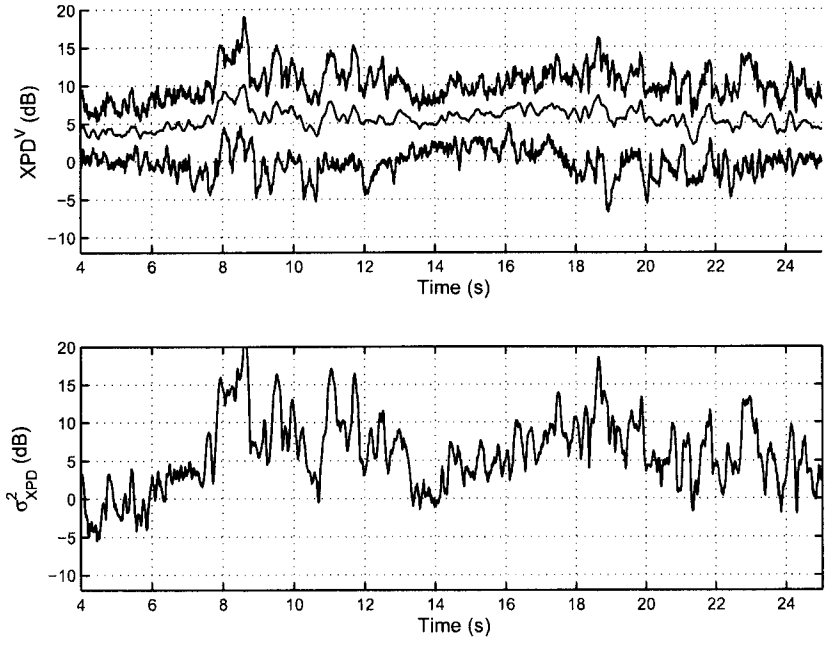

Figure 3.7: Time series of XPD measured on Kent St.

channels as [46]

$$D^V = \frac{\left[\sum_{m=1}^{M} \delta_m^2\right]^2}{\left[\sum_{m=1}^{M} (\delta_m^2)^2\right]}, \tag{3.7}$$

where δ_m^2 is the m^{th} eigenvalue of the VP received autocorrelation function $\mathbf{R}^V = E\left\{\mathbf{H}^V(\mathbf{H}^V)^\dagger\right\}$. Similarly, the diversity measure of the HP channels D^H is defined using the HP autocorrelation matrix $\mathbf{R}^H = E\left\{\mathbf{H}^H(\mathbf{H}^H)^\dagger\right\}$. The diversity measure is a quantification of the eigenvalue spread and is independent of the received power such that $D^V = 1$ indicates the subchannels are completely correlated whereas $D^V = M$ indicates the subchannels are independently distributed.

3.2.1 Time Series Diversity Measures

The diversity measures of the polarized channels captured along each measurement route are plotted in Figures 3.10 to 3.13 and the mean and standard deviation for both the D^V and D^H are summarized in Table 3.1. On Laurier Ave. (Figure 3.10) both the D^V and D^H are low with the D^H generally being less than or equal to the D^V especially between the times 10-20 s.

The low diversity measure on Laurier Ave. is indicative of channels with significant cor-

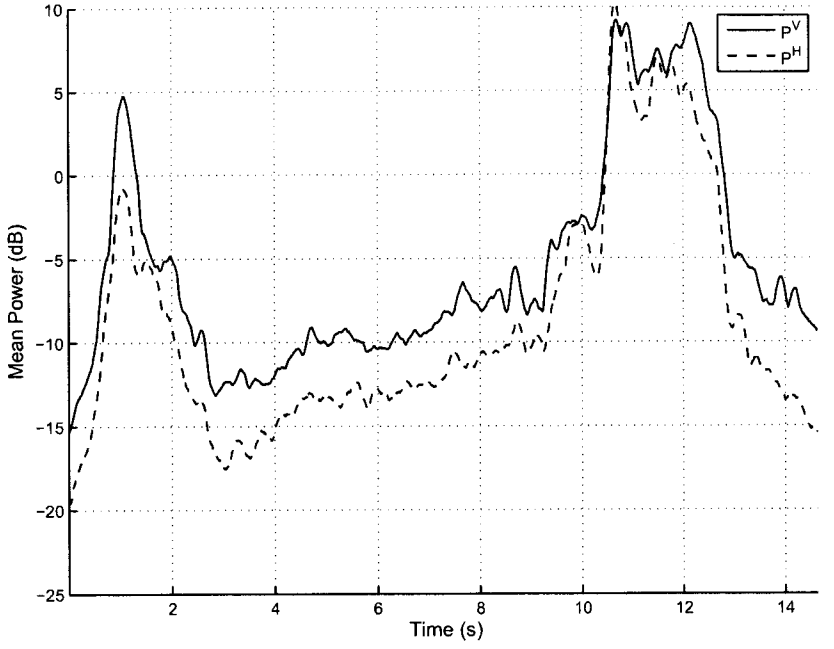

Figure 3.8: Signal power measured on Bank St.

relation among the subchannels at the receiver. The diversity measure will be maximized when a large number of multipath components arrive from all around the receive array. In such a scenario the distribution of energy across the eigenvalues of the autocorrelation matrix will be more uniform. However, when the arriving signal is dominated by a small number of multipath components (or groups of multipath components with a narrow angular spread) the majority of the received power will be contained within one or two of the eigenvalues. This results in a low diversity level as is observed in the Laurier Ave. measurements.

The diversity measure on Slater St. (Figure 3.11) is moderately high with average values around 5 for each polarization. For the first 5 s of the measurement the D^H is generally greater than that of the D^V while for the rest of the measurement the two measures are roughly equivalent. In the last 4 s of the measurement there is a decline in both the D^V and D^H. As opposed to the Laurier Ave. measurement, the diversity on Slater St. indicates significantly lower levels of subchannel correlation and a greater number of received multipath components.

The diversity measures on Laurier Ave. and Slater St. contrast significantly to those measured on Kent St. shown in Figure 3.12 and Bank St. in Figure 3.13. As was observed in Figure 3.6 and Figure 3.8 the intersections of Gloucester St. and Laurier Ave. act as significant sources of energy for Kent St. and Bank St. On each measurement the D^V and D^H are roughly equivalent with high diversity levels in the channels measured between

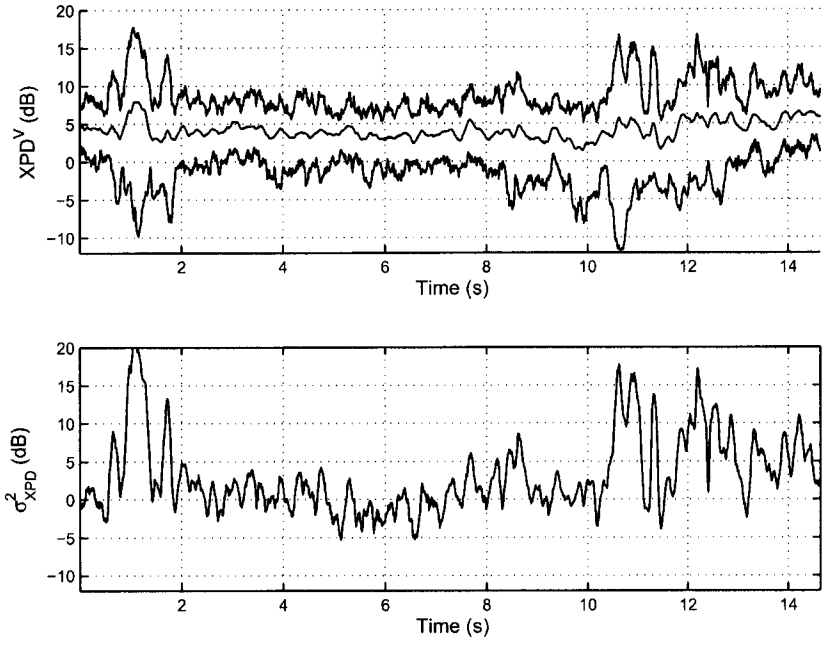

Figure 3.9: Time series of XPD measured on Bank St.

the intersections. In these regions, the mobile is receiving energy as it radiates out of both the Gloucester St. and Laurier Ave. intersections and, as a result, the number of dominant multipath components is fairly large. In the intersections, however, the arriving signal components are dominated by the energy radiating out of the Gloucester St. and Laurier Ave. street canyons resulting in decreased diversity levels and higher subchannel correlation.

On Kent St. it is interesting to note that as the mobile approaches the Gloucester St. intersection between 6-8 s the power increase on both the VP and HP is marked by a decrease in diversity as the strong directional component from the street begins to dominate. However, in the 8-9 s period the increase in $\bar{P}^H$ slows while the $\bar{P}^V$ continues to rise. It is possible that the propagation environment in this area is not as favourable to depolarization as it is in other areas along the measurement route, resulting in lower levels of $\bar{P}^H$. However, during this time period, the decreasing D^H is punctuated by portions of high diversity measuring between 5 and 6 suggesting a possible explanation for the reduced average signal power may be increased multipath fading due to increased scattering.

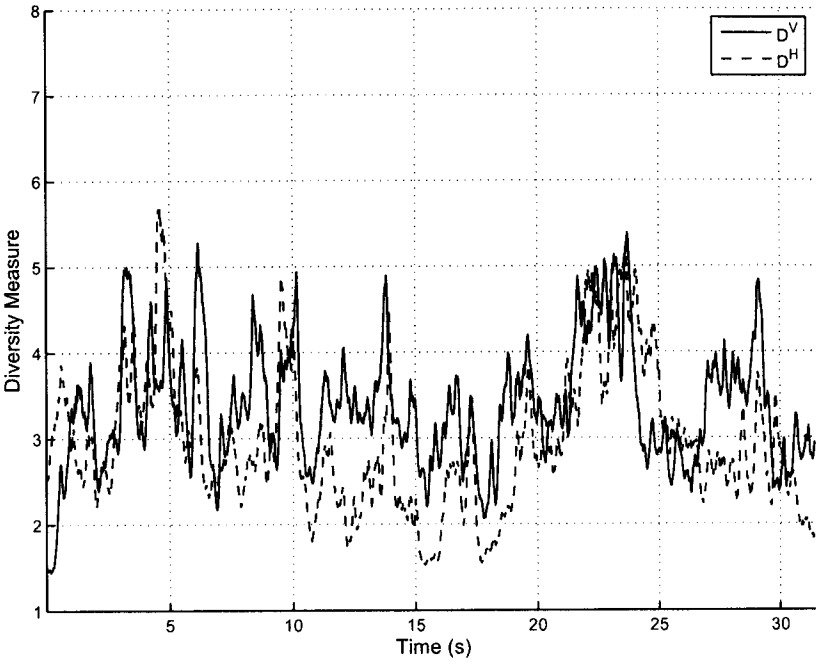

Figure 3.10: The time series of the diversity measure observed on polarized channels along Laurier Ave.

	D^V		D^H	
	mean	std.	mean	std.
Laurier Ave.	3.7	0.7	3.0	0.8
Slater St.	5.1	1.0	5.6	0.7
Kent St.	4.1	1.7	4.3	1.8
Bank St.	4.3	1.8	4.4	1.9

Table 3.1: Mean and standard deviation (std.) of the diversity measure on Laurier Ave. and Slater St.

Summary

In this chapter the polarized channel characteristics measured on four urban streets were discussed. The measurements on Laurier Ave. and Slater St. were in urban canyons with the receiver moving away from the transmitter. On both measurements, a steady decline in received power was observed on both polarizations, however, each environment exhibited unique XPD characteristics. On Laurier Ave. the XPD^V was on average lower than on Slater St. but the variation of the values across the subchannels was greater. On Slater St., the diversity was higher than on Laurier Ave. indicating that the received signal generally consisted of a greater number of multipath components.

The Kent St. and Bank St. measurements transitioned between urban canyons and inter-

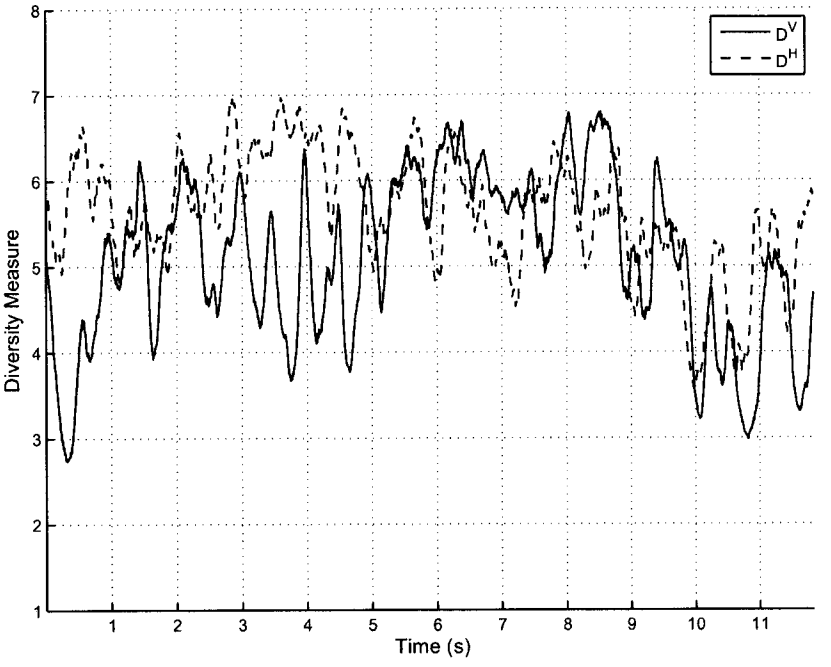

Figure 3.11: The time series of the diversity measure observed on polarized channels along Slater St.

sections. On these measurements it was observed that in the intersections the received signal was dominated by power arriving from Gloucester St. and Laurier Ave. In these areas the mean and variance of the XPD^V increased while in the areas with greater shadowing from surrounding buildings the variance in the XPD^V was reduced and the diversity increased.

As already discussed, the diversity performance of a given channel is dependent on the richness of the multipath environment. Where the number of strong multipath components is high the correlation among the subchannels will be minimized and the diversity will also be high. However, in environments where a small number of multipath components dominate the received signal diversity will be reduced. In the following chapter, the angular distribution of energy in each of the measurement environments is analyzed. By observing the angular range over which energy is received, insight can be gained into possible causes for the differences in channel characteristics.

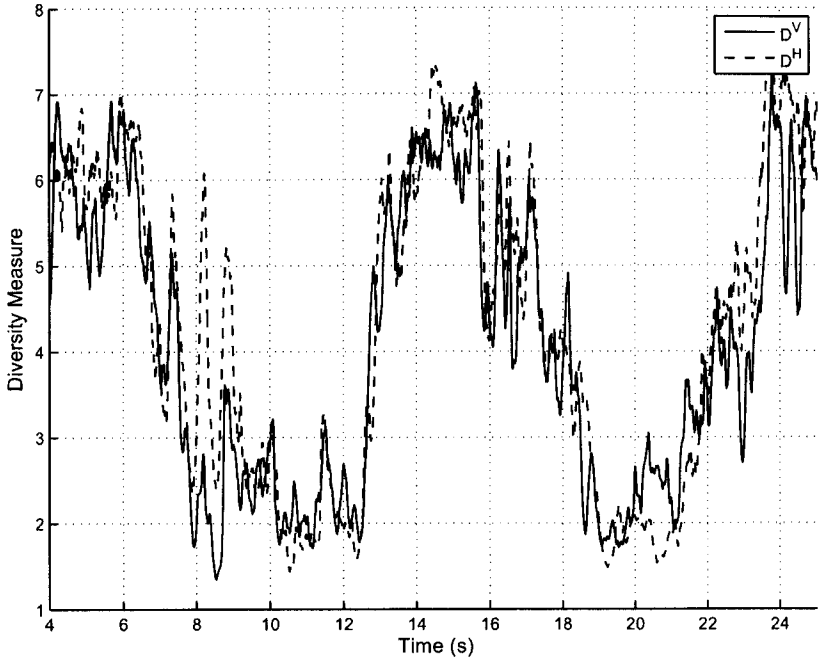

Figure 3.12: The time series of the diversity measure observed on polarized channels along Kent St.

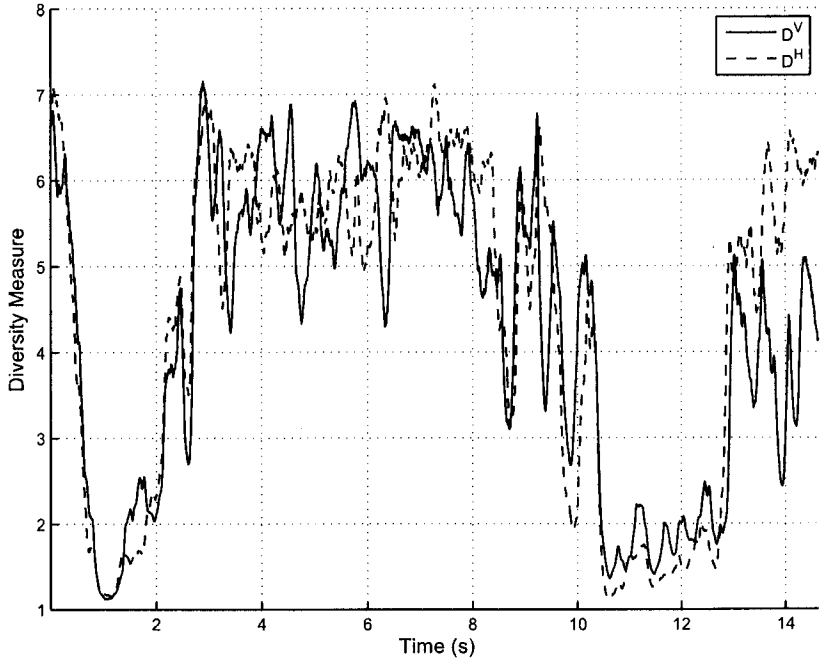

Figure 3.13: The time series of the diversity measure observed on polarized channels along Bank St.

Chapter 4

Angular Distribution of Multipath Components

In a communications system based upon exploiting diversity, the number of multipath components and the range of angles from which they arrive at the receiver have a significant impact on the system's performance. When the multipath components are uniformly distributed over the full angular range of the receive array, diversity will be maximized. However, when the angular distribution is limited by the nature of the environment, e.g., when a dominant directional component is present, diversity will be diminished and the system performance will degrade. This chapter investigates the angular distribution of the polarized multipath components in each of the measurement environments.

4.1 Minimum Variance Distortionless Response Beamformer

The angular distribution of the multipath components are estimated using the minimum variance distortionless response (MVDR) beamformer, also known as the Capon beamformer [47].

The output $\mathbf{x}$ of a multi-element array can be modeled by

$$\mathbf{x} = \mathbf{a}s + \mathbf{n}, \tag{4.1}$$

where s is the desired signal component arriving from a direction defined by the vector $\mathbf{a}$ and $\mathbf{n}$ is an additive white Gaussian noise (AWGN) vector. The goal of the MVDR beamformer is to design an optimum set of weights $\mathbf{w}$ such that the weighted output of the array

$$y = \mathbf{w}^{\dagger}\mathbf{x} \tag{4.2}$$

maximizes the power contribution of the desired signal component s while minimizing the contribution of signal components arriving from other directions. For the MVDR beamformer, the weights are designed by minimizing the variance of y under the constraint that the input signal is not distorted, i.e., $y = s$ and hence $\mathbf{w}^\dagger \mathbf{a} = 1$. Minimizing the variance of y ensures that the interference contribution is minimized since the desired signal cannot be changed due to the distortionless constraint.

The variance of y is given by

$$E\left\{|y|^2\right\} = \mathbf{w}^\dagger \mathbf{R} \mathbf{w}, \tag{4.3}$$

where $\mathbf{R} = E\left\{\mathbf{x}\mathbf{x}^\dagger\right\}$. Applying the distortionless constraint and performing the Lagrange optimization leads to the optimum weight vectors given by

$$\mathbf{w}^\dagger = \frac{\mathbf{a}^\dagger \mathbf{R}^{-1}}{\mathbf{a}^\dagger \mathbf{R}^{-1} \mathbf{a}}. \tag{4.4}$$

To implement the angular spectrum estimation with the MVDR beamformer, it is assumed that the vehicle speed remains constant and the output of the L element virtual array is defined as

$$\tilde{\mathbf{x}}_{mn}[k] = \left[\begin{array}{cccc} \alpha_{mn}[k] & \alpha_{mn}[k+1] & \ldots & \alpha_{mn}[k+L-1] \end{array} \right]^T, \tag{4.5}$$

where $\alpha_{mn}[k]$ is the k^{th} sample of the discrete time series of complex channel coefficients measured between transmit element n and receive element m. The correlation matrix is estimated by averaging the outputs of N_L virtual arrays such that

$$\tilde{\mathbf{R}} = \frac{1}{N_L} \sum_{l=0}^{N_L - 1} \left[\tilde{\mathbf{x}}_{mn}\left[k + l\frac{L}{2}\right] \left(\tilde{\mathbf{x}}_{mn}\left[k + l\frac{L}{2}\right] \right)^\dagger \right]. \tag{4.6}$$

In estimating the correlation matix (4.6), it is necessary to use enough independent samples to achieve an accurate estimate while balancing the fact that the channel does not stay stationary for an indefinite period of time. For a virtual array length of $L = 8$, observations of the angular response for a number of values of N_L indicate that good results are achieved by averaging over $N_L = 24$ instances of the virtual array output vector $\tilde{\mathbf{x}}_{mn}$.

For each angle θ, measured from the broadside of the array, the power level is estimated using a length-L steering vector

$$\mathbf{v}(\theta) = \left[\begin{array}{ccccc} 1 & e^{j2\pi f_c t_r} e^{j2\pi \frac{d}{\lambda} \sin\theta} & e^{j2\pi 2 f_c t_r} e^{j2\pi \frac{2d}{\lambda} \sin\theta} & \ldots & e^{j2\pi (L-1) f_c t_r} e^{j2\pi \frac{(L-1)d}{\lambda} \sin\theta} \end{array} \right]^T, \tag{4.7}$$

where f_c is the centre frequency and $d = v \cdot t_r$ is the distance between virtual array elements based on the estimated velocity v of mobile and the trigger rate t_r. The array output power is calculated by scanning θ from -90° to 90° and determining the corresponding weight vector

$$\mathbf{w}(\theta) = \frac{\mathbf{v}(\theta)^\dagger \tilde{\mathbf{R}}^{-1}}{\mathbf{v}(\theta)^\dagger \tilde{\mathbf{R}}^{-1} \mathbf{v}(\theta)} \tag{4.8}$$

which is substituted into (4.3) to calculate the angular power at the output of the array such that

$$\hat{A}(\theta) = \mathbf{w}(\theta)^{\dagger}\tilde{\mathbf{R}}\mathbf{w}(\theta). \tag{4.9}$$

As discussed in Chapter 2.2, the measurements presented within this report were made with an eight element receive array in which the dual-polarized elements were distributed along both the driver side and passenger side of the measurement vehicle. Depending on the channel environment and the location of the receiver with respect to the transmitter, each array, from this point on referred to as the driver side array (DSA) and the passenger side array (PSA), will experience completely different realizations of the distribution of multipath energy. To fully understand the nature of each channel environment the analysis of the angular power distribution is performed separately at the DSA and PSA. This will provide a basis for understanding the different propagation characteristics on each measurement route and lay the foundation for the discussions to follow.

4.2 Estimation of the Angular Power Distribution

4.2.1 Laurier Avenue

The angular power pattern measured on each polarization at the DSA and PSA for the Laurier Ave. measurement is shown in Figure 4.1. For the orientations of the arrays on both sides of the vehicle, $\theta = 90$ and $\theta = -90$ indicate angles of arrival toward the front and rear of the vehicle, respectively. It is important to note that the resolution of the MVDR estimator decreases as θ approaches the virtual array axis. As a result, the estimates of the angular power arriving from the front and rear of the mobile will be less accurate than the estimates of the energy arriving from the broadside.

On Laurier Ave. the mobile begins near the intersection with Kent St. This intersection acts as the dominant source for signal energy propagating into the Laurier Ave. urban canyon. In general the characteristics of the angular distribution of power are similar at each array location for the portion of the measurement between 7-17 s. In the region from 7-15 s the mobile is passing through an urban canyon and reflections from buildings often result in a wide angular distribution with groups of multipath arriving from the front and broadside of the array as well as the rear. As the mobile approaches the intersection with Bank St., beginning at 15 s, there are fewer buildings along the street. As a result the number of signal components arriving from the broadside and front of the mobile is decreased and the angular distribution becomes dominated by energy from the rear of the vehicle.

As the mobile passes through the intersection and approaches the buildings on the west side of Bank St., from 17-22 s, the angular distributions at the DSA and PSA begin to differ.

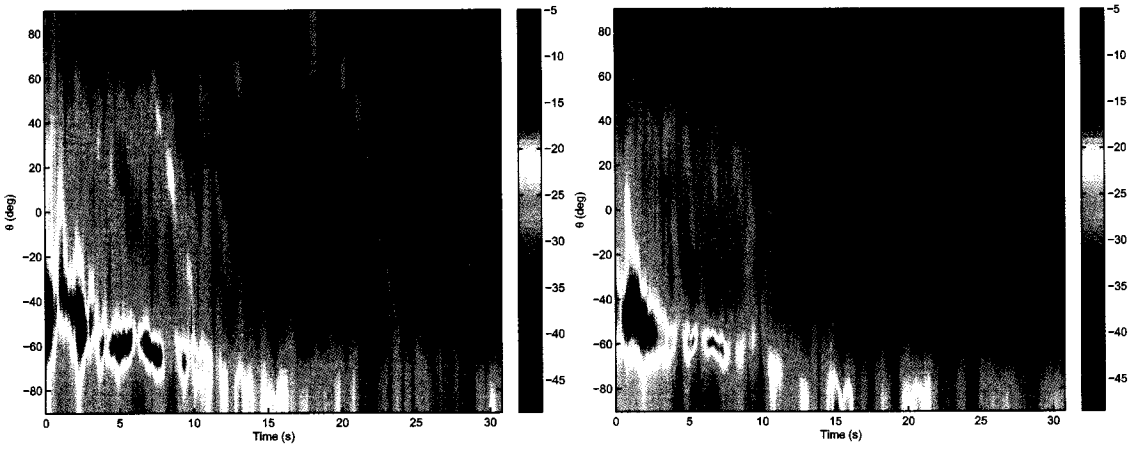

(a) VP-DSA (b) HP-DSA

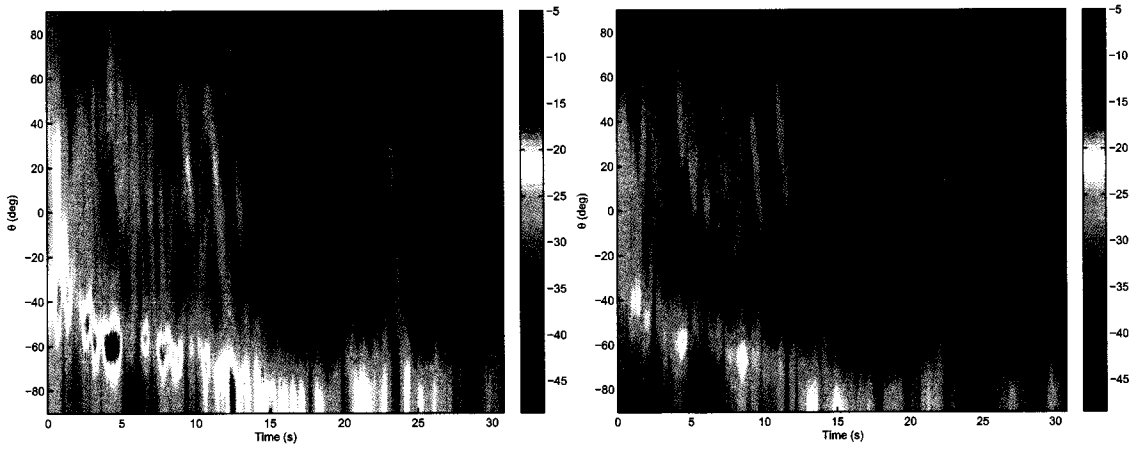

(c) VP-PSA (d) HP-PSA

Figure 4.1: The evolution of the angular power spectrum measured along Laurier Ave. at the vertically and horizontally polarized driver side and passenger side arrays.

At the DSA the number of received multipath groups increases due to strong reflections from these buildings. However, this effect is less noticeable at the PSA where the angular distribution remains dominated by the signal energy from the rear of the mobile. This may be because the buildings on the south-west side of Bank St. are further from the Laurier Ave. and Bank St. intersection than on the north side. As a result the incident angles of the signal components on this side of the street may result in some of the reflected specular components traveling in directions which are not impingent on the PSA.

Once through the intersection, past the 22 s point, the angular distribution at the VP-DSA remains high as groups of multipath are received from both the rear of the mobile and from buildings along the north side of Laurier Ave. At the HP-DSA, some reflected energy

is received through this region, however, as the mobile progresses through to the end of the measurement the strength of the HP components received from the broadside of the mobile is reduced.

4.2.2 Slater Street

The angular power pattern is shown in Figure 4.2 for the channels measured along Slater St. at each of the polarized arrays. The distribution of angular power on Slater St. generally consists of more groups of multipath components spread over a wider angular range than on Laurier Ave., especially on the VP-DSA. Where the Laurier Ave. observations are often dominated by energy arriving from a single direction, the majority of the measurements on Slater St. consists of significant signal components arriving from two or three directions.

On Slater St. the mobile begins near the Kent St. intersection. As on Laurier Ave. this intersection acts a source of signal energy, however, the open area between the buildings south of Slater St. acts as a secondary source, initially toward the front of the mobile. At the 8 s mark the mobile is passing this opening and the energy transitions from the front to the rear of the measurement vehicle. The result is a general reduction in the distribution of angular energy as the mobile progresses through the measurement.

On the Slater St. measurement the energy at the VP-DSA consists of a number of distinct groups of dominant multipath components arriving over the full angular range of the array. On the HP there is a similar angular distribution of energy, however, the strength of the energy from the front of the array is lower. Once the vehicle passes the opening between buildings on the north side of Slater St. at 8 s, the power arriving at the HP-DSA from the broadside disappears almost completely as the reflection surface is lost. At the VP-DSA however, an additional source originating from the front of the array is picked up, resulting in the wide angular distribution of power being maintained.

At the PSA the effect of the secondary signal source is much clearer. On the VP the angular distribution is dominated by the energy received from both the Kent St. intersection and from the building gap. In addition, significant reflected components are received at the broadside from the buildings along Slater St. The result is an overall wide distribution of angular energy. At the HP there is a smaller number of distinct groups of multipath as the energy received from the building gap is more dominant than that from the Kent St. intersection. The lower levels of signal energy on the HP arriving from the rear of the mobile indicates that the signal energy radiating onto Slater St. from Kent St. and Lyon St. may be the result of diffraction around buildings on the street corners, a propagation process which is more favourable to VP signals.

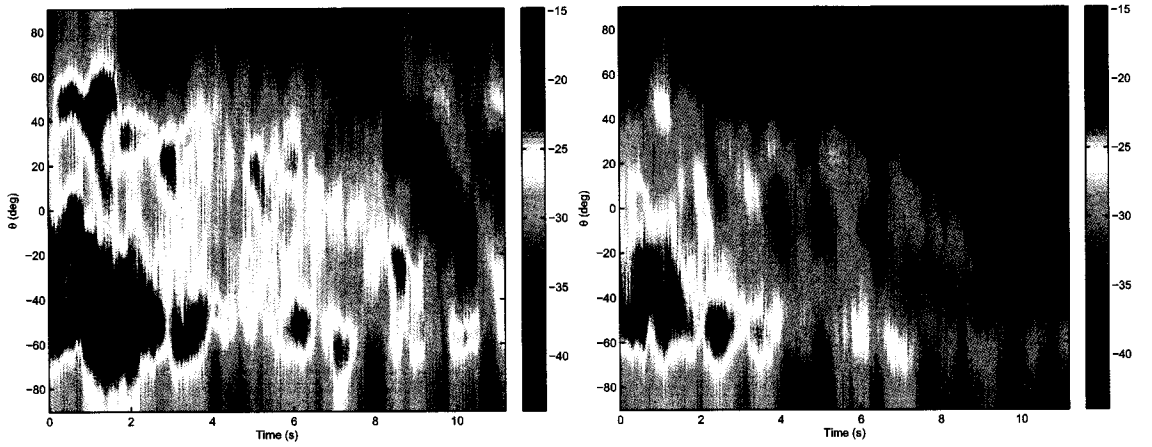

(a) VP-DSA

(b) HP-DSA

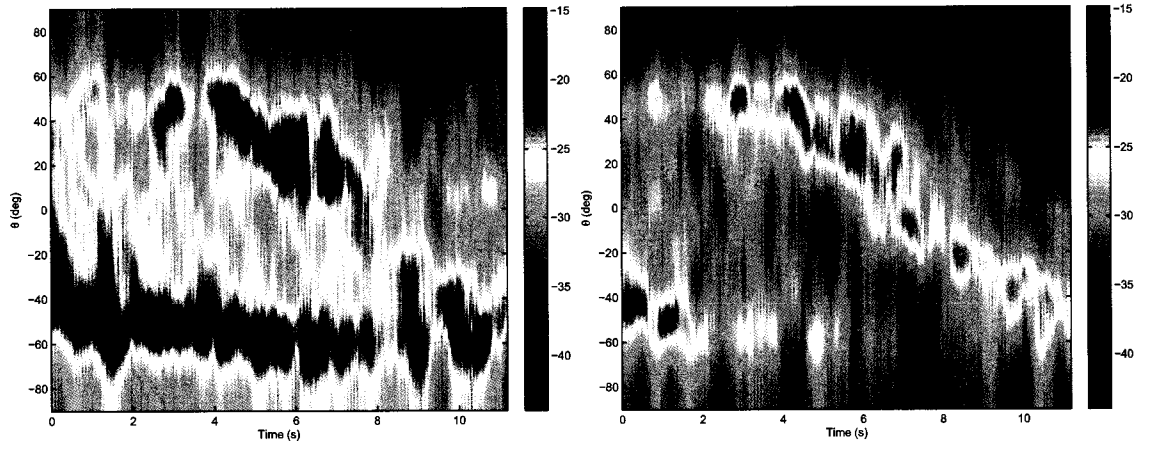

(c) VP-PSA

(d) HP-PSA

Figure 4.2: The evolution of the angular power spectrum measured along Slater St. at the vertically and horizontally polarized driver side and passenger side arrays.

4.2.3 Kent Street

The angular distribution of energy on the Kent St. measurements is plotted in Figure 4.3. For this measurement the mobile is passing through the Gloucester St. and Laurier Ave. intersections in the regions between 8-12 s and 18-22 s respectively. At the DSA the mobile experiences a significant increase in power dominated by a single multipath group within each intersection. This occurs on both the vertical and horizontal polarizations, however, the signal energy is much lower on the HP than on the VP especially in the Gloucester St. intersection.

On the passenger side, the array is shadowed by the mobile so the power received at the PSA results from reflections off buildings along the west side of Kent St. In general this

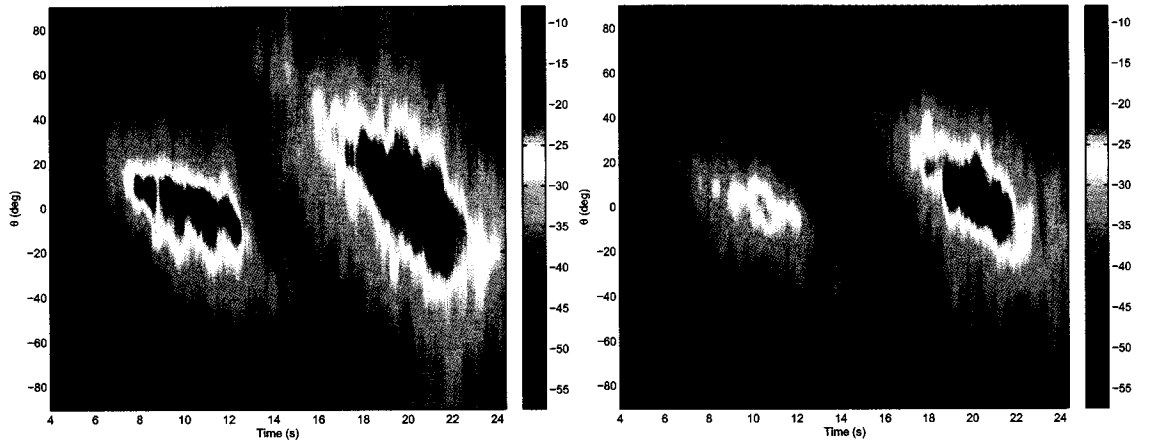

(a) VP-DSA

(b) HP-DSA

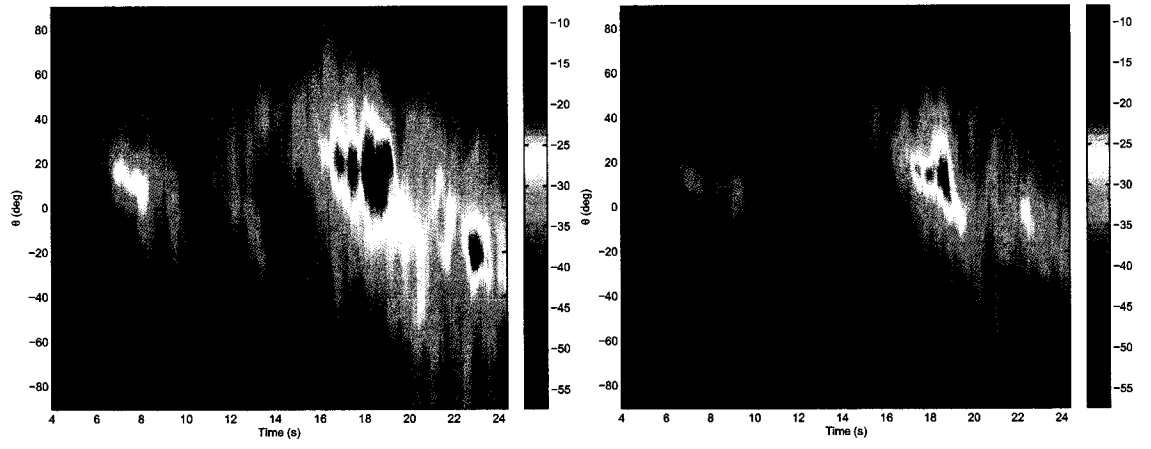

(c) VP-PSA

(d) HP-PSA

Figure 4.3: The evolution of the angular power spectrum measured along Kent St. at the vertically and horizontally polarized driver side and passenger side arrays.

leads to an angular distribution of power which is not as dominated by a single strong group of multipath components as it is on the DSA. However, as the mobile passes through the Laurier Ave. intersection significant reflections off the surrounding buildings still result in the reception of a small number of strong components. As the mobile passes through the centre of the intersection (20-22 s) these reflections disappear only to reappear again when the mobile enters the other side of the intersection. This is caused by the absence of reflectors (buildings) in the middle of the intersection on the passenger side. A similar phenomenon is observed in the Gloucester St. intersection between 10-12 s.

In the middle of the block, the region between 13-16 s, the mobile is in the shadow of the buildings and reflected and diffracted signal energy is received from both the Gloucester

St. and Laurier Ave. intersections, resulting in two groups of multipath components coming from the beginning and rear of the mobile. A similar effect is observed on the PSA however, the angular spread is smaller.

4.2.4 Bank Street

The angular power distribution of the arriving signal components on the Bank St. measurement is shown in Figure 4.4. This measurement route is similar to the Kent St. route in that the mobile also passes through intersections with Gloucester St. and Laurier Ave. at 0-2 s and 10-12 s respectively. At the DSA the angular distribution of power is dominated by a single group of multipath components as the mobile passes through each intersection. At the DSA, the strongest 10 dB of the signal energy is concentrated within an angular spread of less than 40° in both the Gloucester St. and Laurier Ave. intersections. In fact even the strongest 20 dB is limited to a single component distributed across 60°.

At the PSA, much of the signal power is shadowed by the mobile leading up to and inside the Gloucester St. intersection. As a result the angular distribution of power is very evenly distributed across this region as it consists of no dominant groups of multipath. At around the 11 s point, as the mobile is in the centre of the Laurier Ave. intersection, the PSA experiences a similar loss of dominant angular components as was observed on Kent St. in the Laurier Ave. intersection.

Summary

The relationship between the angular distribution of received multipath and the diversity measure is evident in comparing the plots of this chapter with the diverstiy measure plots given in Section 3.2. In channel environments where the received signal is clearly dominated by a single multipath group, such as it is in the intersections on Kent St. and Bank St., there is a distinct drop in the diversity measure. Even on the channels where the energy is spread over a greater range of angles the diversity measure will degrade in the presence of a small number of dominant components, as on Laurier Ave. However, the diversity measure will be higher when the channel consists of energy spread over a large angular range such that the received signal energy is not dominated by strong multipath components. This is exemplified by the diversity measure on Slater St. especially on the HP where the dominant multipath components are generally weaker.

The directionality of the channel also impacts the XPD characteristics discussed in Chapter 3. The relationship between the presence of a dominant component and an increase in the XPD has been observed before [16]. This makes sense intuitively, as a signal becomes

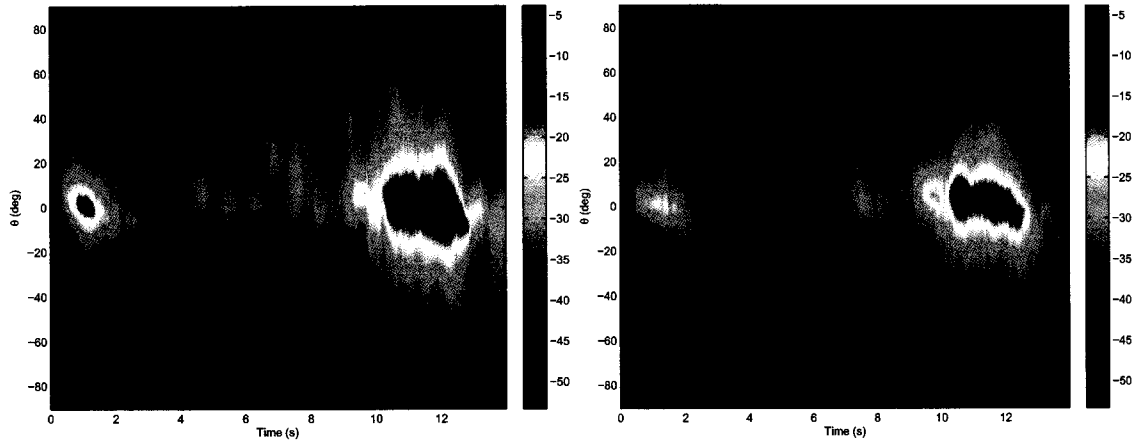

(a) VP-DSA

(b) HP-DSA

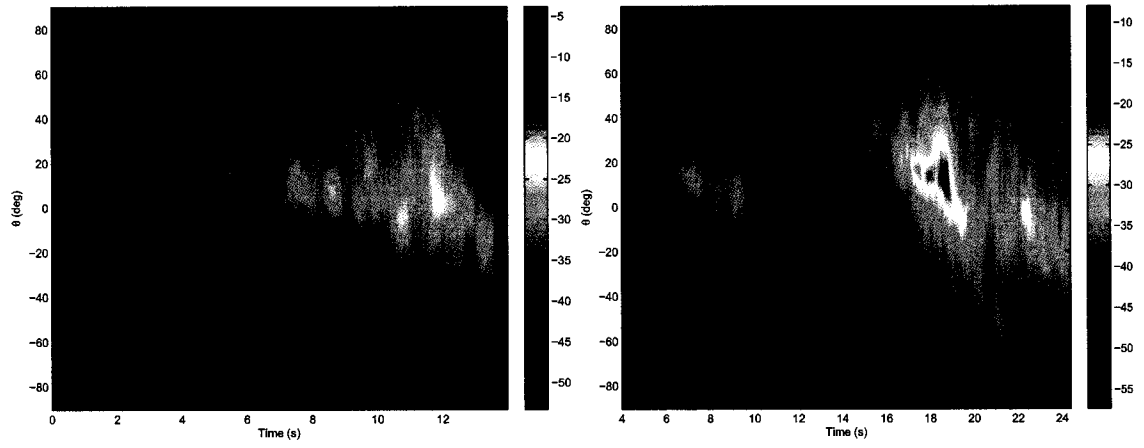

(c) VP-PSA

(d) HP-PSA

Figure 4.4: The evolution of the angular power spectrum measured along Bank St. at the vertically and horizontally polarized driver side and passenger side arrays.

depolarized by interacting with physical objects within the environment, these interactions generally result in the formation of multipath which reduces the channel's directionality. Hence, highly depolarized channels could be expected not to contain strong directional components. However, it has been observed that depolarization can also lead to the formation of specular signals in the orthogonal polarization, as occurs in the intersection regions of Bank St. and Kent St. In these scenarios, large variations in the polarized received power on individual subchannels can develop resulting in the occurrence of both large and small values of XPD.

The angular distributions presented in this chapter demonstrate a clear difference in the propagation characteristics from one side of the mobile to the other. For an engineer

designing a diversity system with multiple antennas located across a vehicle, the impact of such differences in the channel should be considered. In the following chapters the effect of the vehicular array element placement is discussed, starting with an analysis of the subchannel spatial and cross-polar correlations.

Chapter 5

Correlation Coefficients

In MIMO communications, fading correlation among subchannels can significantly impact system performance. The presence of sufficient multipath fading results in independent fading processes at each antenna element thus providing diversity which may be exploited to improve system reliability or increase spectral efficiency. However, when the fading processes are correlated, diversity is lost and system performance degrades.

In a typical MIMO system, diversity is developed by spatially separating the antennas of the transmit and receive arrays. In such a system a minimum spacing of 0.5λ has been found to provide an adequate level of correlation [1] assuming significant multipath exists, however, greater separations are required in environments where less scattering is present.

Spatial correlations are related to the angular distribution of arriving multipath signals. In rich scattering environments signal components arrive at the receiver from all directions and the angles of arrival can be modeled using a uniform distribution from 0° to 360°. This leads to random combining of signal components at each receiver element and uncorrelated MIMO subchannels. This is the fading scenario modeled by the popular i.i.d. Rayleigh channel model and offers ideal conditions for MIMO communications. In environments in which the signal is highly directional, due to either a LOS component or the presence of a strong reflected or diffracted component, spatial correlations will increase. In such a scenario the separation between antenna elements must be increased to preserve the level of performance. In many systems, the mobile handset for example, the requirement for a large physical separation between antennas makes MIMO impractical, especially when the number of antennas is large. However, if the correlations between polarized subchannels are equivalent or lower than those of spatially separated subchannels then it is postulated that polarization diversity may offer an attractive alternative to spatial diversity.

The correlations of polarized channels in indoor environments have been investigated in [31, 48, 49, 32, 33]. In [48], measurements using VP and HP antennas found the VP spatial correlations to be very similar to those of the HP, however, the correlations between the

5.1 Envelope Correlation Coefficients

The envelope correlation coefficients between two complex random variables x and y is defined as

$$\rho(x,y) = \frac{E\{|x| - E\{|x|\}\}E\{|y| - E\{|y|\}\}}{\sqrt{E\{|x|^2 - E\{|x|\}^2\}E\{|y|^2 - E\{|y|\}^2\}}}. \tag{5.1}$$

Throughout this chapter reference is made to correlations calculated at either the DSA or PSA. The DSA correlations are calculated separately using the subchannels from a single transmit array element to the four receiver elements mounted on the driver side of the mobile. Similarly, PSA correlations are calculated using only those subchannels measured at the four elements on the passenger side of the mobile.

Spatial Correlation Coefficients

The spatial correlation coefficients between adjacent vertically polarized array elements at the receiver are defined as

$$\rho_{mn}^{VV} = \rho(\alpha_{mn}^{V}, \alpha_{(m+1)n}^{V}), \tag{5.2}$$

where $n = \{1, 2, \ldots, N\}$ and $m = \{1, 2, 3\}$ on the driver side and $m = \{5, 6, 7\}$ on the passenger side. Similarly, for the horizontally polarized elements

$$\rho_{mn}^{HH} = \rho(\alpha_{mn}^{H}, \alpha_{(m+1)n}^{H}). \tag{5.3}$$

As mentioned in Chapter 2, for the measurements discussed within this report the spatial separation between adjacent array elements was 1λ at both the DSA and the PSA. Further, recall that the receive array elements indexed by $m = \{1, 2, 3, 4\}$ make up the DSA and elements at $m = \{5, 6, 7, 8\}$ make up the PSA.

Cross-Polar Correlation Coefficients

The cross-polar correlation coefficients are defined as the correlation between the subchannels at the colocated vertical and horizontal polarizations of a single receive antenna such that

$$\rho_{mn}^{VH} = \rho(\alpha_{mn}^{V}, \alpha_{mn}^{H}), \tag{5.4}$$

where $m = \{1, 2, \ldots M\}$ and $n = \{1, 2, \ldots, N\}$.

5.2 Measured Spatial and Cross-Polar Correlations

5.2.1 Laurier Avenue

The cdfs of the correlations measured at the DSA and PSA on Laurier Ave. are shown in Figure 5.1. Recall from Section 4.2.1 that the received signal on Laurier Ave. is generally

dominated by a group of multipath components arriving from the rear as well as, at times, strong reflected signal components arriving from the front or broadside. As a result, the Laurier Ave. measurement channels exhibit low to medium levels of diversity.

Even with a small number of dominant signal components the spatial correlations between VP array elements and between HP array elements are low on Laurier Ave. This seems contradictory to the generally lower diversity levels observed on Laurier Ave. However, lower spatial correlations may result from the combination of two strong signal components arriving from different directions. In these bimodal channels the power will be concentrated in a small number of the eigenvalues reducing the diversity measure.

For 90% of the measured subchannels $\rho^{VV} \leq 0.4$ at both the DSA and the PSA and the mean is less than 0.19. At the DSA the HP correlations ρ^{HH} are only slightly lower than those of the VP, whereas they are noticeably lower on the PSA with $\rho^{HH} \leq 0.3$ at the 90^{th} percentile. Less directional power from the rear of the mobile is received at the HP-PSA than on the other array sensors resulting in these lower correlations.

The correlations between the vertically and horizontally polarized subchannels ρ^{VH} are considerably lower than the VP and HP spatial correlations at both arrays. At the 90^{th} percentile the polarized subchannels have a correlation level of less than 0.25 at the DSA and less than 0.2 at the PSA. This can be viewed as a positive indication for polarization diversity as an alternative to spatial diversity.

5.2.2 Slater Street

On the channels measured on Slater St. the power is generally more evenly distributed across the angular range of the receive arrays. This leads to lower correlation levels as indicated by the cdfs shown in Figure 5.2.

The correlation coefficients measured on Slater St. have an almost identical distribution at both the DSA and the PSA with 90% of the VP spatial correlation coefficients measuring less than 0.25. The HP correlation coefficients are slightly less than those of the VP while the polarization correlations ρ^{VH} are further reduced. From a correlation point of view, it is expected that the choice of polarization diversity over spatial diversity would have little impact on overall channel performance on the Slater St. measurement route.

5.2.3 Kent Street

As discussed in Section 4.2.3, power radiates into Kent St. from the Gloucester St. and Laurier Ave. street canyons. As the mobile enters the regions of these intersections the angular distribution of the received multipath components is dominated by the power radiating out of these streets. This leads to higher correlation levels in the intersections which is reflected

in the cdfs in Figure 5.3.

On both the DSA and the PSA the distributions of the spatial correlations, ρ^{VV} and ρ^{HH}, are almost identical to one another. The impact of the intersections is much more noticeable on the DSA than on the PSA where the spatial correlations are considerably higher. On the DSA 90% of the ρ^{VV} and ρ^{HH} are less than 0.6, about double the levels measured on Slater St. However, the mean value for the spatial correlations is still only 0.21 reflecting the low correlations experienced in the non-intersection regions. At the PSA the spatial correlations are more comparable to those measured on Laurier Ave. with 90% measuring less than 0.4 and a mean of approximately 0.1. On the channels measured along Kent St., the PSA is shadowed by the mobile from receiving strong signal components radiating out of Gloucester St. and Laurier Ave. As a result the energy arriving at the PSA undergoes a higher degree of scattering, resulting in lower correlations.

On this measurement route the potential benefits of polarization diversity over spatial diversity are much more dramatic than on Laurier Ave. or Slater St., especially at the DSA where the angular spread is smallest. In Figure 5.3a, 90% of the ρ^{VH} correlations are less than 0.3, while at the PSA $\rho^{VH} \leq 0.25$ at the 90^{th} percentile which is again less than the spatial correlations.

The time series of correlation coefficients measured at the DSA and PSA with respect to transmit element 1 are plotted in Figure 5.4[1]. Each plot contains three subplots in which the VP and HP spatial correlations are shown in the top and middle, respectively, and the cross-polar correlations are shown in the bottom. For the VP and HP spatial correlation plots each line shows the correlation coefficients between the corresponding polarizations on two adjacent antennas. For the cross-polar correlations, each line shows the correlations measured between the VP and HP of a single antenna.

Recall that the mobile is passing through the Gloucester St. intersection in the 8-12 s time frame and through the Laurier Ave. intersection from 18-22 s. At the DSA, the intersection areas result in a significant increase in correlation. This is especially evident on the VP spatial correlations where $\rho^{VV} \approx 0.8$ between 8-9 s and again between 18-19 s. A similar behaviour is exhibited on the HP spatial correlations although the effect is more pronounced in some subchannels than others. For example, in the intersections $\rho^{HH} \geq 0.75$ on the subchannels from transmit element 2, (Figure A.35), whereas $\rho^{HH} \leq 0.55$ on the subchannels from transmit element 1.

The impact that the propagation characteristics in the intersections have on the correlations at the PSA is reduced due to shadowing from the mobile. When the mobile is in the centre of the Laurier Ave. intersection (19-22 s) the ρ^{VV} are consistently low. Leading up to

[1]The time series of correlation coefficients measured on Laurier Ave., Slater St., Kent St. and Bank St. from all transmit elements are provided in Appendix A.

the intersection (16-19 s), ρ^{VV} tends to increase as the PSA receives a strong reflected signal component from the buildings along the east side of Kent St. However, as the mobile enters the intersection the vehicle begins to shadow the PSA from the highly directional energy radiating out of the Laurier Ave. canyon. This is exacerbated by the lack of buildings (i.e., the open street) along the east side of Kent St. As a result the energy received at the PSA is scattered from the street corners and the correlations are reduced. A similar behaviour is observed on the HP spatial correlations where the highest correlation levels are observed immediately before and after the mobile enters the intersections.

At both the DSA and PSA the polarization correlations remain largely unaffected by the directional nature of the signal energy at the intersections. For most of the measurement $\rho^{VH} \leq 0.5$ and the variations do not appear to be highly correlated to either the directional nature of the channel or the location of the mobile. This is generally the case for the subchannels measured from other transmit elements as well, however the subchannels from transmit element 2 and 5 in Figure A.35 and Figure A.41, respectively, do exhibit higher polarization correlations in the intersections especially at the DSA.

5.2.4 Bank Street

As on Kent St., the correlations measured on Bank St. are dominated by the strong directional component in the regions of the intersections. The cdfs of the correlations measured at the DSA and PSA are plotted in Figure 5.5. At the DSA the spatial correlations are higher than those measured on the other streets with $\rho^{VV} \leq 0.7$ and $\rho^{HH} \leq 0.75$ at the 90^{th} percentile. At the PSA the correlations are much lower with 90% less than 0.3 on the VP and less than 0.25 on the HP. At the DSA the cross-polar correlations are higher than those measured on other streets but still lower than the spatial correlations with $\rho^{VH} \leq 0.4$ for 90% of the measured subchannels.

The warped nature of the cdf curves for the DSA spatial correlations indicates the tendencies of the correlations to be either high or low with the middle of the range values being less likely. This is illustrated in the time series plots of ρ measured with respect to transmit element 2 in Figure 5.6.

Of all the measurements analyzed, the highest correlations were observed in the Gloucester St. and Laurier Ave. intersections with Bank St. At the DSA, when the mobile enters the intersection, from 0-2 s and 10-13 s, the spatial correlations increase abruptly as opposed to the gradual increase in the Kent St. intersections. In these intersections the correlations are higher than in the corresponding Kent St. intersections with $\rho^{VV} \approx 1$ at 1 s and $\rho^{HH} \approx 1$ at 10.5 s.

Given that Bank St. is further away from the transmitter than Kent St., it could be expected that, in traveling the extra distance, the signal undergoes a greater degree of reflection

and scattering resulting in a greater number of multipath components at the receiver and correspondingly a lower level of correlation. However, as the signal propagates from Lyon St. to Bank St., the powers of these scattered and reflected multipath components are significantly reduced. On the other hand, the Gloucester St. and Laurier Ave. urban canyons act similar to a wave guide, directing energy along each street. As a result, in the intersections with Bank St., the received signal is completely dominated by a single strong, directional component. Hence, the correlations are very high. This effect also impacts the cross-polar correlations, e.g., $\rho^{VH} \approx 0.9$ just after 10 s, however, such high correlations occur less frequently among the cross-polar channels.

At the PSA the intersections have significantly less impact on the correlations, especially at Gloucester St. where no effect at all is noticeable. This is true of all the subchannel correlations measured at the PSA from each transmit element as shown by the figures in Appendix A.4. At the Laurier Ave. intersection, as there was on the Kent St. measurement, the PSA often experiences a rise in correlation just prior to entering the intersection followed by a drop in correlation within the intersection and another rise as the mobile exits the intersection. However this behaviour is not as consistent with respect to the different transmit elements. For example HP spatial correlations ρ^{HH} from transmitter 3 in Figure A.54 show very little effect within the Laurier Ave. intersection while the ρ^{VV} correlations from transmit element 5 range from 0 to 0.5 within this region.

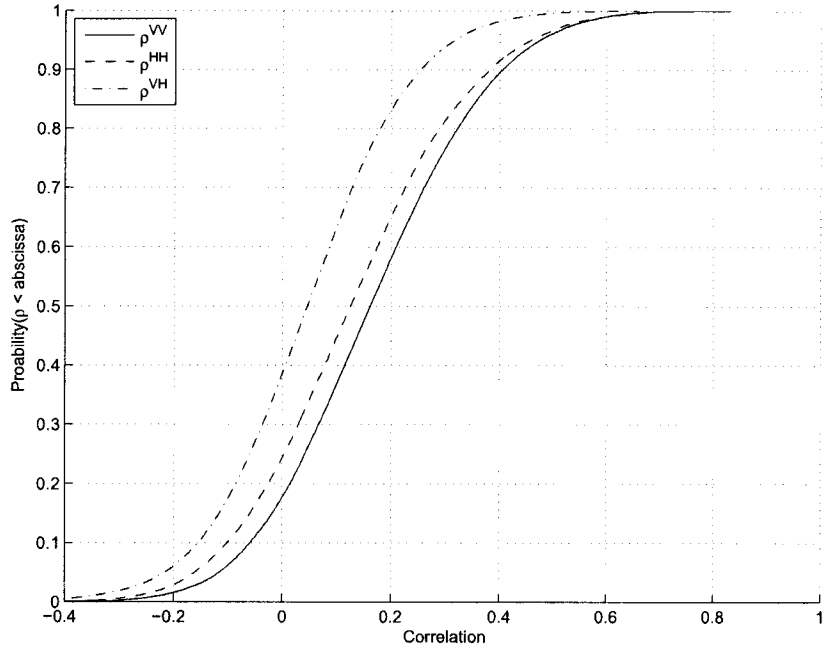

(a) DSA

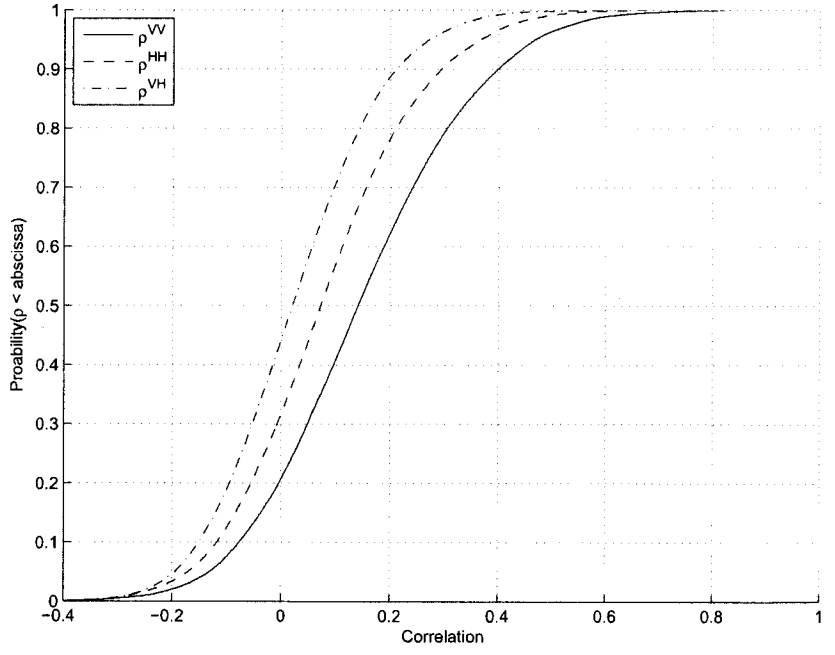

(b) PSA

Figure 5.1: cdfs of DSA and PSA spatial and cross-polar correlation coefficients measured on Laurier Ave.

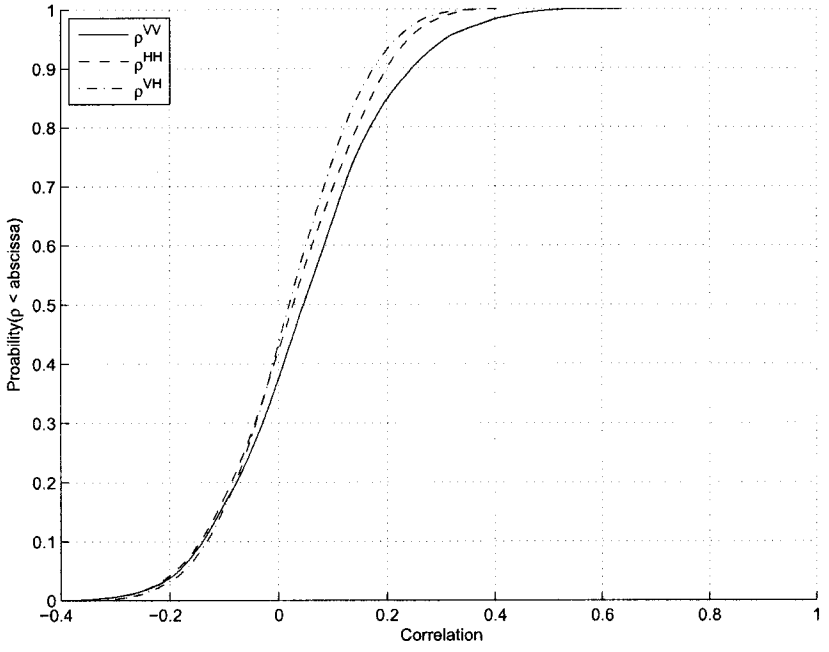

(a) DSA

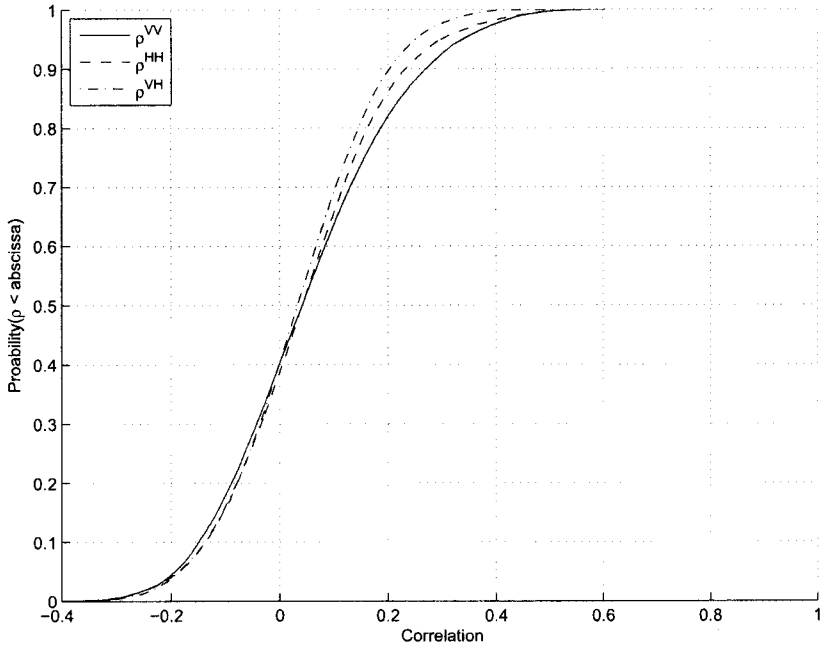

(b) PSA

Figure 5.2: cdfs of DSA and PSA spatial and cross-polar correlation coefficients measured on Slater St.

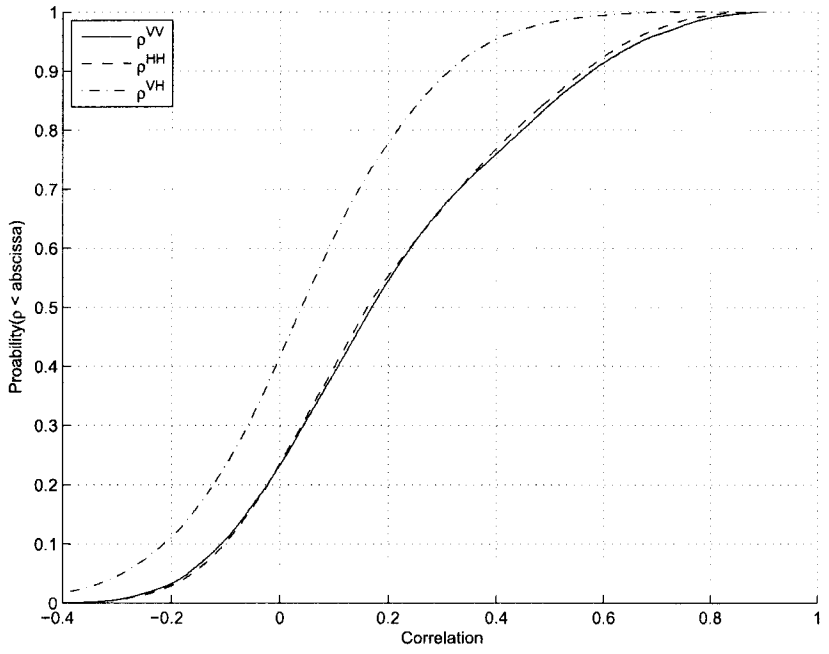

(a) DSA

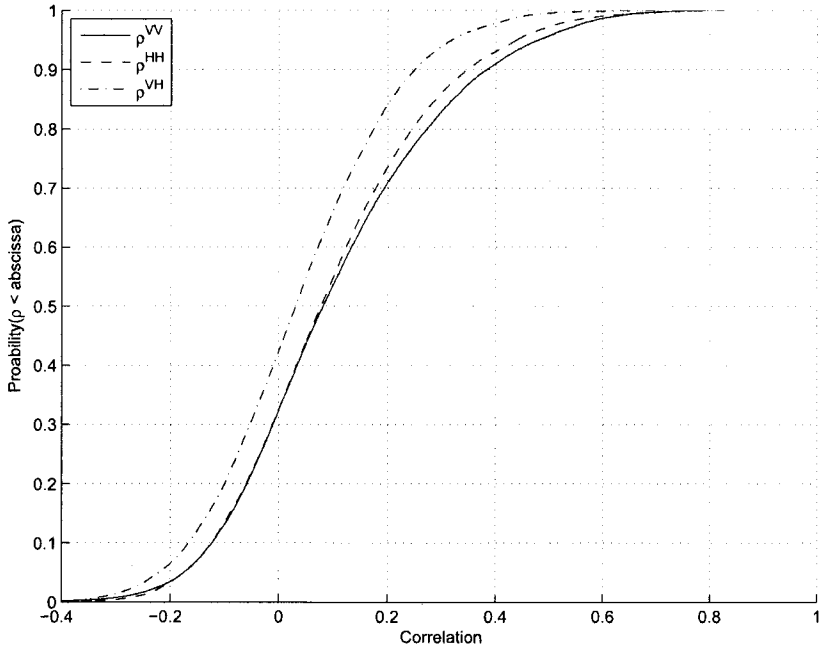

(b) PSA

Figure 5.3: cdfs of DSA and PSA spatial and cross-polar correlation coefficients measured on Kent St.

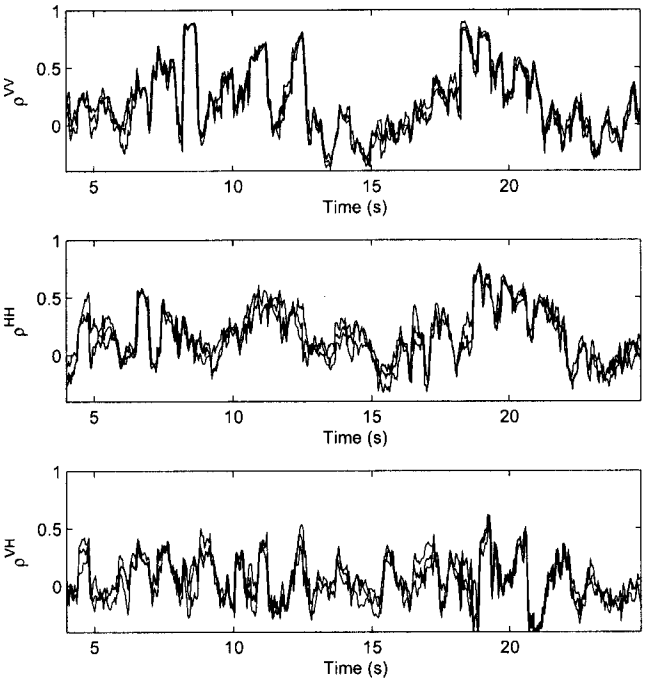

(a) DSA

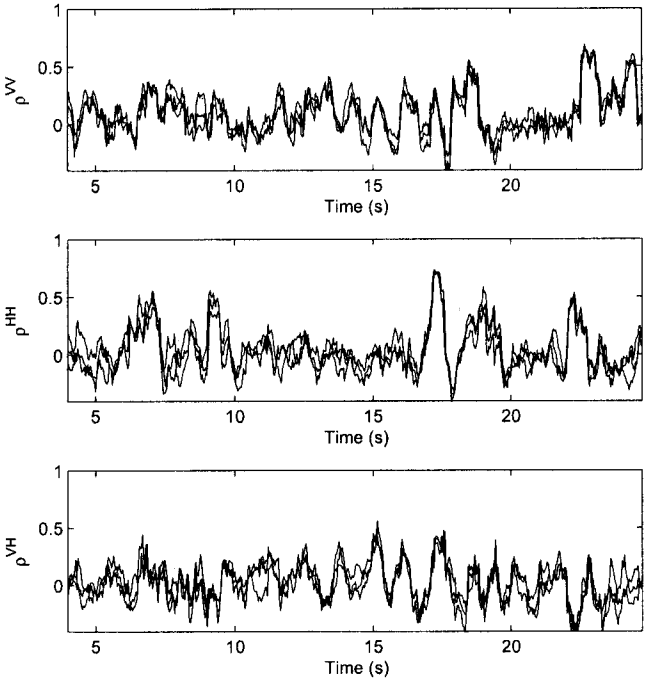

(b) PSA

Figure 5.4: Time series of correlation coefficients measured on Kent St. The top and middle plots show the spatial correlations of the VP and HP channels, respectively. The bottom plots show the polar correlation coefficients across the VP and HP subchannels. In each plot, the lines show the correlations between a different pair of subchannels measured at the receiver with respect to transmit element 1. The correlation plots with respect to all transmit elements are provided in Appendix A.

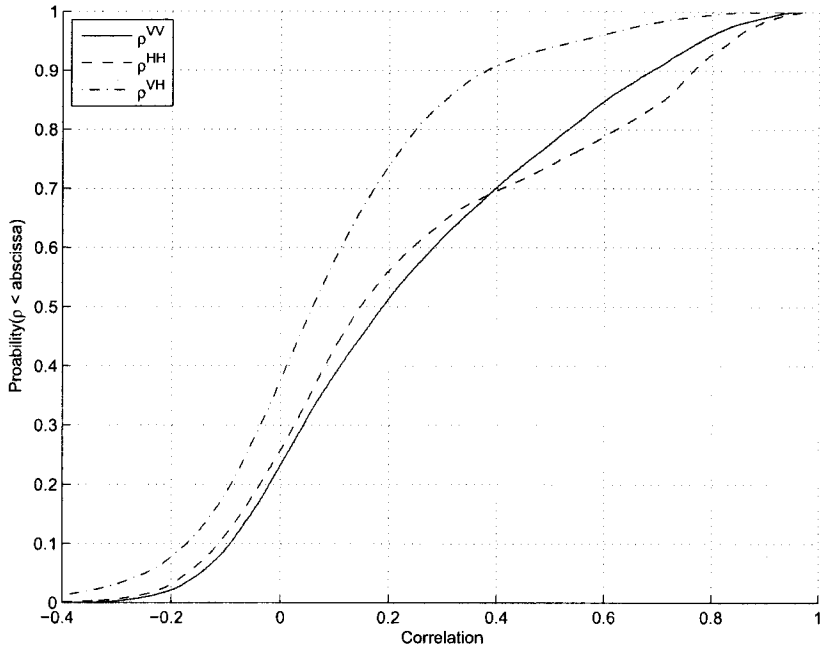

(a) DSA

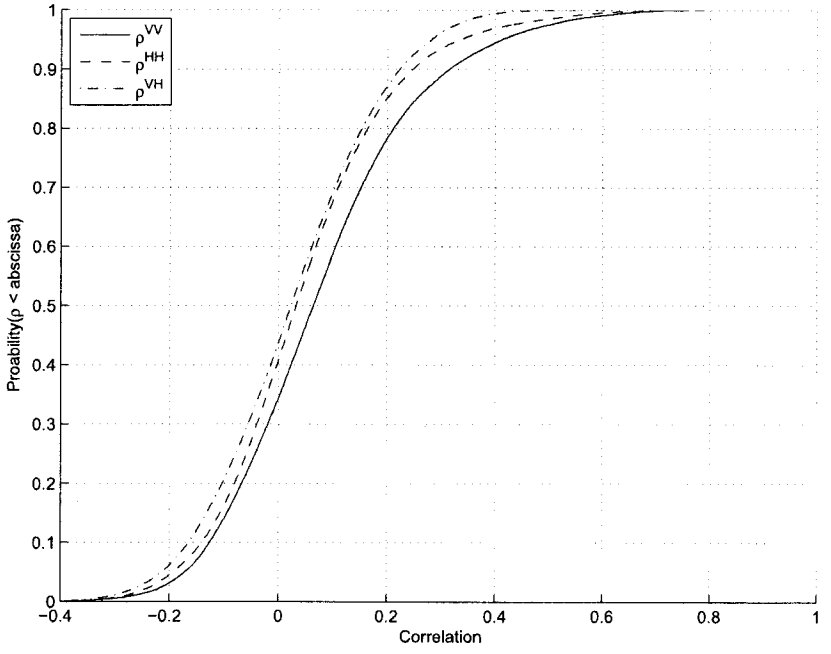

(b) PSA

Figure 5.5: cdfs of DSA and PSA spatial and cross-polar correlation coefficients measured on Bank St.

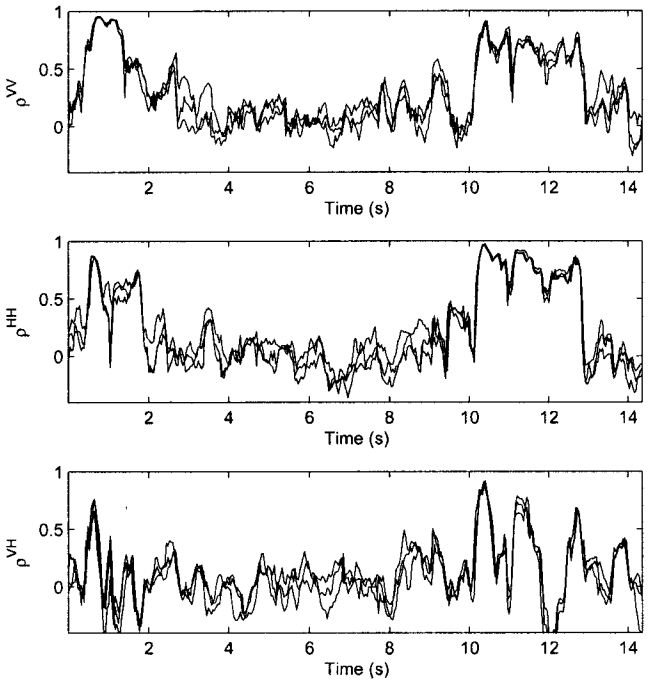

(a) DSA

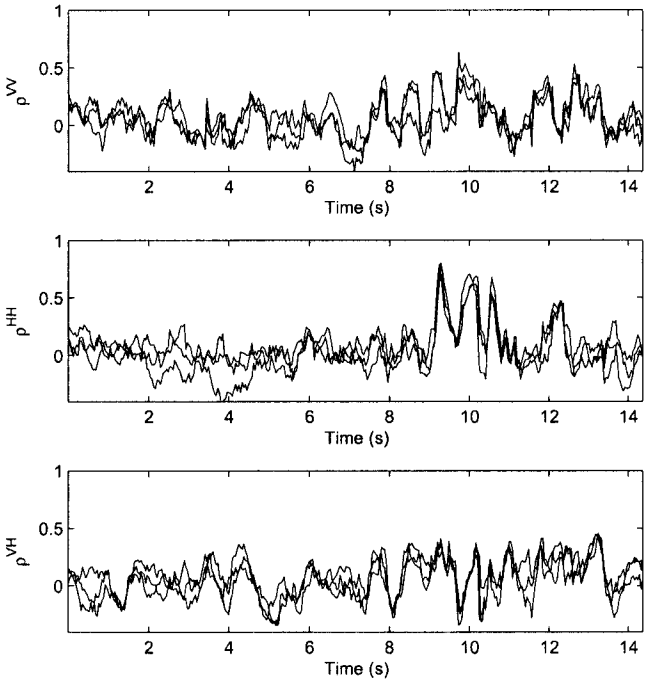

(b) PSA

Figure 5.6: Time series of correlation coefficients measured on Bank St. The top and middle plots show the spatial correlations of the VP and HP channels respectively. The bottom plots show the polar correlation coefficients across the VP and HP subchannels. In each plot, the three lines show the correlations between a different pair of subchannels measured at the receiver with respect to the same transmit element. The correlation plots with respect to all transmit elements are provided in Figure A.

Chapter 6

Driver Side vs Passenger Side Polarized Channel Characteristics

In Chapter 3, the polarized channel characteristics of an 8×8 MIMO system were analyzed based on the generalized scattering environment in the area of the mobile. In this chapter, the localized effect the mobile has on the polarized received signal arriving at antenna elements placed on both sides of the vehicle is analyzed.

6.1 Polarized Channel Powers

6.1.1 Laurier Avenue

The average power received on the vertical and horizontal polarizations at the DSA is defined by averaging the subchannel powers from the N transmitter elements to the $M_d = 4$ receiver elements mounted along the driver side of the mobile such that

$$P_d^V = E\left\{tr\{\mathbf{H}_d^V(\mathbf{H}_d^V)^\dagger\}\right\}, \text{ and } P_d^H = E\left\{tr\{\mathbf{H}_d^H(\mathbf{H}_d^H)^\dagger\}\right\}. \tag{6.1}$$

Similarly the mean power at each polarization of the PSA is defined using the N subchannels at each of the $M_p = 4$ array elements located on the passenger side of the mobile such that

$$P_p^V = E\left\{tr\{\mathbf{H}_d^V(\mathbf{H}_p^V)^\dagger\}\right\}, \text{ and } P_p^H = E\left\{tr\{\mathbf{H}_p^H(\mathbf{H}_p^H)^\dagger\}\right\}. \tag{6.2}$$

The mean power levels measured on Laurier Ave. are shown in Figure 6.1. The upper portion of the figure shows P_d^V and P_d^H and the lower shows P_p^V and P_p^H. In general, the PSA tends to be closer to the buildings lining the streets while the DSA is positioned in the centre of the street. On the Laurier Ave. measurement the mobile is moving west so the broadside of the PSA faces south while the DSA faces north. As mentioned in Section 4.2.1 most of the power at the receiver is originating from the rear of the mobile in the intersection

of Laurier Ave. and Kent St. but a power difference of up to 10 dB between the DSA and PSA is still present.

To help illustrate the difference in received power on one side of the van versus the other a new metric is defined as the array power imbalance (API). This metric is the ratio of the power received on a given polarization at the driver side array versus that received at the PSA. Thus the API for the vertically polarized channels is given as

$$API^V = E\left\{\frac{tr\{\mathbf{H}_d^V(\mathbf{H}_d^V)^\dagger\}}{tr\{\mathbf{H}_p^V(\mathbf{H}_p^V)^\dagger\}}\right\} \tag{6.3}$$

and similarly for the HP channels the API is

$$API^H = E\left\{\frac{tr\{\mathbf{H}_d^H(\mathbf{H}_d^H)^\dagger\}}{tr\{\mathbf{H}_p^H(\mathbf{H}_p^H)^\dagger\}}\right\}. \tag{6.4}$$

Channels in which more power is received on the DSA than on the PSA will have a large API^Vor API^H. However, when the opposite is true the API will be very small. Diversity will be maximized when equal signal levels are received at each array resulting in a unity API. For a MIMO system with elements of the antenna array distributed across both sides of the mobile a very high or low API will reduce the diversity levels achievable.

The $API^V$and API^Hmeasured on Laurier Ave. are shown in Figure 6.2. For most of the measurement, the power received on the DSA is greater than that on the PSA by as much as 10 dB on the VP. The consistently positive log values for the API^V and API^H indicate that the propagation environment favours the DSA. One of the reasons for this is that the PSA is much closer to the buildings than the DSA. In electromagnetic propagation, obstacles in the environment act as signal sources for multipath components due to reflection and diffraction. Because the street is open on the driver side of the vehicle the DSA can effectively see more sources than the PSA which looks directly out onto the side of a building. For example, from about 7-11 s the mobile is passing by an opening between buildings on the north side of Laurier Ave. Figure 4.1a indicates a strong multipath component arriving at the DSA from the front of the vehicle at 7 s and transitioning to the rear of the vehicle at 10 s. During this period the $API^V$is 2-5 dB. However, after the vehicle passes this open area it moves between two buildings (11-14 s) and there is an increase in energy at the PSA while the decline in power of the DSA continues. Here, the building on the north side of Laurier Ave. shadows the DSA from the energy radiating out of the open area, while the building on the south side reflects it back at the PSA. In this region the API^Vdrops to near 0 dB.

The XPD on the DSA and PSA are shown in Figure 6.3. On the DSA, the similarity of the received powers on each polarization leads to a lower $\hat{\mu}_{XPD}$, however, on a per subchannel basis there is significant variation of the XPD with values frequently -5 dB or less. On the

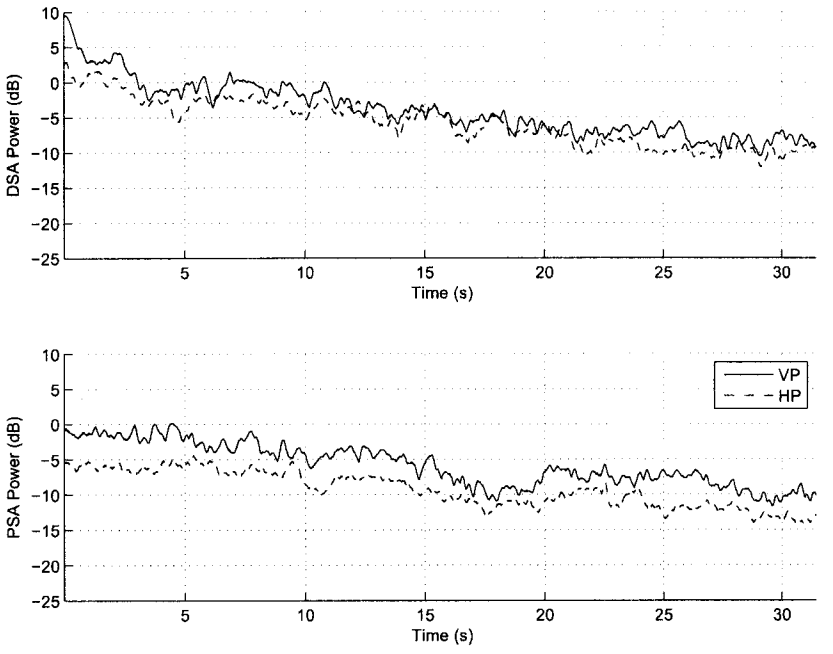

Figure 6.1: Average received power on the VP and HP channels measured at the DSA (top) and PSA (bottom) on Laurier Ave.

PSA the consistent difference in the VP and HP signal powers for the first 15 s results in a higher $\hat{\mu}_{XPD}$ and reduced variation across the subchannels. However, after the 15 s mark, as the mobile enters the open area prior to the Bank St. intersection the variation in the XPD across the array increases. As discussed in Section 4.2.1, the received power is highly directional in this portion of the channel due to the loss of reflective sources on the sides of Laurier Ave.

Comparing Figure 6.3 to Figure 3.3 illustrates how the high variance of the XPD on the complete $N \times M$ channel was largely a product of channels located on the DSA. The directional angular spectrum on these channels causes some subchannels to develop Ricean fading characteristics in which the power in the dominant component is larger on one polarization than on the other. Large differences result in an increase or decrease in the subchannel's XPD, depending on which polarization receives the component with the higher power. For the Laurier Ave. measurement, the DSA subchannels often exhibit Ricean fading in which the dominant component on the HP is greater than that of the VP. This is likely due, in part, to the fact that the open street surface at the driver side of the mobile is favourable for the propagation of HP signals. As a result, the XPD of these subchannels can be less than $\hat{\mu}_{XPD}$ by more than 10 dB.

The propagation of HP signals is not as favourable on the passenger side of the mobile

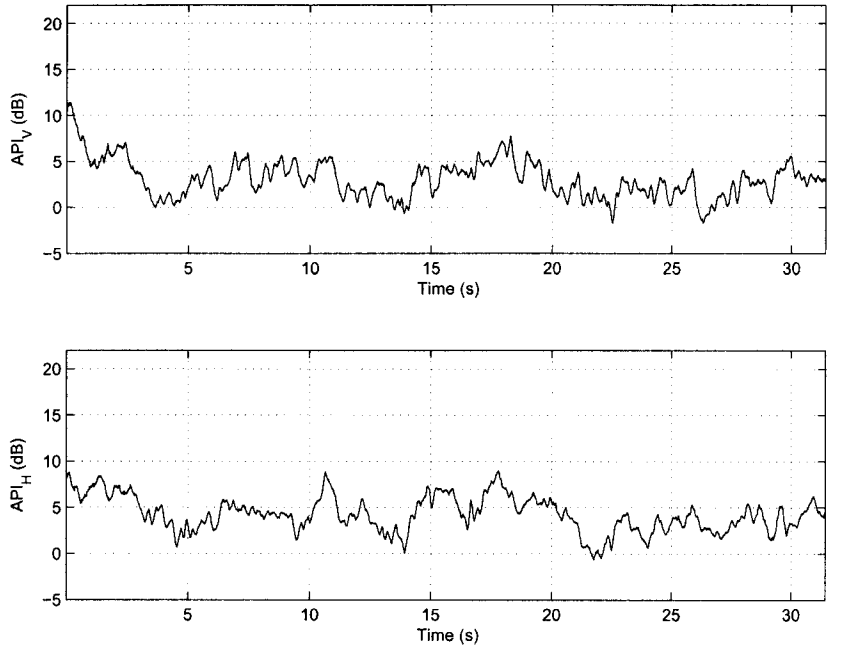

Figure 6.2: Array power imbalance measured on Laurier Ave. API^V(top) API^H(bottom).

due to the closer proximity of the PSA to the buildings along the street. As a result, the XPD of the subchannels at the PSA tends to be higher than at the DSA. However, in the times between 15-25 s the variations in the XPD of PSA channels increases. In this portion of the channel the mobile has entered the intersection with Kent St. and energy at both the DSA and PSA is dominated by signals arriving from the rear of the mobile. Here, the absence of the buildings along the streets result in a lack of scatterers at the front of the mobile reducing the angular range over which multipath components are received and improving the propagation conditions for HP signals at the PSA. As a result, the polarized subchannels in this environment periodically exhibit strong Ricean components which result in high (15-16 s) and low (16-17 s) XPD^V values.

6.1.2 Slater Street

On the Slater St. measurement the power received at both the DSA and PSA, shown in Figure 6.4, is consistently lower on the HP, however, the power decays at a greater rate on the DSA than on the PSA. Recall from Section 4.2.4 that on Slater St. two portions of the street act as sources of signal energy. The main source is the intersection of Kent St. and Slater St., the secondary source is the gap between the buildings along the south side of the street between Kent St. and Bank St. The slower power decay on the PSA is due to diminishing power from the intersection being replaced by increasing power from the

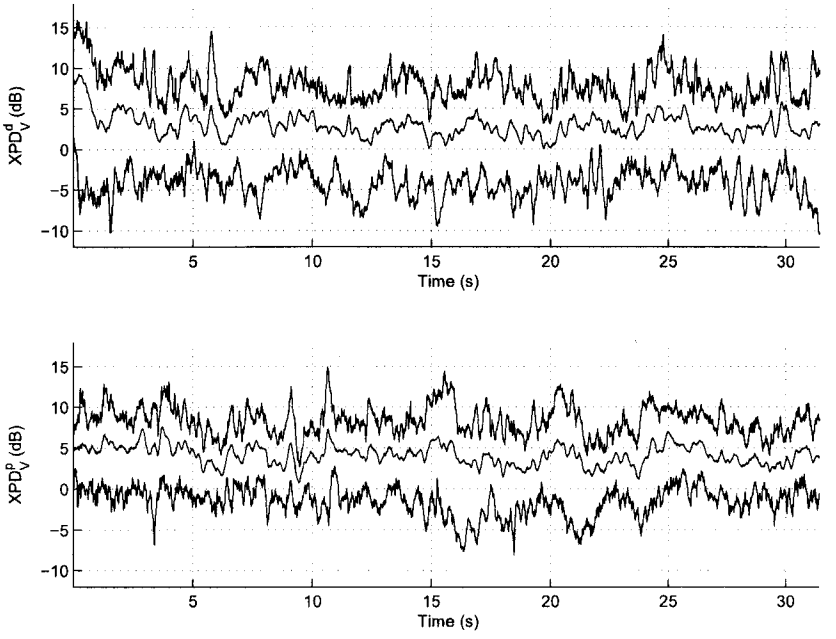

Figure 6.3: XPD^V_{max}, $\hat{\mu}_{XPD}$, XPD^V_{min} measured at the DSA (top) and PSA (bottom) on Laurier Ave.

building gap.

The secondary signal source on Slater St. results in a decreasing API (Figure 6.5) for both polarizations. In the initial 3 s of the measurement the power at the mobile is dominated by energy at the DSA especially on the HP. However, as the mobile nears the building gap at 4 s, the power radiating from this secondary source becomes much stronger at the PSA. As the mobile passes through this region the DSA is shadowed by the mobile resulting in an API less than 0 dB. For the remainder of the measurement the API stays lower on the HP than on the VP. This indicates that the HP power decays at a greater rate on the DSA than the VP power does. For the DSA to receive HP energy radiating out of the building gap, it must be reflected by a horizontal surface. However the vertical walls of the street canyon result in a depolarization of the reflected energy back to the VP.

The characteristics of the XPD on Slater St., shown in Figure 6.6, are similar on both the DSA and PSA with an $\hat{\mu}_{XPD} \approx 5$ dB for the whole measurement. On the DSA there is a slight oscillation of the XPD due to initially increasing and then decreasing HP power radiating from the secondary source, however, the variance of the XPD on each side is consistent for the whole measurement.

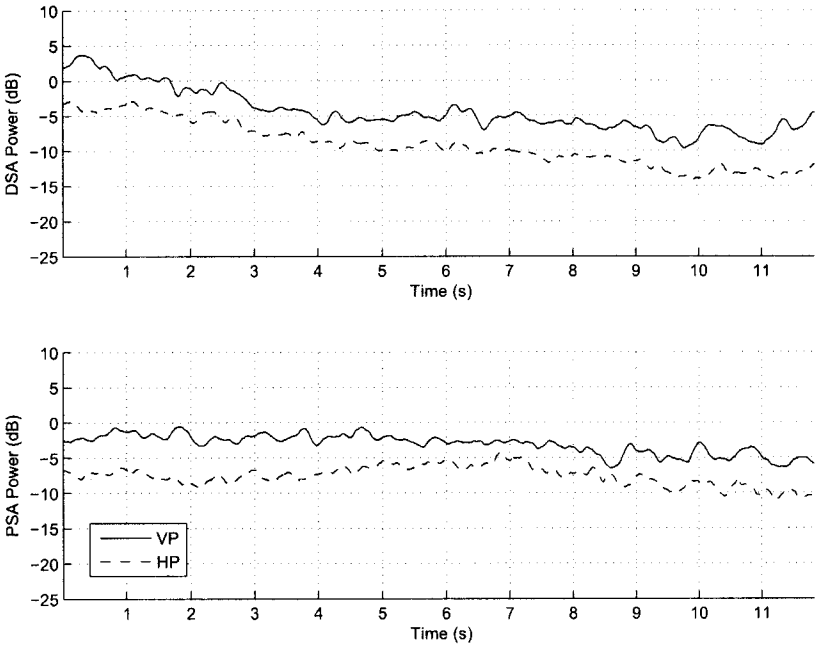

Figure 6.4: Average received power on the VP and HP channels measured at the DSA (top) and PSA (bottom) on Slater St.

6.1.3 Kent Street

Figure 6.7 shows the average power measured on the vertical and horizontal polarizations at the DSA and PSA along the Kent St. route. Immediately clear is the increase in received power when the mobile is passing through the Gloucester St. (8-12 s) and Laurier Ave. (18-22 s) intersections. On both sides of the mobile the power at the HP is about 5 dB less than that of the VP. At the DSA, the powers on both polarizations are greatest when the mobile is in the centre of the intersections, however, on the PSA the power at each polarization is greatest just prior to the intersection. Since the PSA is shadowed from the transmitter by the mobile it receives most of its energy via reflections from the buildings on the west side of Kent St. When the mobile is in the middle of the intersections, at 20 s for example, the absence of buildings result in a drop in received power.

The difference in the power behaviour on the DSA and PSA is clear from the API plotted in Figure 6.8. In the Gloucester St. intersection, the $API^V$and $API^H$are 20 dB and 18 dB respectively, and in the Laurier Ave. intersection both reach 15 dB. These represent significant differences in power levels between the two sides of the mobile. These types of channels will represent a significant diversity disadvantage for a MIMO system using arrays with elements similarly distributed. Accounting for such imbalances in power will be important consideration in designing systems for which the targeted performance is based

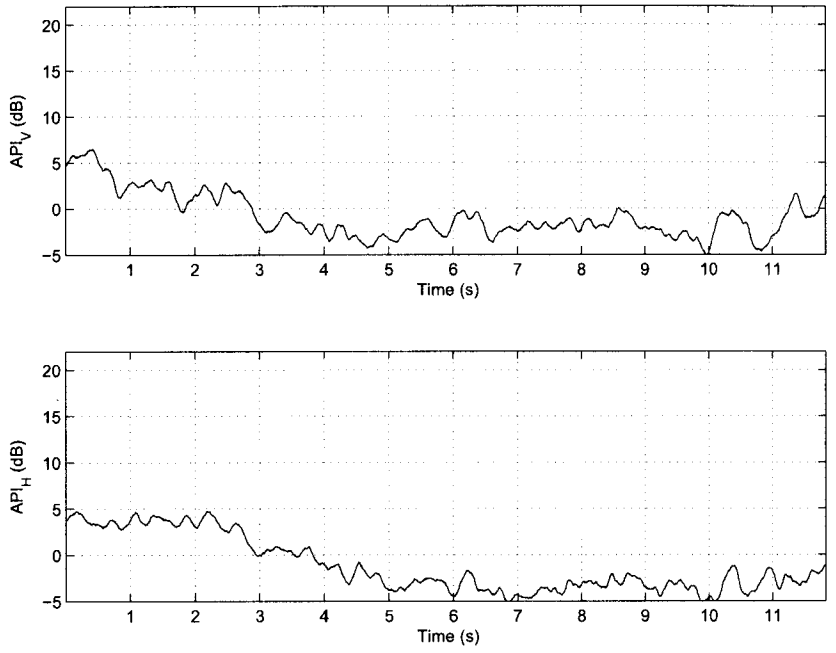

Figure 6.5: Array power imbalance measured on Slater St. API^V(top) API^H(bottom).

on a more even distribution of power. In these scenarios the use of selection diversity, where the receive branches with low signal levels are not used, may be a beneficial system option.

In the non-intersection regions, 4-7 s, 13-18 s and 23-25 s, both the $API^V$and $API^H$are near zero indicating that, on these portions of the channel, energy is being reflected and scattered equally to both sides of the mobile, although the difference between the VP and HP remains the same.

The XPD measured along Kent St. is shown in Figure 6.9. In the non-intersection regions of the route the XPD is about 5 dB on both sides of the mobile, however, near the intersections, both the mean and variance of the XPD increases. This is especially noticeable on the DSA where instances of the XPD_d^V are as much as 16 dB and the $\hat{\mu}_{XPD}$ reaches 10 dB. At the PSA, the $\hat{\mu}_{XPD}$ is less than that of the DSA with $\hat{\mu}_{XPD} \leq 8$ dB.

6.1.4 Bank Street

The Bank St. measurement is very similar to the Kent St. measurement in that the mobile again passes through intersections with Gloucester St. (0-2 s) and Laurier Ave. (11-13 s). The average powers measured on Bank St. are shown in Figure 6.10. For most of the measurement the power on the VP tends to be about 3 dB greater than that of the HP, however, within the Laurier Ave. intersection, at 10 s and 11 s, the powers at each polarization are almost equal. During this small section of the measurement the overall channels have become almost

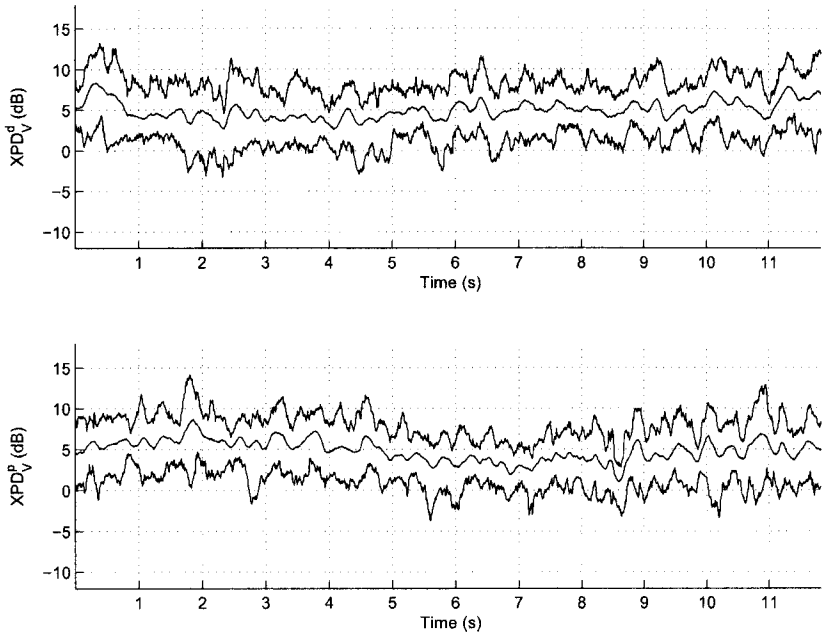

Figure 6.6: XPD^V_{max}, $\hat{\mu}_{XPD}$, XPD^V_{min} measured at the DSA (top) and PSA (bottom) on Slater St.

completely depolarized. At the DSA, increased power in the intersections is clearly present on both polarizations, however, the PSA is almost completely shadowed by the vehicle.

As on Kent St., the API (shown in Figure 6.11) is considerable in the intersections on Bank St. reaching more than 20 dB and 15 dB in the Gloucester St. and Laurier Ave. intersections, respectively. This is an indication of the high strength of the directional components propagating along Gloucester St. and Laurier Ave. compared to the scattered components coming from other directions. In these regions, the waveguide effect of Gloucester St. and Laurier Ave. have focused the energy to a single group of components propagating along each street while the scattered energy has become very weak. As a result the DSA receives significant power from which the PSA is shadowed.

The impact of the propagation characteristics on the Bank St. intersections is clearer on the XPD measured on Bank St. (Figure 6.12) than on Kent St. On the DSA the XPD increases to 10 dB in the Gloucester St. intersection, and reaches 7 dB in the Laurier Ave. intersection. In these intersections the variance in the XPD is considerable, ranging from 16 dB to -10 dB. The XPD on the PSA is somewhat different. Although variations in the XPD from -5 dB to 13 dB occur within the Laurier Ave. intersection, the energy at the PSA is more scattered and the variance of the XPD is reduced.

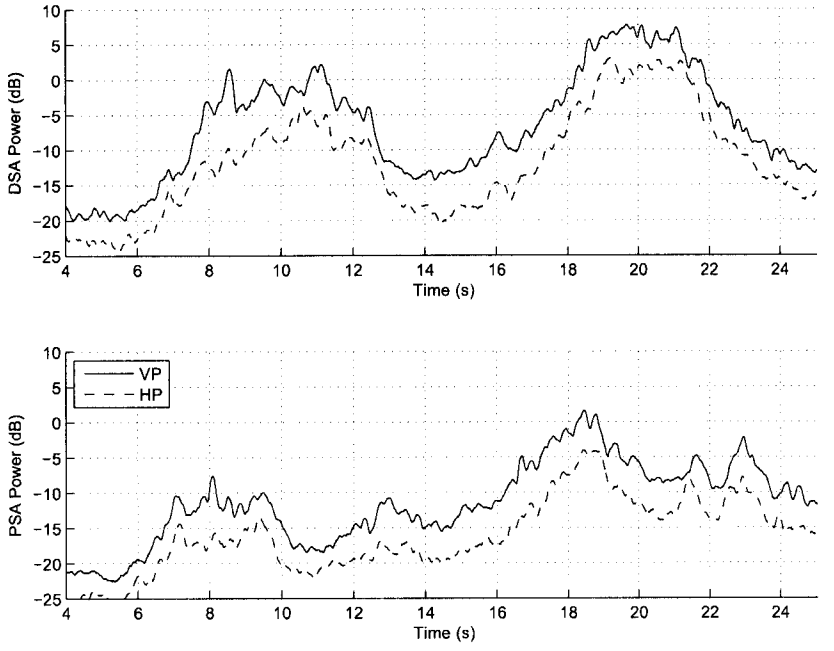

Figure 6.7: Average received power on the VP and HP channels measured at the DSA (top) and PSA (bottom) on Kent St.

6.2 Polarized Channel Diversity Measures

The diversity measure (3.7) of the polarized channels captured along Laurier Ave. are given in Figure 6.13. On each side of the mobile the diversity behaviour differs somewhat. On the DSA the diversity tends to be low for the whole measurement, especially in the urban canyon portion between Kent St. and Bank St. On the PSA, the diversity on the VP, though higher than that on the DSA, is lower than the HP for the first 15 s of the measurements. Once inside the Bank St. intersection the narrow angular distribution of the received energy (see Figure 4.1c and Figure 4.1d) results low diversity levels between 15-20 s. As the mobile moves into the street canyon on the west side of the intersection the diversity rises again as scattering from the surrounding buildings increases.

The diversity on Slater St., shown in Figure 6.14, is greater than that of Laurier Ave. on both polarizations and at both arrays. This is due to the increased angular spread of the received energy on Slater St. resulting from multipath components radiating out of the Slater St. building gap. At both the DSA and PSA, the diversity on the HP is consistently high through the first 6 s, however in the second half of the measurement the mobile has moved past the secondary source and the signal energy begins arriving from the rear of the mobile with a reduced angular spread. The diversity on the VP is similarly affected in the second half of the measurement. In the first half of the measurement on both the VP-DSA

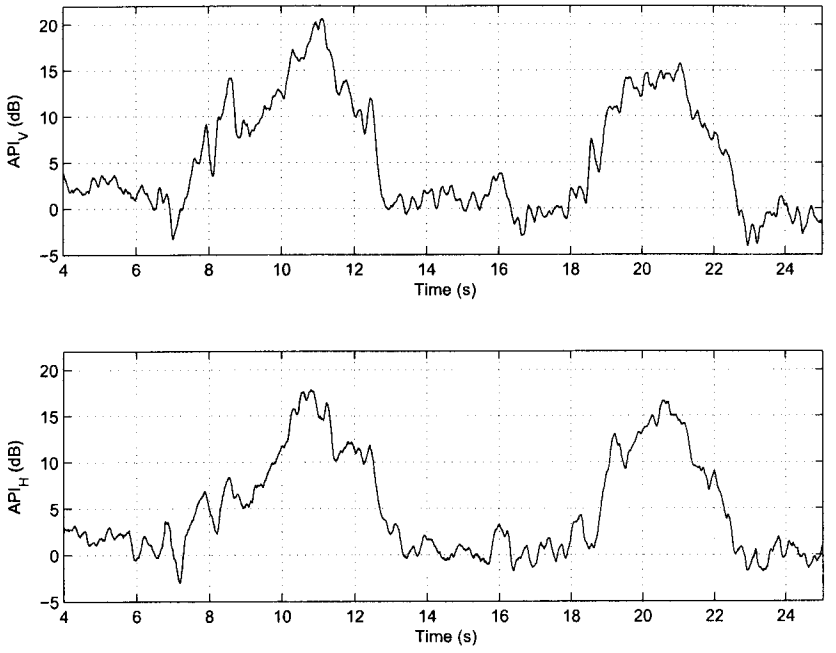

Figure 6.8: Array power imbalance measured on Kent St. API^V(top) API^H(bottom).

and VP-PSA, the momentary losses of power from the secondary signal source combined with high power levels from the intersection results in deep variations in the diversity. An example of this can be seen by comparing the diversity in Figure 6.14 with the angular distribution of power in Figure 4.2. Between 1 s and 2 s and between 3 s and 4 s the loss of signal energy on the VP-PSA from the front of the mobile results in corresponding drops in diversity in Figure 6.14.

Figure 6.15 shows the VP and HP diversity measured at both arrays along the Kent St. measurement route. At both arrays the diversity on each polarization is approximately equal with a few exceptions. Outside the intersections the diversity is between 3 and 4 at each array. At the DSA the diversity drops in the intersections as the angular spread of the dominant signal components becomes smaller. On the PSA the diversity starts to drop at 6 s, just before the mobile enters the intersection. Here, strong specular reflections from buildings west of Kent St. and south of Gloucester St. dominate the angular spectrum of the received signal energy. Once inside the intersection the buildings are no longer present and the PSA is shadowed by the mobile. As a result the diversity increases again at 10 s only to drop again as the mobile exits the intersection. The behaviour is repeated again as the mobile enters the Laurier Ave. intersection at 16 s.

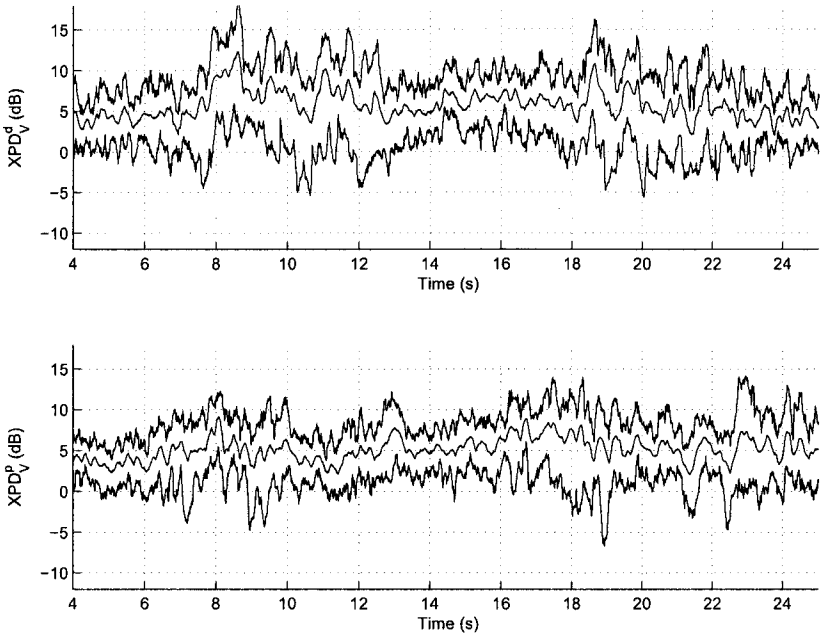

Figure 6.9: XPD^V_{max}, $\hat{\mu}_{XPD}$, XPD^V_{min} measured at the DSA (top) and PSA (bottom) on Kent St.

Summary

In comparing the plots of the angular power distribution in Chapter 4 with the XPD and diversity measure plots presented within this chapter, a relationship between each channel characteristic can be observed. In channels in which the received the angular power spectrum is directional, less scattering results in increased correlations between spatially separated elements, reducing the diversity.

These directional channels impact the XPD characteristics as well. The relationship can be observed by comparing the diversity measure and XPD plots. In general, when the diversity of a particular polarization is very low, signifying a narrow angular distribution of received signal energy, the XPD is biased toward that polarization. Often, polarized channels with low diversity result from channel conditions in which the fading is Ricean distributed. On average, the power in Ricean channel will be high, compared to a Rayleigh fading channel for example, due to the strong dominant component. As a result the XPD in these channels will be increased or decreased depending on if the co-polarized or cross-polarized channel is more Ricean, respectively. For example, between 8-9 s on the Kent St. diversity at the VP-DSA is much less than that at the HP. In this region the measured XPD values are high. Similar behaviours can be observed at the Bank St. PSA measurements between 12-13 s and at the PSA on Laurier Ave. at 20 s and 25 s. In each case, low values for the VP diversity coinciding with higher HP diversity result in increased XPD values. The opposite is true

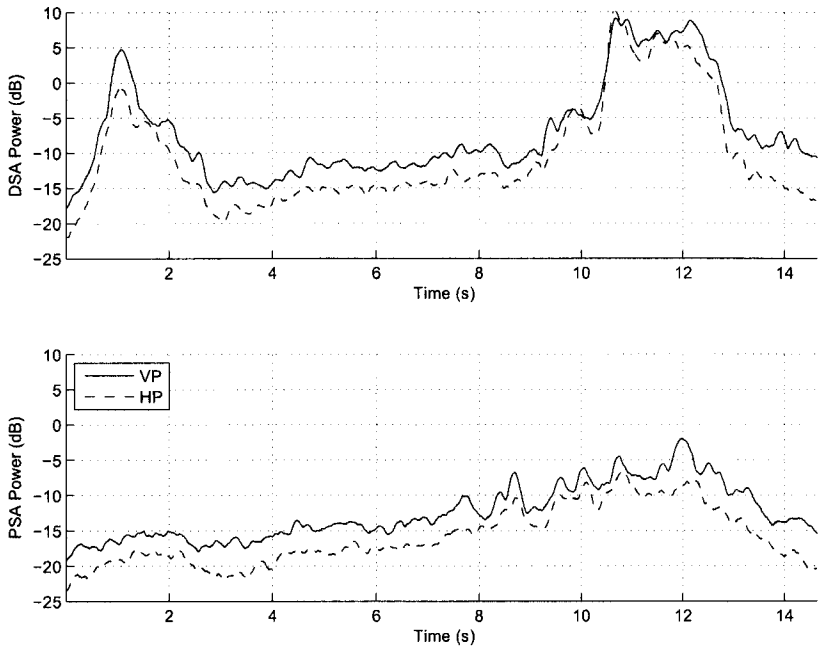

Figure 6.10: Average received power on the VP and HP channels measured at the DSA (top) and PSA (bottom) on Bank St.

when the HP diversity is low and the VP diversity is high. For example, for the channels measured at the VP-DSA at 12 s on Laurier Ave. and between 21-22 s at the HP-PSA measured on Kent St. reduced XPDs were observed.

When the diversity is low on both polarizations, as it tends to be at the DSA in the intersections on Kent St. and Bank St., the XPD has a large variance across the subchannels. Likewise, when the diversity is high on both polarizations, such as for much of the Slater St. measurement, the variance of the XPD is much less.

In this chapter considerable differences were observed in the polarized channels measured at each side of the measurement vehicle. For a MIMO system with array elements distributed on both sides of the mobile, the different channels characteristics will impact the system performance as a whole. For example, on Laurier Ave., the diversity for the 8×8 channels measured between 21-24 s (see Figure 3.3) results mainly from the diversity at the PSA (see Figure 6.13). However, the low diversity levels at the very start of that measurement result mainly from the diversity characteristic of the DSA. This is even more evident on the Kent St. and Bank St. measurements where the 8×8 diversity is highly dominated by the DSA channels.

In the next chapter, the performance impact due to the different polarized channel characteristics at each array is investigated for spatial multiplexing systems.

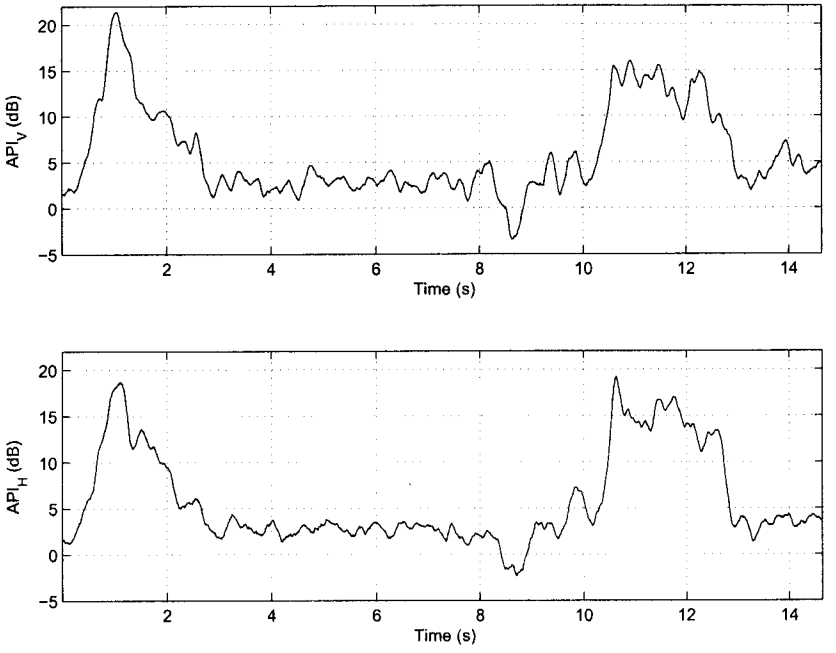

Figure 6.11: Array power imbalance measured on Bank St. API^V(top) API^H(bottom).

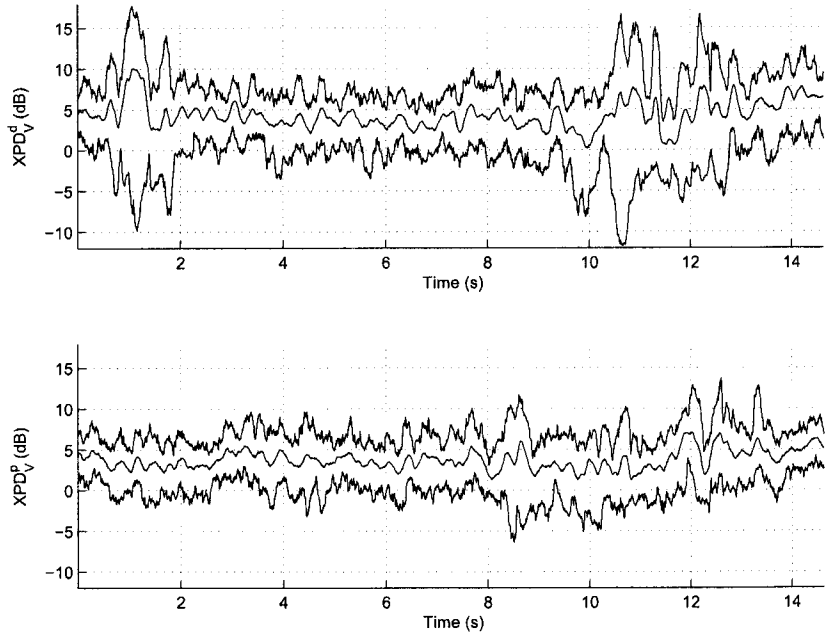

Figure 6.12: XPD^V_{max}, $\hat{\mu}_{XPD}$, XPD^V_{min} measured at the DSA (top) and PSA (bottom) on Bank St.

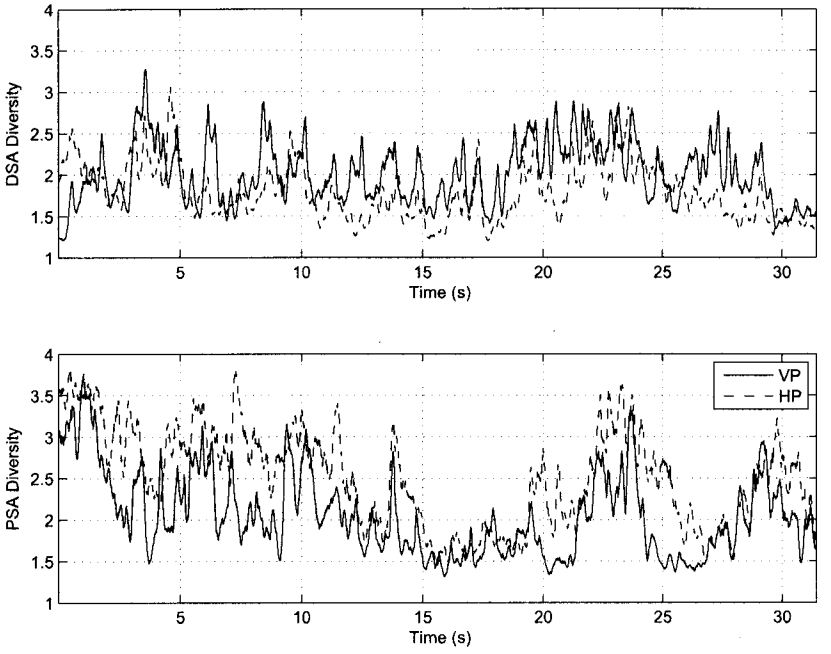

Figure 6.13: Diversity measures observed at the DSA (top) and PSA (bottom) on Laurier Ave.

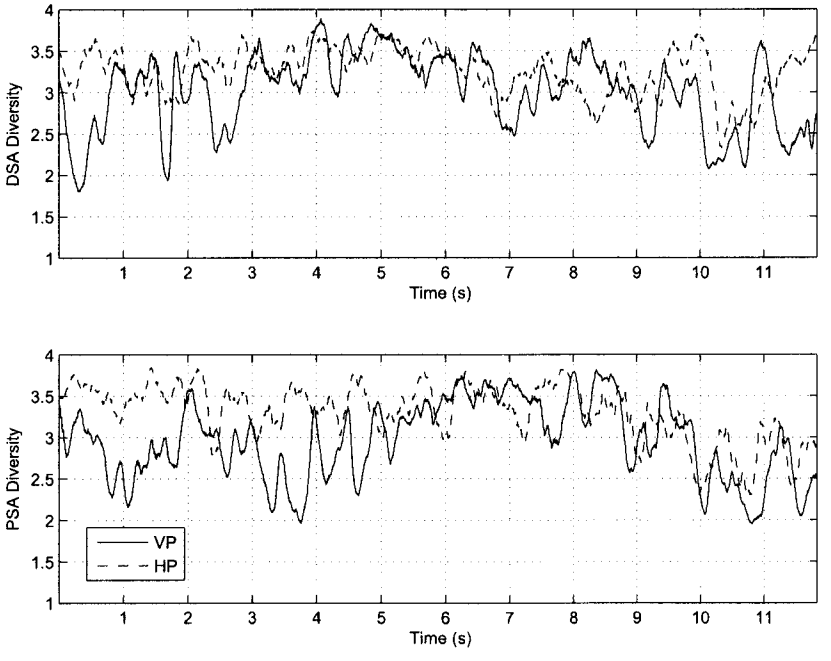

Figure 6.14: Diversity measures observed at the DSA (top) and PSA (bottom) on Slater St.

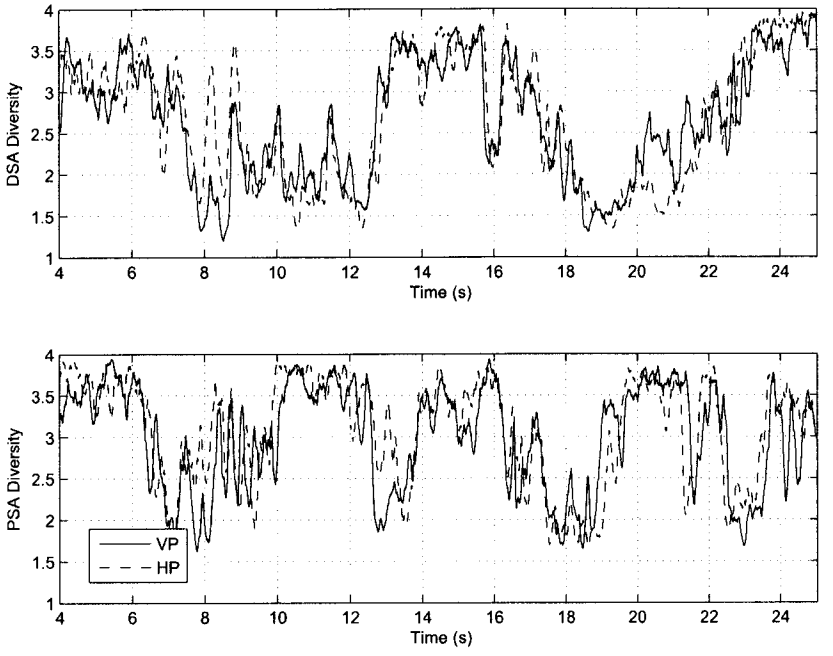

Figure 6.15: Diversity measures observed at the DSA (top) and PSA (bottom) on Kent St.

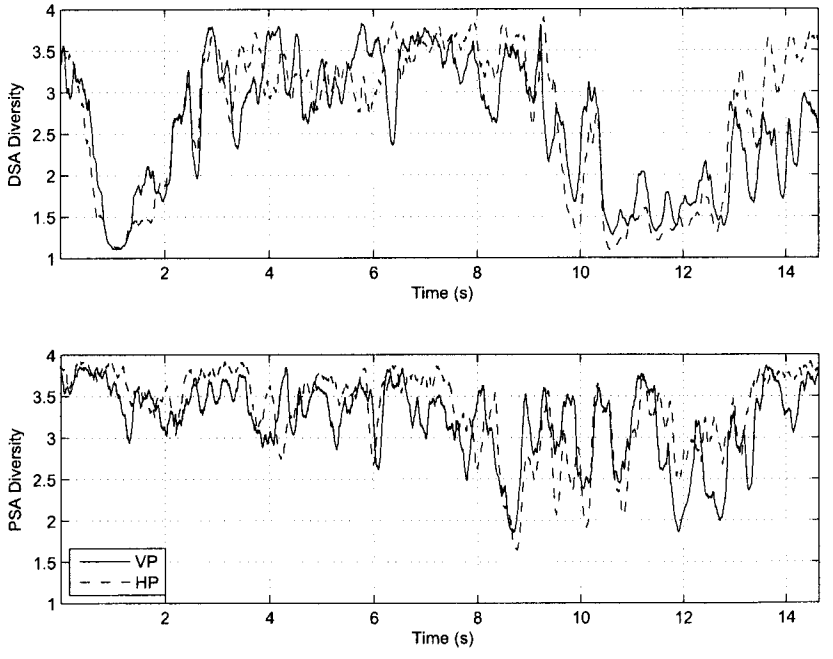

Figure 6.16: Diversity measures observed at the DSA (top) and PSA (bottom) on Bank St.

Chapter 7

Effect of Polarization on System Performance

The performance benefit of using polarization diversity in a MIMO system, with respect to a system using purely spatial diversity, comes from the lower correlations between polarized subchannels. However, this decreased correlation comes at a cost: the reduced power in the cross-polar subchannels. The requirement for balanced power in the diversity branches and the dependence on correlation must be a primary consideration when attempting to choose between system designs using these two diversity methods.

Performance comparisons of spatial and polarized MIMO communications systems have been investigated in [36, 33, 35, 34] and [26]. In [33, 35, 26] it was shown that in diversity systems such as orthogonal space-time block coding (OSTBC), polarization diversity offers no performance benefit over spatial counterparts and in fact will usually result in a performance degradation, regardless of spatial correlations.

Consider a system using the Alamouti scheme [4]. This is a 2x2 OSTBC in which two symbols are transmitted from two transmitter elements in two time periods. In the Alamouti scheme the code orthogonalizes the channel making it resilient to intersymbol interference resulting from correlation. In Rayleigh channels the error performance is dominated by the occurrence of severe multipath fading. When the spatial correlation is low, the use of polarization diversity will result in a performance degradation because of the power imbalance resulting from the XPD. If the correlation is very high, however, the performance of OSTBC will suffer as multiple subchannels enter a deep fade. In these cases the decreased subchannel correlation in a polarization diversity system can result in an improvement in performance, but only if the XPD is not high [33, 35].

Polarization diversity offers no benefit to the Alamouti scheme operating in Ricean channels with either high or low spatial correlation. In Ricean channels the performance of OSTBC is determined by the power of the dominant signal component. When the channel

is very Ricean, i.e., the dominant component is very strong, fading will be limited. As a result, attempting to use polarization diversity will result in a power imbalance due to the XPD and hence a loss in performance [33, 35].

Although polarization diversity may have limited potential for use in OSTBC schemes, performance benefits can be realized in spatial multiplexing systems. In a spatial multiplexing system the data is divided into N parallel streams which are transmitted simultaneously from each transmit array element. Whereas the Alamouti scheme is rate 1, the rate of a spatial multiplexing MIMO system is determined by the number of transmitter array elements N. Because the transmitted symbols are not necessarily encoded, spatial multiplexing systems are much more susceptible to self-interference in correlated channels. As a result, polarization diversity has shown to be promising in improving performance of spatial multiplexing, especially in correlated channels [36, 34, 26].

In this chapter the performance of V-BLAST (Vertical Bell Labs Layered Space Time) [53] is investigated for polarized spatially separated arrays as well as hybrid arrays using a combination of spatially separated, dual-polarized antennas. The discussion is begun by looking at the measured channel capacities which provide insight into how well spatial multiplexing can be expected to perform.

7.1 Capacity

7.1.1 Simulation Channel Models

For the discussion to follow a number of different channel matrices are define below. Note: for each model the same 4 transmit elements are used.

1. VP-DSA and HP-DSA refer to the 4×4 channel matrix given in (2.1) and (2.2) respectively and where $N = 4$.

2. VP-PSA and HP-PSA refer to the 4×4 channel matrix given in (2.3) and (2.4) respectively and where $N = 4$.

3. VH-DSA refers to the 4×4 dual-polarized channel matrices given by

$$\mathbf{H}_d^{VH}(t) = \begin{bmatrix} \alpha^V_{m_1 n_1}(t) & \dots & \alpha^V_{m_1 n_4}(t) \\ \alpha^H_{m_1 n_1}(t) & \dots & \alpha^H_{m_1 n_4}(t) \\ \alpha^V_{m_2 n_1}(t) & \dots & \alpha^V_{m_2 n_4}(t) \\ \alpha^H_{m_2 n_1}(t) & \dots & \alpha^H_{m_2 n_4}(t) \end{bmatrix}, \tag{7.1}$$

where the DSA receiver elements m_1 and m_2 and transmitter elements $n_1 \dots n_4$ are chosen such than the spatial separation between adjacent elements at each array is

1λ. Similarly, the channel matrices at the VH-PSA, $\mathbf{H}_p^{VH}$, are defined using the PSA receiver elements with 1λ spatial separation and the same transmitter elements that are used for the DSA analysis.

7.1.2 Measured Channel Capacity

Although capacity is not necessarily a good indicator of how well a system will perform in a given channel it does provide an upper bound as to what performance one can expect. As discussed in Chapter 1 the capacity is given by

$$C = log_2(det[\mathbf{I}_M + \frac{\gamma}{N}\mathbf{H}\mathbf{H}^\dagger]) \tag{7.2}$$

The capacities at an SNR of 21 dB calculated along each measurement route are provided in Figures 7.1 to 7.4. On each measurement route the achievable capacities are dominated by the received signal strength which is greatest at the VP arrays and lowest on the HP arrays.

Laurier Avenue

On the Laurier Ave. measurement there is a steady decline in capacity (see Figure 7.1) on both the DSA and the PSA as the mobile moves further away from the transmitter. On average the capacity is about 2 b/s/Hz greater on the DSAs than on the corresponding PSAs due to the higher signal strength at that array. Interestingly the capacity of the dual-polarized arrays (VH-DSA and VH-PSA) are almost as high as the corresponding VP arrays, even though the XPD is often high on this route. In general, the angular power distributions on the Laurier Ave. channels are narrower than those measured in the other channel environments. This results in comparatively higher correlations between spatial subchannels while the correlations between polarized subchannels remain low. Thus, for the dual-polarized arrays, the capacity loss incurred by the lower signal strength on the HP subchannels is balanced by the increase diversity gain due to lower cross-polar correlations.

Slater Street

As on Laurier Ave. the capacity on Slater St., shown in Figure 7.2, is highest on the VP and lowest on the HP, and decays as the mobile moves away from the transmitter. However, the rate at which the capacity decreases is much higher on the DSA due to the greater rate at which the signal level decreases at that side of the mobile. For the first 3 s of the measurement the capacities are higher on the DSA than on the PSA. However, after the 3 s mark, and for the following 5 s, the capacity declines on the DSA but remains more or less constant on the PSA. As a result the average capacities measured on the DSA are about 3 b/s/Hz less than those measured on the PSA through this portion of the measurement.

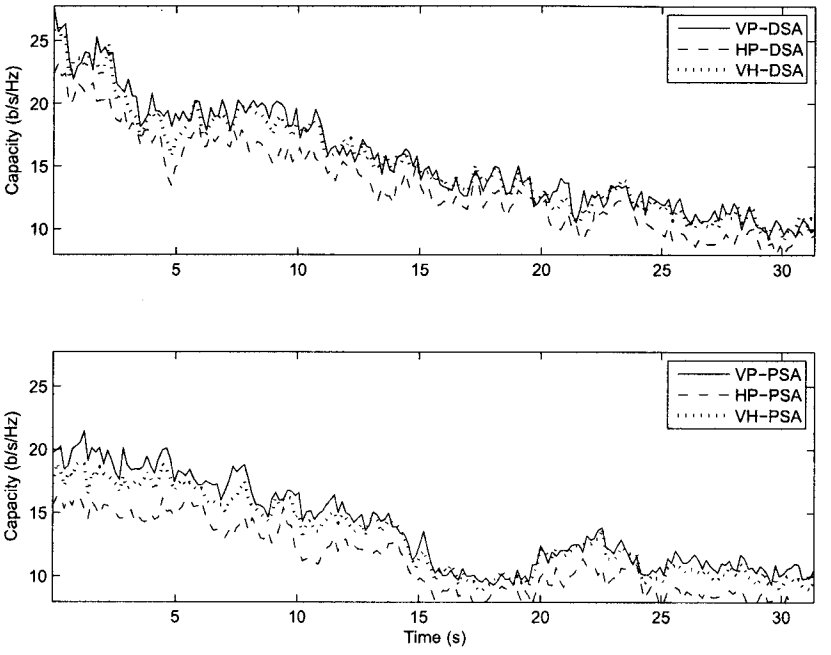

Figure 7.1: Time series of capacity measured on Laurier Ave. at the DSA (top) and PSA (bottom).

On average, at both the driver side and passenger side, the capacities of the dual-polarized arrays and HP arrays are about 2 b/s/Hz and 5 b/s/Hz less than those on the VP arrays, respectively. Recall from Section 5.2.2 that the spatial correlations measured on Slater St. were as low as the cross-polar correlations. The reduced capacity on the VH-DSA and VH-PSA therefore results from the power imbalance reflected in the XPD (see Figure 6.6). On the Slater St. measurement the dual-polarized arrays do not gain the diversity advantage observed on Laurier Ave. since the spatial correlations on Slater St. are already low.

Kent Street

The impact that the power radiating out of the Gloucester St. and Laurier Ave. intersections has on the capacities on Kent St. is immediately evident from Figure 7.3. On the DSA the capacities at the VP array increase from 3 b/s/Hz to as much as 26 b/s/Hz in the centre of the Laurier Ave. intersections. On the passenger side of the mobile the PSA is shadowed from much of this energy so the increases are not as strong. As a result, the difference in the DSA and PSA capacities measured in the intersections on Kent St. are at times more than 10 b/s/Hz. It is interesting to note that on the PSA the drop in signal energy when the mobile is in the centre of the intersections translates to a corresponding drop in capacity at that array.

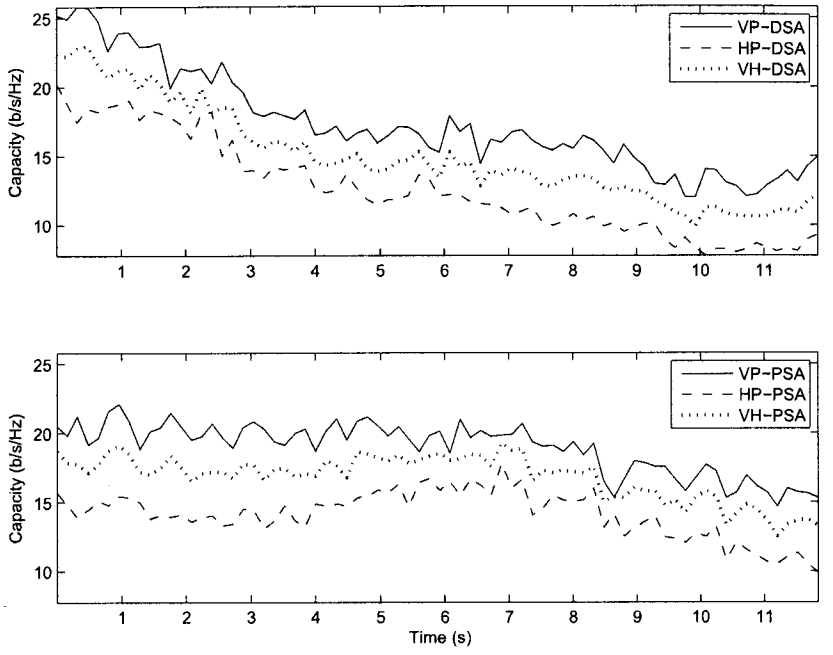

Figure 7.2: Time series of capacity measured on Slater St. at the DSA (top) and PSA (bottom).

In the intersection regions of the measurements the VP channels often exhibit higher spatial correlations at the DSA. In these regions the capacities on the dual-polarized array are only about 1 b/s/Hz worse than those measured on the VP. Again this is likely due in part to the decreased correlation on the cross-polar subchannels.

Bank Street

The capacities on Bank St. (Figure 7.4) behave similarly to those on Kent St. In the intersections regions the DSA experiences large capacity increases due to the power funneling out of the Gloucester St. and Laurier Ave. intersections. In these regions on Bank St. the dual-polarized array often performs as well as or better than the VP array even though many of the subchannels in these regions experience large XPD. Again this is an example of the diversity gain from the lower cross-polarization correlations in these regions as compared to the VP spatial correlations.

7.2 VBLAST Detection

The V-BLAST algorithm [53] is a MIMO detection technique for spatial multiplexing. In a V-BLAST system, independent streams of uncoded data are transmitted simultaneously

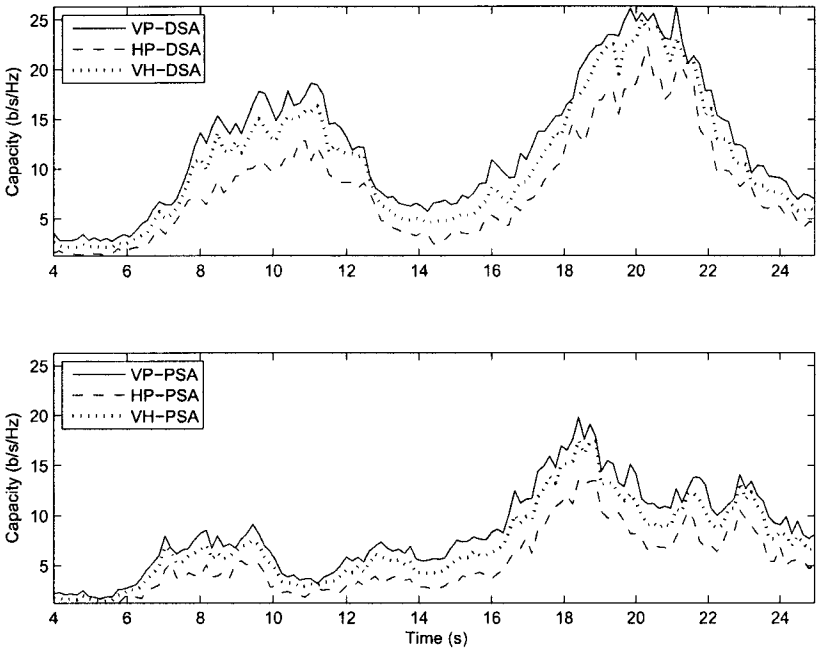

Figure 7.3: Time series of capacity measured on Kent St. at the DSA (top) and PSA (bottom).

from each transmit array element and are detected using the V-BLAST successive interference cancellation algorithm. The receiver uses a channel matrix estimate to determine the transmit element with the highest SINR, where the interference is considered to be the signals transmitted from the other transmitter elements. A weighted nulling technique, such as minimum mean squared error (MMSE) or zero forcing (ZF), is then used to extract the desired signal from the received signal vector. The data symbols are estimated and subtracted from the received signal at which point the algorithm repeats, selecting the next transmit element with the highest SINR. By estimating and canceling the strongest signal first, the largest source of interference for the other transmit streams is removed, thus improving the symbol estimations on the following iterations.

In a V-BLAST system, the transmitter has no knowledge of the channel so, for the system to operate with an acceptable error performance, multipath propagation is required to decorrelate the subchannels. However, if the decorrelation is not sufficient, the successive cancellation of interference will result in errors propagating through each layer of detection. In environments where the amount of multipath propagation is low, the correlation between spatially separated array elements may be high. In these environments, polarization diversity may offer some performance benefits over traditional spatial systems since cross-polarized subchannel correlations are often lower.

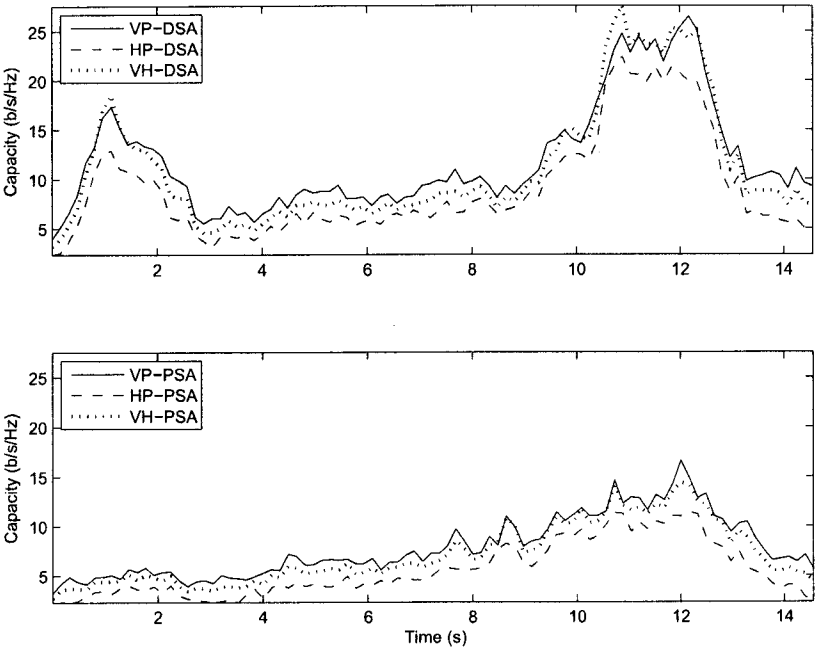

Figure 7.4: Time series of capacity measured on Bank St. at the DSA (top) and PSA (bottom).

7.2.1 4x4 V-BLAST Performance Simulations

In this section, the results of 4×4 V-BLAST simulations, run on the measured channels, are presented. The received signal $\mathbf{r}[k]$ at sample index k is modeled as

$$\mathbf{r}[k] = \mathbf{H}[k]\mathbf{s}[k] + \mathbf{n}[k], \tag{7.3}$$

where the length-N vector of transmitted symbols $\mathbf{s}$ are drawn from a QPSK constellation and the complex vector $\mathbf{n}$ consists of AWGN values with variance N_o. For each array configuration the channel matrices presented in Section 7.1.1 are substituted for $\mathbf{H}$.

Prior to performing the simulations, the channels are first normalized. Since each array configuration experiences different power levels, the normalization factor η is calculated with respect to the VP-DSA such that

$$\eta = \sqrt{\frac{1}{MNK}\sum_{k=1}^{K} \|\mathbf{H}_d^V[k]\|_F^2}, \tag{7.4}$$

where K is the number of samples in the measurement time series. This normalization factor is then applied to the channel matrices measured at each array configuration. In this manner the SNR discussed represents the power levels at the VP-DSA and the performance difference resulting, in part, from the differences in power levels at each array configuration will be reflected in the performance curves.

Laurier Avenue

The time series of bit error rates (BER) for a 4x4 V-BLAST system simulated on Laurier Ave. are plotted in Figure 7.5 for a normalized SNR of 21 dB. In the upper portion of the figure, the curve designated VP-DSA (HP-DSA) applies to the V-BLAST system consisting of only spatially separated uni-polarized antenna elements with VP (HP) antennas at the DSA. The VH-DSA refers to the hybrid system using two dual-polarized receive antennas spatially separated by 1λ at the DSA. The lower portion of the figure plots the BER for the corresponding arrays at the PSA.

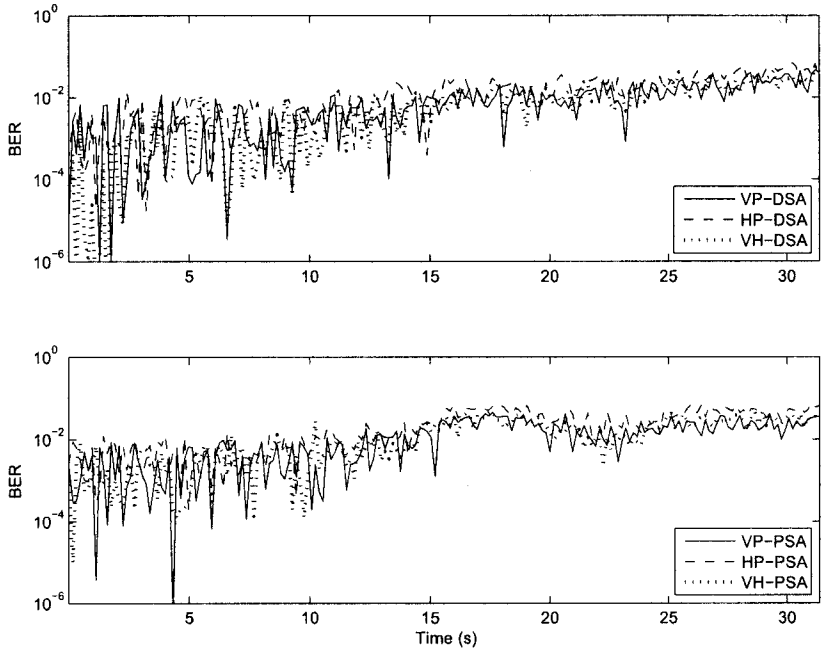

Figure 7.5: Time series of BER for a 4 × 4 V-BLAST system using uni-polarized (vertical and horizontal) and dual-polarized receive antennas. The simulation is run using channel data measured on Laurier Ave. with a normalized SNR of 21 dB.

As the mobile progresses down the Laurier Ave. urban canyon the performance degrades on all the systems simulated. This is due to the increasing path loss as the mobile moves further away from the transmitter. On both sides of the mobile the performance of the VP and VH systems are roughly equivalent. Even though the XPD is often high on this route, the diversity (Figure 6.13) at the VP array is generally low while the VH-DSA generally exhibits low polarization correlation (Figure 5.1a). As mentioned in Section 7.1.2, the lower cross-polar correlation compensates for the performance loss due to the power imbalance in the polarization branches resulting in a minimal loss in performance.

In general the performance of the DSA channels is better than that of the PSA. Since

there is little difference between the spatial correlations at the DSA and PSA, the lower BERs are mainly due to the increased power at those arrays.

As mentioned earlier, the BER performance of the VP and VH arrays at both the DSA and the PSA are nearly identical while the HP arrays perform the worst. For this channel environment, both the VP spatial DSA or PSA could be replaced by a dual-polarized array without a significant loss in performance but with reduction in the size of the array from 3λ to 1λ.

Slater Street

Figure 7.6 shows the BER for a V-BLAST system operating on Slater St. Of the four measurement routes the spatial correlations measured on Slater St. were the lowest, only slightly higher than the polarized correlations. As a result the diversity on this measurement route is high for the spatial arrays and a performance loss is expected from using polarization diversity due to the XPD. This is indicated in Figure 7.6 in which the VH system is rarely observed to perform as well as or better than the higher power VP arrays.

Although the signal energy measured on Slater St. begins stronger on the DSA, the rate at which the signal level decays is greater on the DSA than on the PSA. This is due to the secondary signal source resulting from the gap between buildings on the south side of Slater St. As a result the average performance is better at the PSA than at the DSA.

Kent Street

The BER performance of the V-BLAST simulations on Kent St. is shown in Figure 7.7. As hinted at by the capacity plot in Figure 7.3 the V-BLAST performance is best in the intersections. Even given the low diversity within these regions the high SNR still result in a performance improvement.

Figure 7.8 plots the results of the V-BLAST simulations run on Kent St. when power control is present. The power control is implemented using the VP-DSA channel matrices $\mathbf{H}_d^V$ as a reference and normalizing the channels of each array configuration by

$$\eta[k] = \sqrt{\frac{1}{MNL} \sum_{l=k-L/2+1}^{k+L/2} \|\mathbf{H}_d^V[l]\|_F^2}, \tag{7.5}$$

where k is the sample index and $L = 250$ samples. By implementing power control on the measured channels, the dependency of the simulations on the received power is removed and the impact of the other channel characteristics becomes clearer.

With power control the BER performance becomes dominated by the spatial and cross-polar correlations and by the XPD. As the mobile enters the intersections where the correlations and XPD are highest the performance gets worse on all array configurations. This

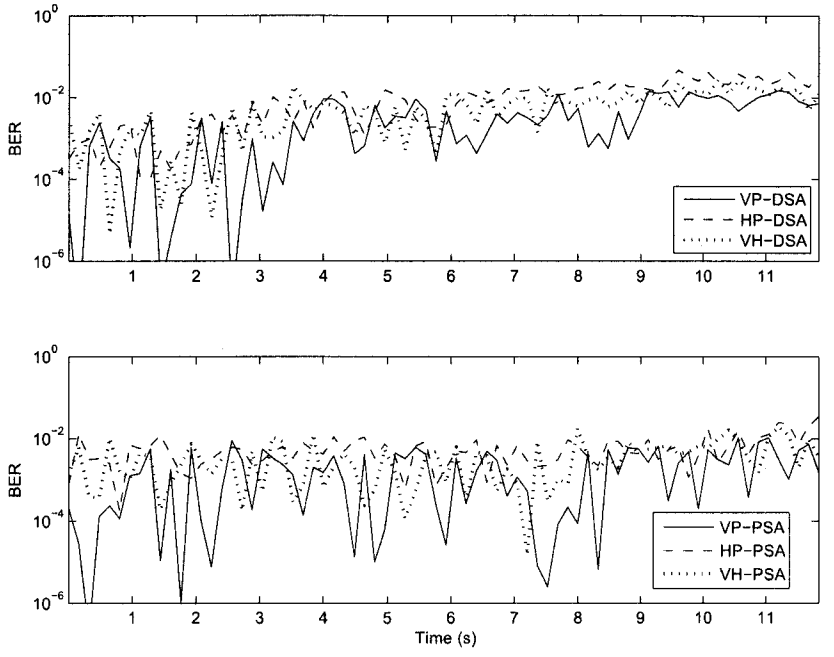

Figure 7.6: Time series of BER for a 4 × 4 V-BLAST system using uni-polarized (vertical and horizontal) and dual-polarized receive antennas. The simulation is run using channel data measured on Slater St. with a normalized SNR of 21 dB.

is most noticeable on the PSA where the effects of the API, discussed in Chapter 6, result in increased error rates. Because the PSA is shadowed by the mobile, the power drops considerably in the intersections resulting in an increase in detection errors.

Figure 7.9 shows the BER for increasing E_b/N_o averaged over the whole Kent St. measurement. At a BER of 10^{-3} the channels measured at the PSA require about 7 dB more signal power than their DSA counterparts. On each side of the mobile the VP arrays are the best performers with the dual-polarized configurations trailing by about 2 dB.

Bank Street

The time series of BERs for the V-BLAST simulations run on the Bank St. channels are given in Figure 7.10. As on Kent St. the performance of the DSA improves when the mobile enters the intersections. At the PSA however, the improvement is only noticeable in the Laurier Ave. intersection since the signal strength reaching that side of the mobile does not increase significantly in the Gloucester St. intersection (see Figure 6.10).

On the DSA the performance of the dual-polarized array is very close to that of the VP array. This is clearer in the BERs simulated on the power controlled channels shown in Figure 7.11. On the DSA the performance of the dual-polarized channels is often equivalent

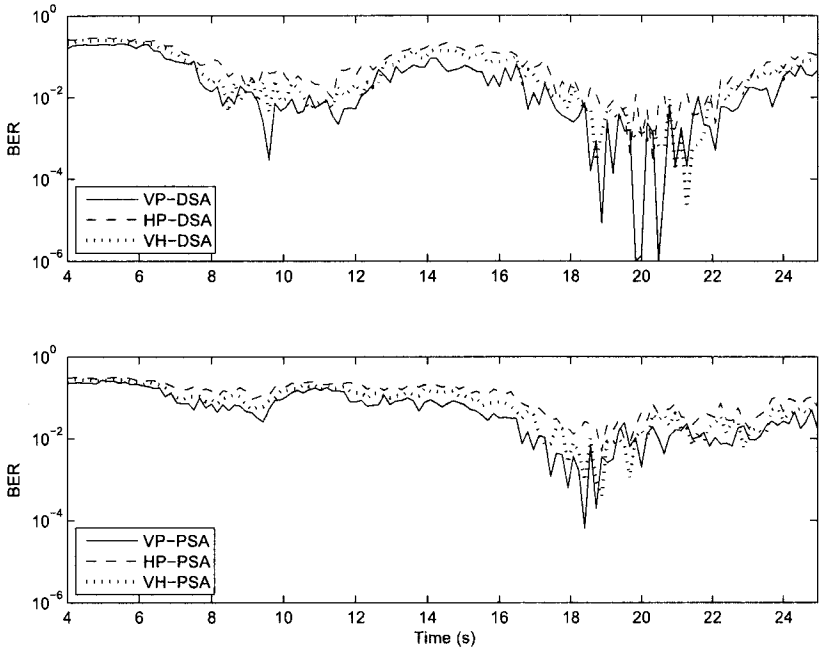

Figure 7.7: Time series of BER for a 4 × 4 V-BLAST system using uni-polarized (vertical and horizontal) and dual-polarized receive antennas. The simulation is run using channel data measured on Kent St. with a normalized SNR of 21 dB.

to or better than those of the VP channels. At the PSA the performance of the dual-polarized array is only marginally worse than the VP array. In both cases the error performance degrades as the mobile enters the intersections due to the increased spatial and, to a lesser degree, cross-polar correlations in these regions.

Again the effect of the API is clear in Figure 7.11 as significant increases in the error rate occur at the PSA within the intersection regions when power control is used. On the DSA the performance degradation in the intersections is dominated by increased correlations resulting from the increased directionality of the angular spectrum. However, the increased error rates on the PSA result from a drop in SNR on that side of the mobile.

The overall performance on each set of channels is plotted in the BER curves in Figure 7.12. On each side of the mobile the dual-polarized arrays perform almost as well as the VP arrays and about 4 dB better than the HP array at a BER of 10^{-3} on the DSA.

Summary

In this chapter, the performance of uni-polarized and dual-polarized V-BLAST systems was compared with respect to the array placement on two sides of the measurement vehicle. It has been demonstrated that there is generally a performance advantage in using vertically

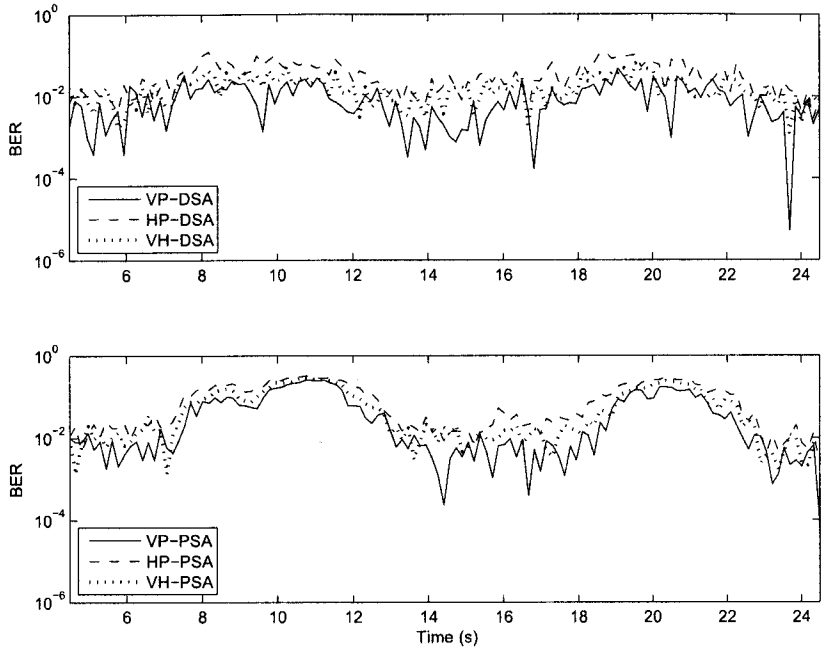

Figure 7.8: Time series of BER for a 4 × 4 V-BLAST system using uni-polarized (vertical and horizontal) and dual-polarized receive antennas. The simulation is run using channel data measured on Kent St. with power control and a normalized SNR of 21 dB.

polarized, spatially separated arrays as opposed to a combination of dual-polarized antennas. However, the use of dual-polarized systems only results in performance losses of a few dB and can reduce the footprint of the array significantly. Further, there is often a significant advantage in having arrays located on one side of the vehicle as opposed to the other, especially in those scenarios where one array is severely shadowed by the mobile. In practical scenarios the optimum vehicular location for the array elements will change depending on the environment and the mobile's location with respect to the transmitter. As a result, it may be in the systems designer's best interest to distribute the array elements about the vehicle. In this manner only a subset of the array elements will experience the extreme shadowing or correlations and the system should provide a 'middle of the road' level performance.

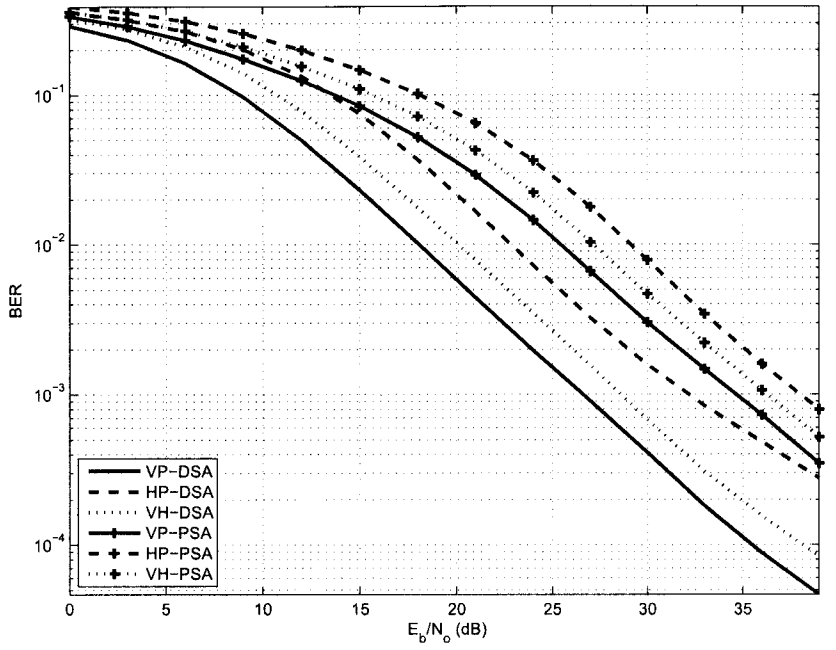

Figure 7.9: BER curves for uni-polarized (vertical and horizontal) and dual-polarized 4 × 4 V-BLAST systems. The results are averaged over channel data measured on Kent St.

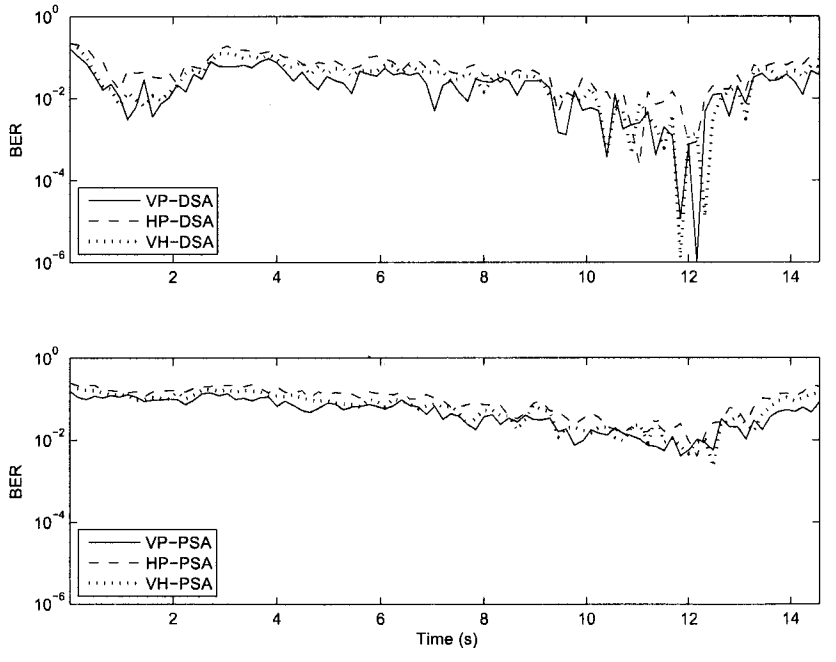

Figure 7.10: Time series of BER for a 4 × 4 V-BLAST system using uni-polarized (vertical and horizontal) and dual-polarized receive antennas. The simulation is run using channel data measured on Bank St. with a normalized SNR of 21 dB.

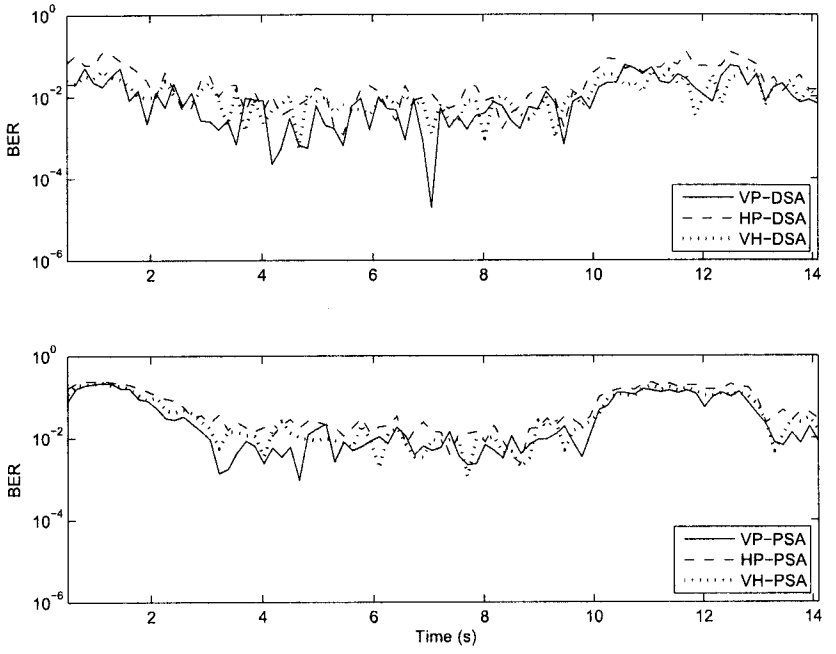

Figure 7.11: Time series of BER for a 4 × 4 V-BLAST system using uni-polarized (vertical and horizontal) and dual-polarized receive antennas. The simulation is run using channel data measured on Kent St. with power control and a normalized SNR of 21 dB.

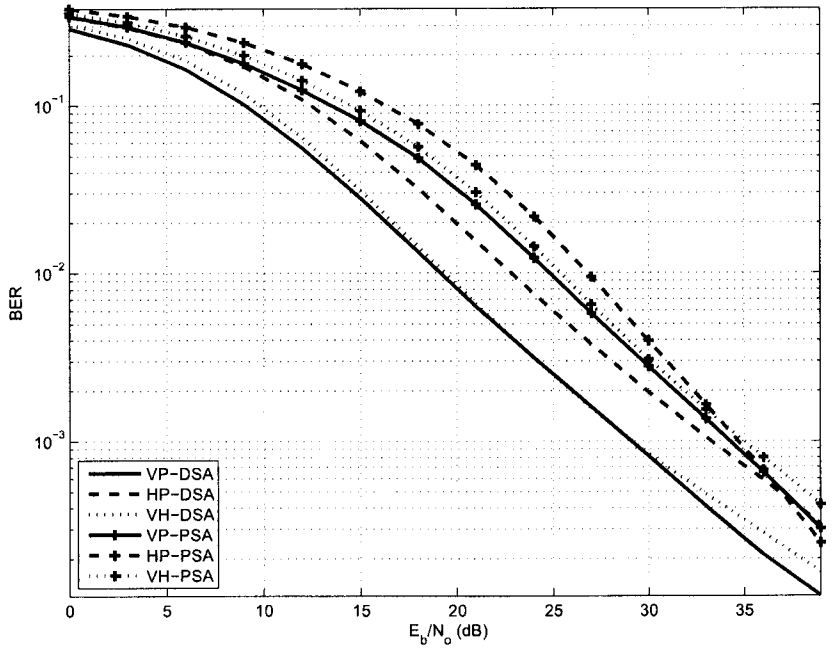

Figure 7.12: BER curves for uni-polarized (vertical and horizontal) and dual-polarized 4 × 4 V-BLAST systems. The simulation is run using channel data measured on Bank St.

Chapter 8

Conclusions

In this thesis, measurements and analysis of polarized MIMO channels in urban environments are presented. Modifications were made to the CRC-MCS to allow it to perform near simultaneous measurements of orthogonally polarized MIMO channels using linearly dual-polarized receive antenna array elements. The elements of the receive array were positioned on two sides of a measurement vehicle which was used to collect channel responses in a number of different propagation environments. At each array position, considerable variation in the MIMO channel characteristics were measured depending on the local propagation environment and the orientation of the vehicle relative to the transmitter location.

The measurement routes discussed consisted of both specular and scattering environments. The propagation characteristics of the Laurier Ave. and Gloucester St. urban canyons tend to exhibit a small number of dominant signal components. The measurements recorded along Kent St. and Bank St. consist of both specular and multipath regions dependent on the mobile's location relative to the intersection regions and the position of the receive array relative to the transmitter. The measurements on Slater St. exhibit the highest degree of multipath, resulting mainly from the secondary source of energy radiating into the urban canyon.

The polarized power levels received were highly dependent on the local propagation conditions resulting from intersections, gaps between buildings, the presence of narrow urban canyons, and the orientation of the receive array with respect to the dominant signal sources. In general, the average power received on the vertically polarized channels was greater than that measured on the horizontal polarization and resulted in average values for the XPD^V which ranged from 3-5 dB.

In general, the diversity levels measured at each polarization were very similar, indicating that the angular distributions of power received at both the VP and HP tend to be comparable. However, the polarized diversities did differ in some measurement regions, the most notable being at the PSA on portions of the Laurier Ave. and Slater St. measurements. The

greatest similarities in the polarized diversity behaviour were observed on the Kent St. and Bank St. measurements where the diversity was high outside of the intersection areas but dropped significantly within the intersections. In these regions, the angular spectrum of the received power was highly directional due to the strong signal components radiating out of the street canyons. As a result, increases in the spatial correlations between receiver elements were observed in these regions. However, even in these highly directional environments, the colocated, cross-polar subchannels were much more robust to increases in correlation.

Increases in both the average XPD and variance of the XPD measured across the array subchannels were observed in areas where the channels were highly directional. The fading envelopes in these channels often have Rician distributions in which the power in the dominant component can vary significantly between subchannels and across polarizations. This results in significant variations in the powers received on each subchannel. On some subchannels, the strength of the dominant component is much larger on one polarization than on the other. On these subchannels the XPD^V values measured are as much as 7 dB above or 15 dB below the mean value across the array, depending on which polarization is stronger.

Considerable variations of the channel characteristics were observed at the subchannels measured on opposite sides of the mobile. Although the most extreme example occurs on those measurement routes where one side of the mobile is oriented toward the transmitter, as on Kent St. and Bank St., significant differences were also measured on Slater St. and Laurier Ave. indicating the channel characteristics are also highly impacted by the proximity of buildings and the presence of traffic. When the received signal energy is highly incident on one side of the mobile (as on Kent St. and Bank St.) a portion of the array becomes shadowed and must rely on the presence of buildings to provide reflected multipath components. More often though, buildings result in shadowing and the openings between buildings provide propagation routes for signal energy to travel to the receiver. As a result different environments can result in a significant imbalance in the power received at various locations of the mobile. In these measurements, differences in the average power received at each side of the mobile were characterized by the API and measured to be as high as 20 dB. The behaviour of the API was very similar for both polarizations.

For MIMO communications this power imbalance has a significant effect on the performance of the system. In the intersection regions, the directional energy radiating out of the street canyons resulted in drops in diversity and increases in spatial correlations, creating conditions less than ideal for MIMO communications. However, because these regions also experience significant increases in received power, the performance loss resulting from subchannel correlation is significantly outweighed by the improved SNR. As a result, under a condition of constant transmit power, the performance in these regions improves. However,

when power control is implemented the impact of the channel structure becomes evident. In regions where the channels are dominated by a small number of eigenmodes, the performance degrades. For most propagation environments, dual-polarized channels exhibit at least two strong eigenmodes, one for each polarization. However, because the XPD can often be quite strong in these regions the impact of the reduced power at the horizontal polarization inhibits the gain achieved. On many of the channels investigated in this thesis, only a slight degradation in the system performance results from the use of dual-polarized antennas, but the savings is a reduction of the size of the array footprint by about one half.

From the measurements and analysis presented within this thesis, it is clear that the placement of array elements in vehicular MIMO will have a significant impact on the system performance. As the vehicle moves through an urban environment the characteristics of the channel can vary significantly. Further, the statistics of the channels experienced by each array element cannot be considered to be identically distributed. This departure from the theoretically ideal channel models, in which the channel coefficients are considered to be i.i.d., should be a consideration for system designers involved in the deployment of vehicular MIMO systems.

8.1 Future Work

The measurements and analysis discussed within this thesis suggest a number of additional avenues of investigation through which understanding of polarized MIMO channels can be extended. A number of these are suggested below.

Measurements with dual-polarized transmit antennas

The measurements discussed focused on the reception of dual-polarized signals resulting from the transmission and depolarization of VP signals. However, further insight into polarized channel behaviour could be gained by modifying the transmission system to use HP elements as well. Such measurements would allow for the analysis of cross-polarized channels resulting from HP sources.

Studying the impact of polarization angles

This thesis investigated the properties of vertically and horizontally polarized MIMO channels where polarization angles of the VP and HP is 90° and 0°, respectively. The investigation of alternate polarization angles, ±45° for example, may also provide useful insight.

Alternate antenna locations

This thesis also investigated the impact of array element placement on the measured channel characteristics with the array elements positioned two sides of the mobile. Further investigation into alternate distributions of array elements are necessary to develop a complete understanding of the impact of vehicular array locations. Comparing the channels measured at the sides, roof, front and rear of the mobile may lead to useful conclusions for the practical implementations of vehicular arrays.

Nonidentical distributions of subchannel coefficients

Analysis of the measured channel data revealed significant differences in the channel characteristics between array elements. Characterization of the variations in the power, fading distributions, XPD, and correlation across the MIMO subchannels could reveal useful insight into the practical performance of MIMO communications techniques.

Bibliography

[1] W. C. Jakes, *Microwave Mobile Communications*, W. C. Jakes, Ed. New York: IEEE Press, 1993.

[2] W. Lee and Y. Yeh, "Polarization diversity system for mobile radio," *IEEE Transactions on Communications*, vol. 20, no. 5, pp. 912–923, Oct. 1972.

[3] A. F. Molisch, *Wireless Communications*. John Wiley & Sons, 2005.

[4] S. M. Alamouti, "A simple transmit diversity technique for wireless communications," *IEEE Journal on Selected Areas in Communications*, vol. 16, no. 8, pp. 1451–1458, Oct. 1998.

[5] G. J. Foschini, "Layered space-time architecture for wireless communication in a fading environment when using multiple antennas," *Bell Labs Technical Journal*, vol. 1, no. 2, pp. 41–59, 1996.

[6] J. Winters, "On the capacity of radio communication systems with diversity in a Rayleigh fading environment," *IEEE Journal on Selected Areas in Communications*, vol. 5, no. 5, pp. 871–878, Jun. 1987.

[7] G. J. Foschini and M. J. Gans, "On limits of wireless communications in a fading environment when using multiple antennas," *Wireless Personal Communications*, vol. 6, no. 3, pp. 311–335, Mar. 1998.

[8] C. E. Shannon, "Communication in the presence of noise," in *Proc. IRE*, vol. 37, Jan. 1949, pp. 10–21.

[9] I. E. Telatar, "Capacity of multi-antenna gaussian channels," *European Transactions on Telecommunications*, vol. 10, no. 6, pp. 585–595, 1999.

[10] V. A. Aalo, "Performance of maximal-ratio diversity systems in a correlated Nakagami-fading environment," *IEEE Transactions on Communications*, vol. 43, no. 8, pp. 2360–2369, Aug. 1995.

[11] J. P. Kermoal, L. Schumacher, K. I. Pedersen, P. E. Mogensen, and F. Frederiksen, "A stochastic MIMO radio channel model with experimental validation," *IEEE Journal on Selected Areas in Communications*, vol. 20, no. 6, pp. 1211–1226, Aug. 2002.

[12] A. Paulraj, R. Nabar, and D. Gore, *Introduction to space-time wireless communications.* Cambridge University Press, 2003.

[13] R. Vaughan and J. Andersen, *Channels, Propagation and Antennas for Mobile Communications.* IEE, London, 2003.

[14] G. Porter, "Measurement of polarization statistics of signals received over a short range HF path," *IEEE Transactions on Communication Technology*, vol. 14, no. 4, pp. 484–494, Aug. 1966.

[15] S. Kozono, T. Tsuruhara, and M. Sakamoto, "Base station polarization diversity reception for mobile radio," *IEEE Transactions on Vehicular Technology*, vol. 33, no. 4, pp. 301–306, Nov. 1984.

[16] R. G. Vaughan, "Polarization diversity in mobile communications," *IEEE Transactions on Vehicular Technology*, vol. 39, no. 3, pp. 177–186, Aug. 1990.

[17] A. M. D. Turkmani, A. A. Arowojolu, P. A. Jefford, and C. J. Kellett, "An experimental evaluation of the performance of two-branch space and polarization diversity schemes at 1800 MHz," *IEEE Transactions on Vehicular Technology*, vol. 44, no. 2, pp. 318–326, May 1995.

[18] C. C. Martin, J. H. Winters, and N. R. Sollenberger, "MIMO radio channel measurements: performance comparison of antenna configurations," in *Proc. Vehicular Technology Conference (VTC '01 Fall)*, vol. 2, Oct. 7–11, 2001, pp. 1225–1229.

[19] V. Erceg, P. Soma, D. S. Baum, and S. Catreux, "Multiple-input multiple-output fixed wireless radio channel measurements and modeling using dual-polarized antennas at 2.5 GHz," *IEEE Transactions on Wireless Communications*, vol. 3, no. 6, pp. 2288–2298, Nov. 2004.

[20] V. Erceg, H. Sampath, and S. Catreux-Erceg, "Dual-polarization versus single-polarization MIMO channel measurement results and modeling," *IEEE Transactions on Wireless Communications*, vol. 5, no. 1, pp. 28–33, Jan. 2006.

[21] K. Sulonen, P. Suvikunnas, L. Vuokko, J. Kivinen, and P. Vainikainen, "Comparison of MIMO antenna configurations in picocell and microcell environments," *IEEE Journal on Selected Areas in Communications*, vol. 21, no. 5, pp. 703–712, Jun. 2003.

[22] J. Ling, D. Chizhik, D. Samardzija, and R. A. Valenzuela, "Peer-to-peer MIMO radio channel measurements in a rural area," *IEEE Transactions on Wireless Communications*, vol. 6, no. 9, pp. 3229–3237, Sep. 2007.

[23] E. M. Vitucci, V.-M. Kolmonen, V. Degli-Esposti, and P. Vainikainen, "Analysis of radio propagation in co- and cross-polarization in urban environment," in *Proc. IEEE 10th International Symposium on Spread Spectrum Techniques and Applications (ISSSTA '08)*, Aug. 25–28, 2008, pp. 277–281.

[24] J. P. Kermoal, L. Schumacher, F. Frederiksen, and P. E. Mogensen, "Polarization diversity in MIMO radio channels: experimental validation of a stochastic model and performance assessment," in *Proc. Vehicular Technology Conference (VTC '01 Fall)*, vol. 1, 2001, pp. 22–26.

[25] L. R. Nair, B. T. Maharaj, and J. W. Wallace, "Capacity and robustness of single- and dual-polarized MIMO systems in office and industrial indoor environments," in *Proc. IEEE Global Telecommunications Conference (GLOBECOM '07)*, Nov. 26–30, 2007, pp. 4522–4526.

[26] W. Q. Malik and D. J. Edwards, "Measured MIMO capacity and diversity gain with spatial and polar arrays in ultra wideband channels," *IEEE Transactions on Communications*, vol. 55, no. 12, pp. 2361–2370, Dec. 2007.

[27] P. Kyritsi, D. C. Cox, R. A. Valenzuela, and P. W. Wolniansky, "Effect of antenna polarization on the capacity of a multiple element system in an indoor environment," *IEEE Journal on Selected Areas in Communications*, vol. 20, no. 6, pp. 1227–1239, Aug. 2002.

[28] V. R. Anreddy and M. A. Ingram, "Capacity of measured Ricean and Rayleigh indoor MIMO channels at 2.4 GHz with polarization and spatial diversity," in *Proc. IEEE Wireless Communications and Networking Conference (WCNC '06)*, vol. 2, 3–6 April 2006, pp. 946–951.

[29] J.-M. Molina-Garcia-Pardo, J.-V. Rodriguez, and L. Juan-Llacer, "Polarized indoor MIMO channel measurements at 2.45 GHz," *IEEE Transactions on Antennas and Propagation*, vol. 56, no. 12, pp. 3818–3828, Dec. 2008.

[30] M. F. A. Kadir, M. K. Suaidi, M. Z. A. Aziz, M. R. C. Rose, M. S. R. M. Shah, D. Misman, and M. K. A. Rahim, "Measurement of 2.4 GHz MIMO channel using polarization diversity," in *Proc. International Conference on Electronic Design (ICED '08)*, Dec. 1–3, 2008, pp. 1–5.

[31] W. Kotterman, G. Sommerkorn, and R. Thoma, "Cross-correlation values for dual-polarised indoor MIMO links and realistic antenna elements," *3rd International Symposium on Wireless Communication Systems (ISWCS '06)*, pp. 505–509, Sept 2006.

[32] M. Shafi, M. Zhang, A. L. Moustakas, P. J. Smith, A. F. Molisch, F. Tufvesson, and S. H. Simon, "Polarized MIMO channels in 3-D: models, measurements and mutual information," *IEEE Journal on Selected Areas in Communications*, vol. 24, no. 3, pp. 514–527, Mar. 2006.

[33] R. U. Nabar, H. Bolcskei, V. Erceg, D. Gesbert, and A. J. Paulraj, "Performance of multiantenna signaling techniques in the presence of polarization diversity," *IEEE Transactions on Signal Processing*, vol. 50, no. 10, pp. 2553–2562, Oct. 2002.

[34] Y. Deng, A. Burr, and G. White, "Performance of MIMO systems with combined polarization multiplexing and transmit diversity," in *Proc. Vehicular Technology Conference (VTC '05 Spring)*, vol. 2, May 30–Jun. 1, 2005, pp. 869–873.

[35] C. Oestges, B. Clerckx, M. Guillaud, and M. Debbah, "Dual-polarized wireless communications: From propagation models to system performance evaluation," *IEEE Transactions on Wireless Communications*, vol. 7, no. 10, pp. 4019–4031, Oct. 2008.

[36] H. Bolcskei, R. U. Nabar, V. Erceg, D. Gesbert, and A. J. Paulraj, "Performance of spatial multiplexing in the presence of polarization diversity," in *Proc. IEEE International Conference on Acoustics, Speech, and Signal Processing (ICASSP '01)*, vol. 4, May 7–11, 2001, pp. 2437–2440.

[37] C. Oestges, V. Erceg, and A. J. Paulraj, "Propagation modeling of MIMO multipolarized fixed wireless channels," *IEEE Transactions on Vehicular Technology*, vol. 53, no. 3, pp. 644–654, May 2004.

[38] C. C. Squires, T. J. Willink, and B. Gagnon, "A flexible platform for MIMO channel characterisation and system evaluation," *Proc. Wireless 2003*, vol. 2, pp. 441–450, 2003.

[39] J. J. Carr, *Practical Antennas Handbook*, 2nd ed. TAB/McGraw-Hill, 1994.

[40] N. Gagnon, A. Petosa, and J. Bradley, "Design of dual-polarized probe-fed microstrip patch antennas for MIMO application," Communications Research Centre / Industry Canada, Ottawa, CRC Report CRC-RP-2007-02, June 2007.

[41] T. J. Willink, "Wide-sense stationarity of mobile MIMO radio channels," *IEEE Transactions on Vehicular Technology*, vol. 57, no. 2, pp. 704–714, Mar. 2008.

[42] T. W. C. Brown, S. R. Saunders, S. Stavrou, and M. Fiacco, "Characterization of polarization diversity at the mobile," *IEEE Transactions on Vehicular Technology*, vol. 56, no. 5, pp. 2440–2447, Sep. 2007.

[43] J. Weitzen and M. Wallace, "Analysis of diversity performance of space diversity and cross polarization for PCS base stations," in *Proc. IEEE International Symposium on Personal, Indoor and Mobile Radio Communications (PIMRC '98)*, vol. 1, Sep. 8–11, 1998, pp. 293–297.

[44] F. Lotse, J.-E. Berg, U. Forssen, and P. Idahl, "Base station polarization diversity reception in macrocellular systems at 1800 MHz," in *Proc. IEEE 46th Vehicular Technology Conference 'Mobile Technology for the Human Race'*, vol. 3, Apr. 28–May 1, 1996, pp. 1643–1646.

[45] M. T. Ivrlac and J. A. Nossek, "Quantifying diversity and correlation in Rayleigh fading MIMO communication systems," in *Proc. 3rd IEEE International Symposium on Signal Processing and Information Technology ISSPIT 2003*, Dec. 14–17, 2003, pp. 158–161.

[46] T. J. Willink, "Characteristics of urban vehicular MIMO channels at different frequencies," in *Proc. 3rd European Conference on Antennas and Propagation EuCAP 2009*, Mar. 23–27, 2009, pp. 645–649.

[47] H. Van Trees, *Optimum Array Processing (Detection, Estimation, and Modulation Theory, Part IV)*. John Wiley & Sons, 2002.

[48] P. Kyritsi, D. C. Cox, R. A. Valenzuela, and P. W. Wolniansky, "Correlation analysis based on MIMO channel measurements in an indoor environment," *IEEE Journal on Selected Areas in Communications*, vol. 21, no. 5, pp. 713–720, Jun. 2003.

[49] V. R. Anreddy and M. A. Ingram, "Antenna selection for compact dual-polarized MIMO systems with linear receivers," in *Proc. IEEE Global Telecommunications Conference GLOBECOM '06*, Nov. 2006, pp. 1–6.

[50] T. B. Sorensen, A. O. Nielsen, P. E. Mogensen, M. Tolstrup, and K. Steffensen, "Performance of two-branch polarisation antenna diversity in an operational GSM network," in *Proc. 48th IEEE Vehicular Technology Conference VTC 98*, vol. 2, May 18–21, 1998, pp. 741–746.

[51] H. Asplund, J.-E. Berg, F. Harrysson, J. Medbo, and M. Riback, "Propagation characteristics of polarized radio waves in cellular communications," in *Proc. VTC-2007 Fall Vehicular Technology Conference 2007 IEEE 66th*, Sep. 2007, pp. 839–843.

[52] V. Erceg, P. Soma, D. S. Baum, and A. J. Paulraj, "Capacity obtained from multiple-input multiple-output channel measurements in fixed wireless environments at 2.5 GHz," in *Proc. IEEE International Conference on Communications ICC 2002*, vol. 1, Apr. 28–May 2, 2002, pp. 396–400.

[53] P. W. Wolniansky, G. J. Foschini, G. D. Golden, and R. A. Valenzuela, "V-BLAST: an architecture for realizing very high data rates over the rich-scattering wireless channel," in *Proc. URSI International Symposium on Signals, Systems, and Electronics ISSSE 98*, Sep. 29–Oct. 2, 1998, pp. 295–300.

Appendix A

Measured Correlation Time Series

The following sections contain the time series of correlation coefficients measured on each of the measurement routes. The top and middle plots show the spatial correlations of the VP and HP channels respectively. The bottom plots show the cross-polar correlation coefficients among the VP and HP subchannels. In each plot, the lines show the correlations between a different pair of subchannels measured at the receiver with respect to a single transmit element.

A.1 Laurier Avenue

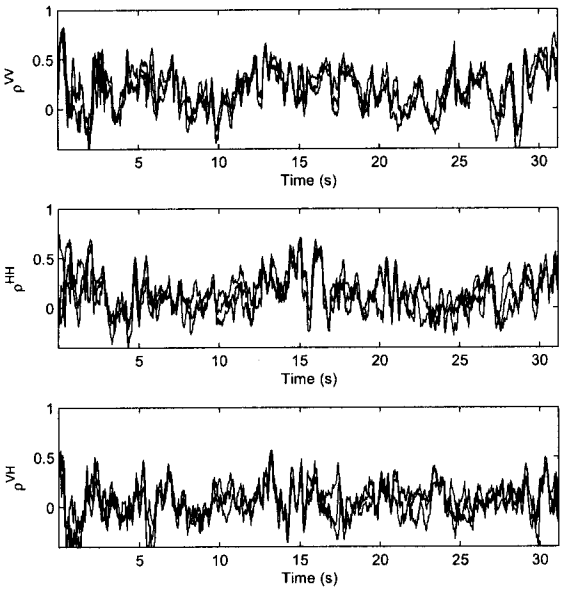

Figure A.1: Laurier Ave. DSA correlations from transmitter 1

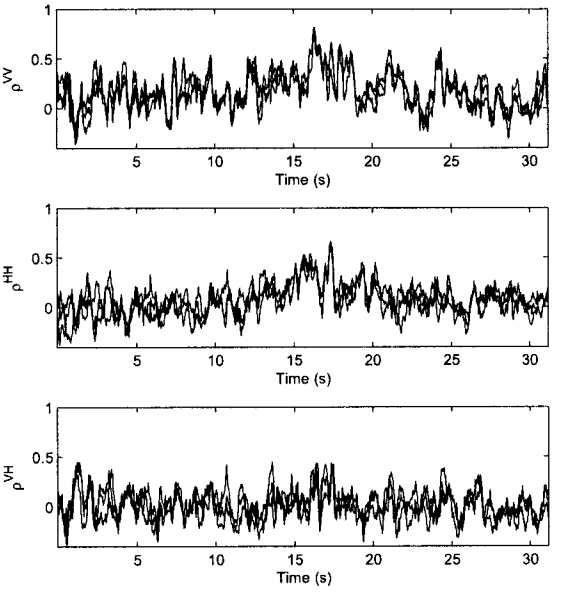

Figure A.2: Laurier Ave. PSA correlations from transmitter 1

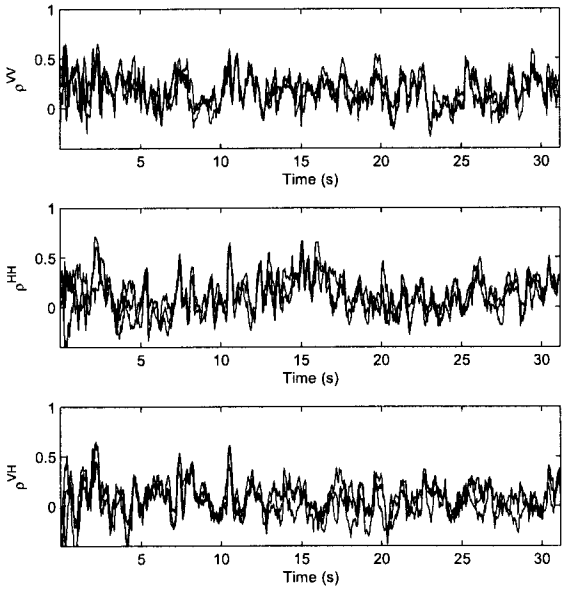

Figure A.3: Laurier Ave. DSA correlations from transmitter 2

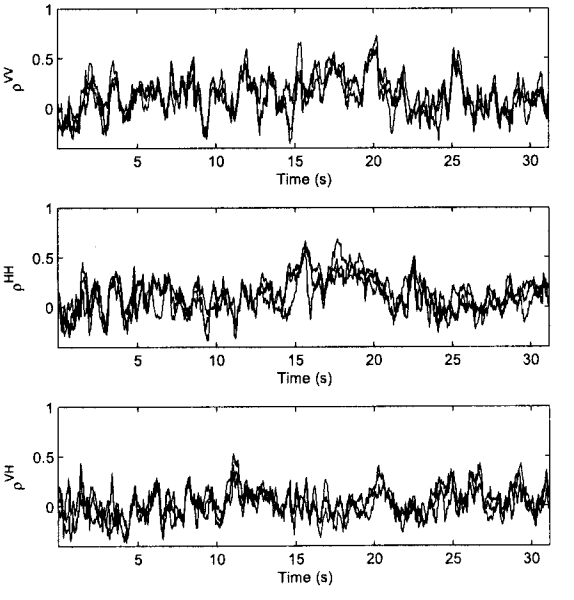

Figure A.4: Laurier Ave. PSA correlations from transmitter 2

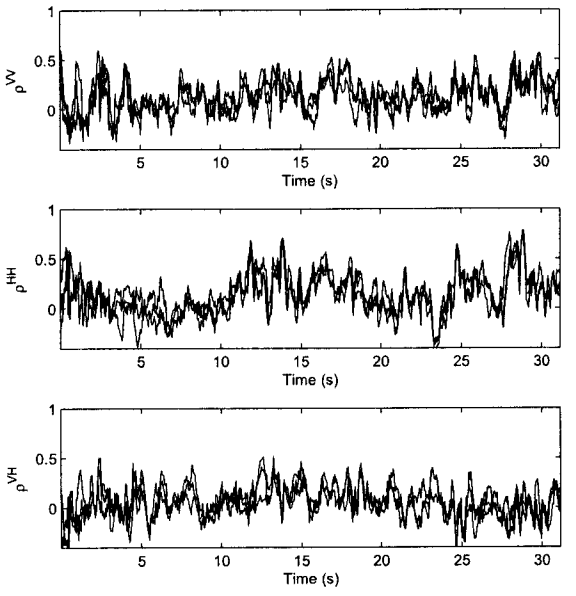

Figure A.5: Laurier Ave. DSA correlations from transmitter 3

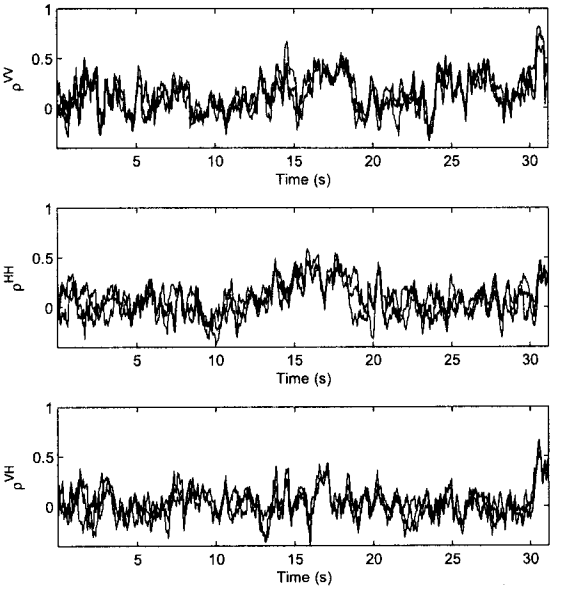

Figure A.6: Laurier Ave. PSA correlations from transmitter 3

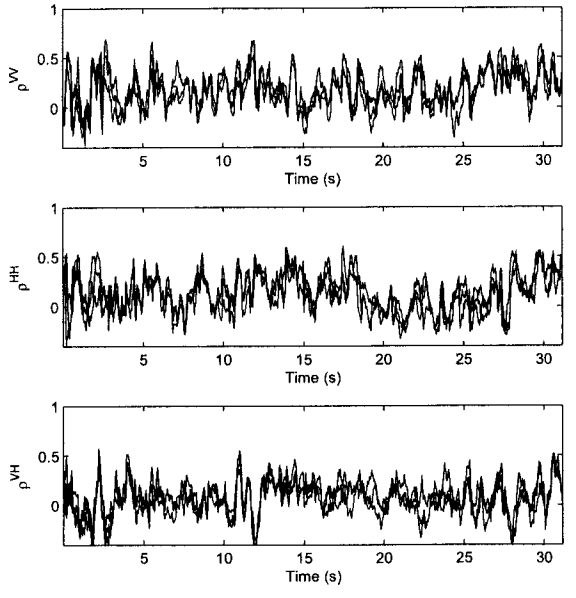

Figure A.7: Laurier Ave. DSA correlations from transmitter 4

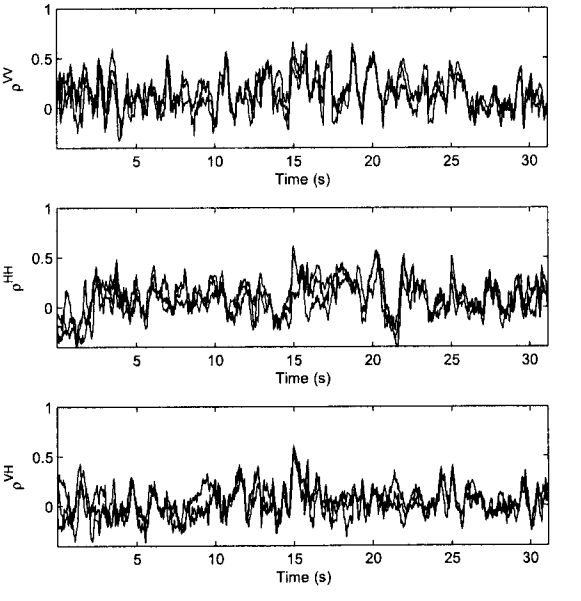

Figure A.8: Laurier Ave. PSA correlations from transmitter 4

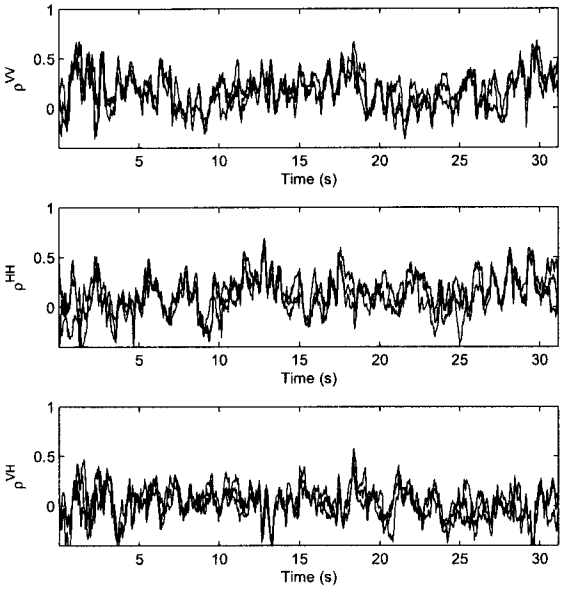

Figure A.9: Laurier Ave. DSA correlations from transmitter 5

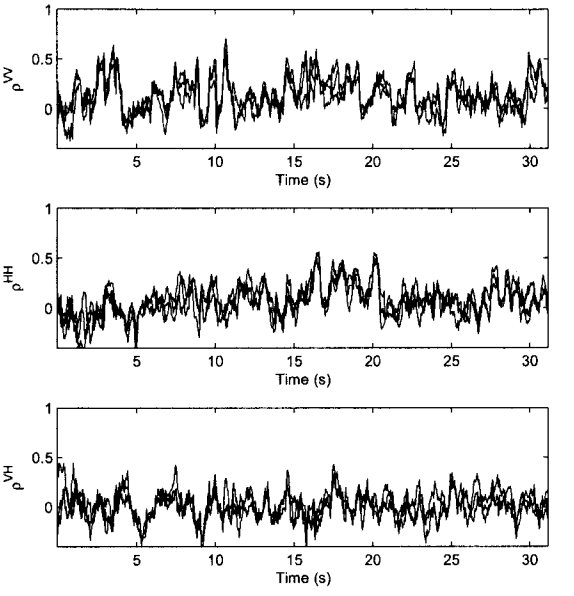

Figure A.10: Laurier Ave. PSA correlations from transmitter 5

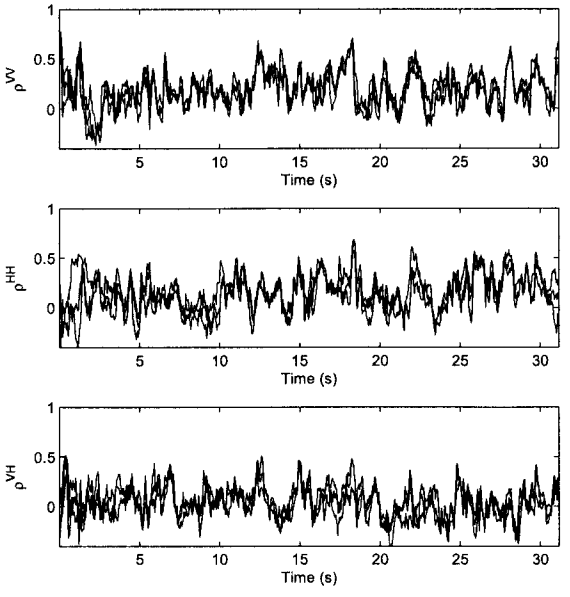

Figure A.11: Laurier Ave. DSA correlations from transmitter 6

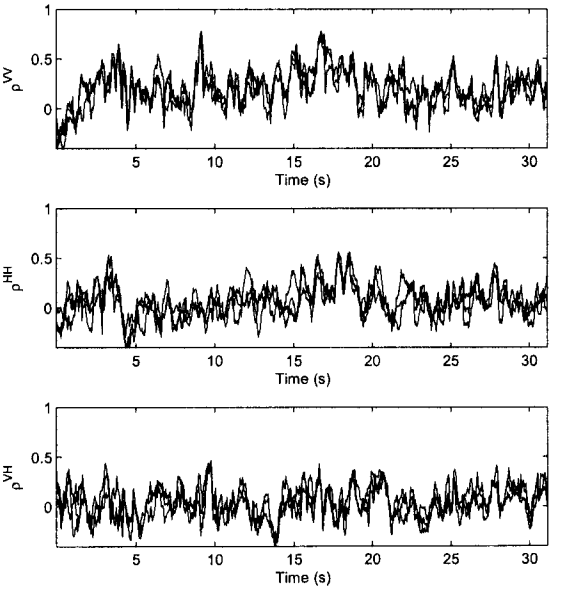

Figure A.12: Laurier Ave. PSA correlations from transmitter 6

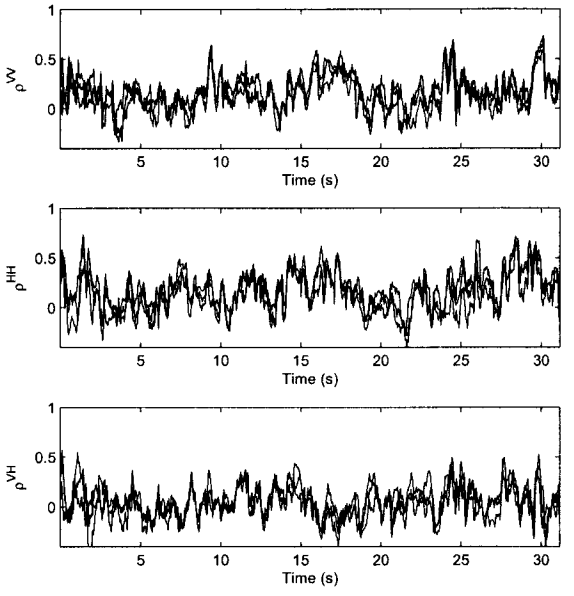

Figure A.13: Laurier Ave. DSA correlations from transmitter 7

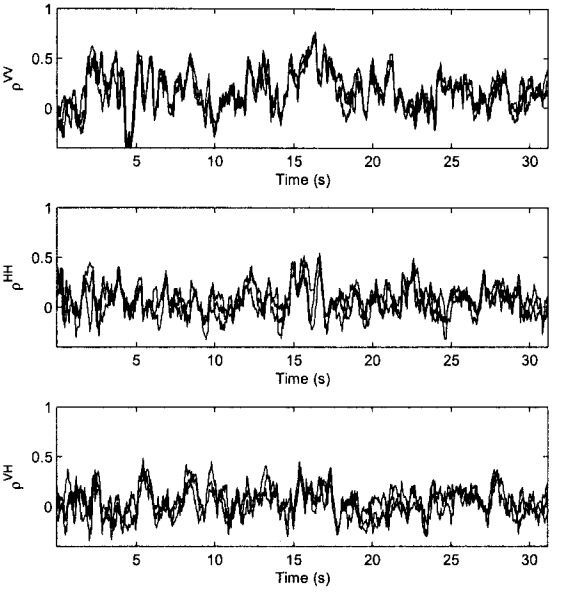

Figure A.14: Laurier Ave. PSA correlations from transmitter 7

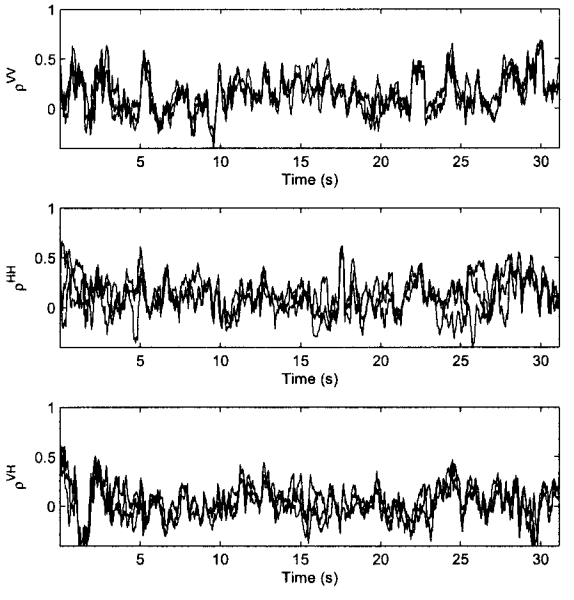

Figure A.15: Laurier Ave. DSA correlations from transmitter 8

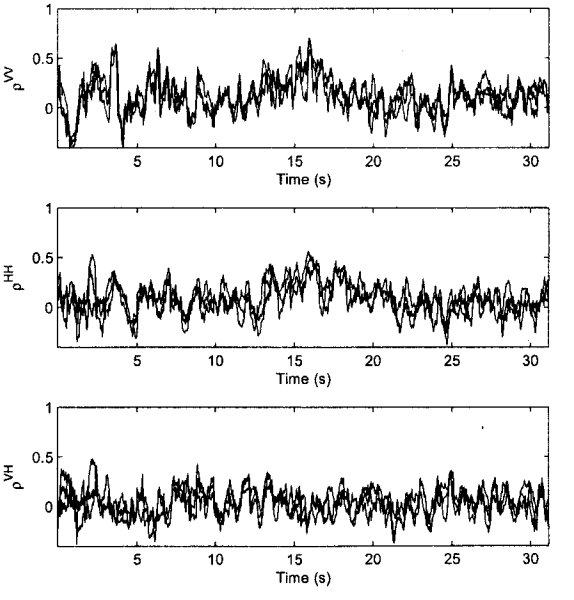

Figure A.16: Laurier Ave. PSA correlations from transmitter 8

A.2 Slater Street

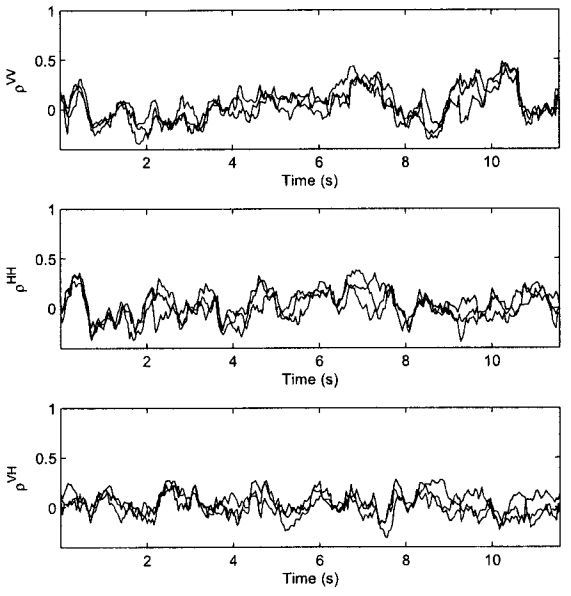

Figure A.17: Slater St. DSA correlations from transmitter 1

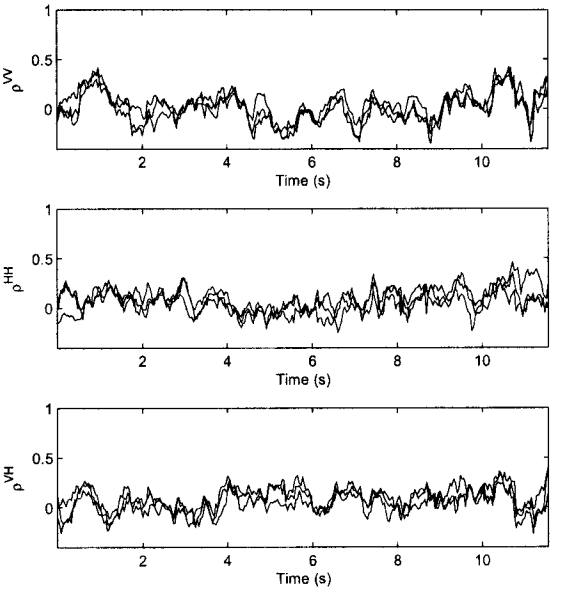

Figure A.18: Slater St. PSA correlations from transmitter 1

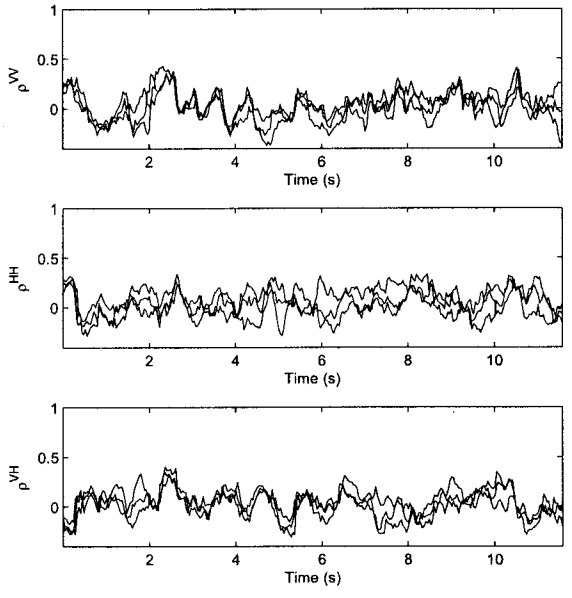

Figure A.19: Slater St. DSA correlations from transmitter 2

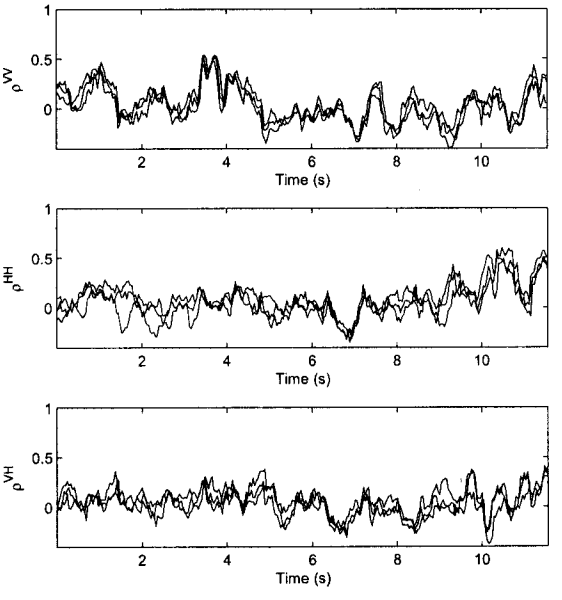

Figure A.20: Slater St. PSA correlations from transmitter 2

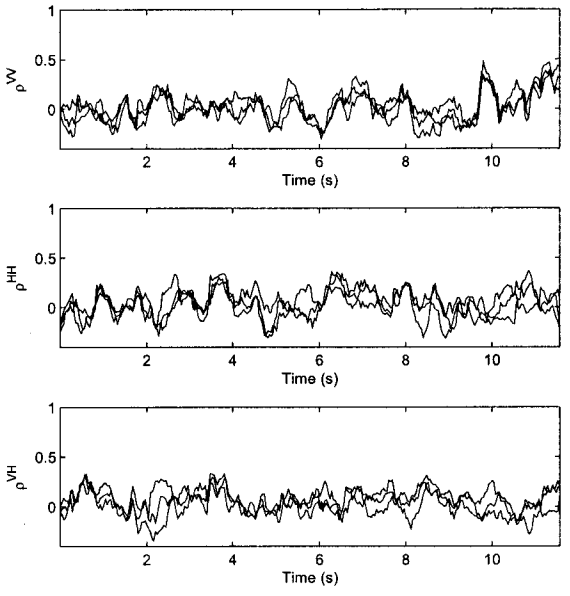

Figure A.21: Slater St. DSA correlations from transmitter 3

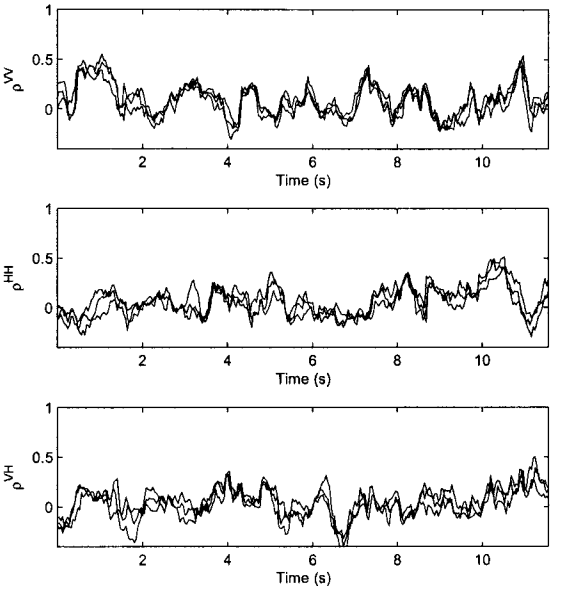

Figure A.22: Slater St. PSA correlations from transmitter 3

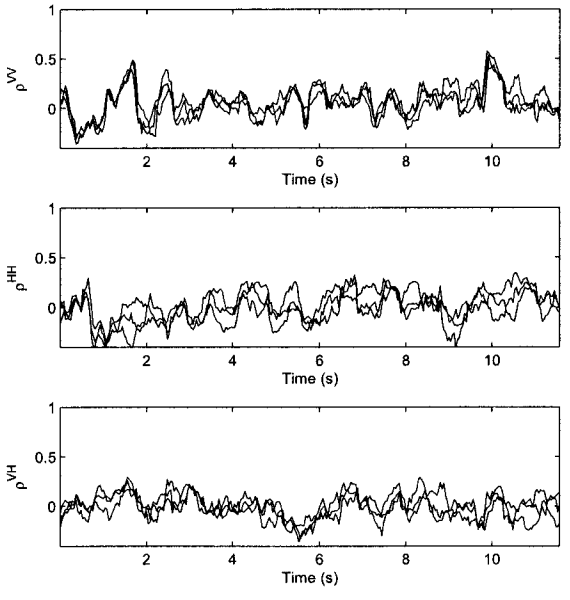

Figure A.23: Slater St. DSA correlations from transmitter 4

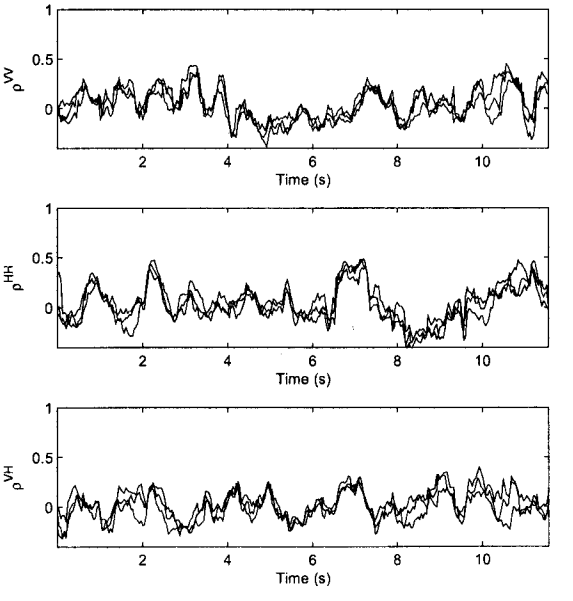

Figure A.24: Slater St. PSA correlations from transmitter 4

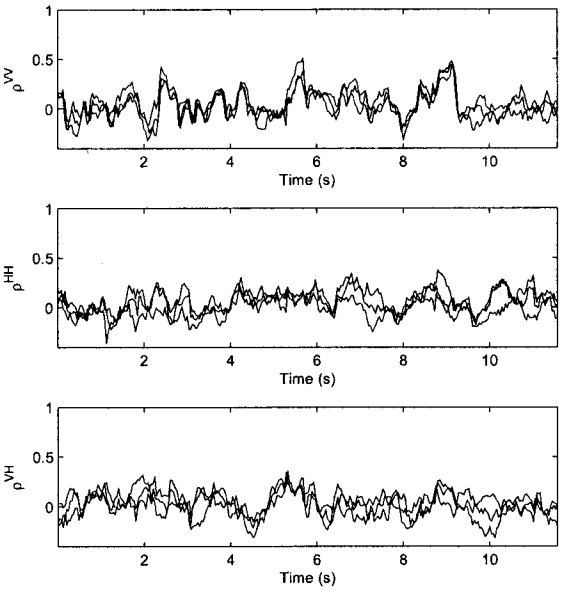

Figure A.25: Slater St. DSA correlations from transmitter 5

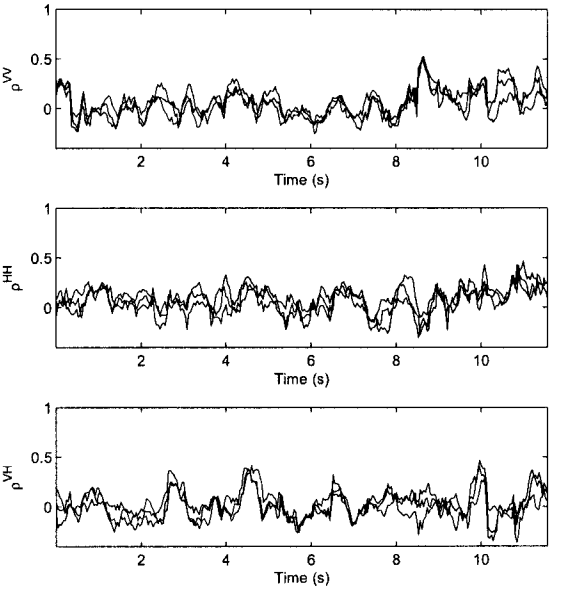

Figure A.26: Slater St. PSA correlations from transmitter 5

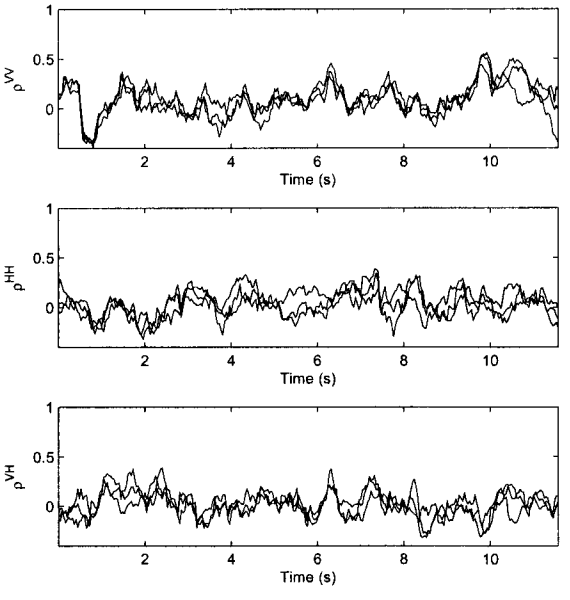

Figure A.27: Slater St. DSA correlations from transmitter 6

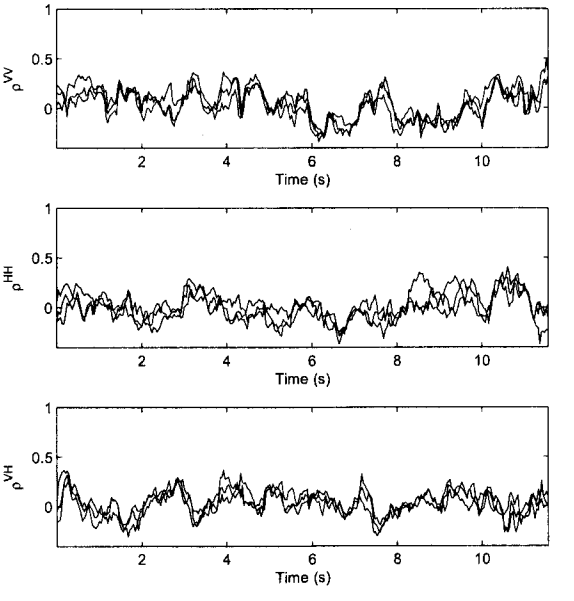

Figure A.28: Slater St. PSA correlations from transmitter 6

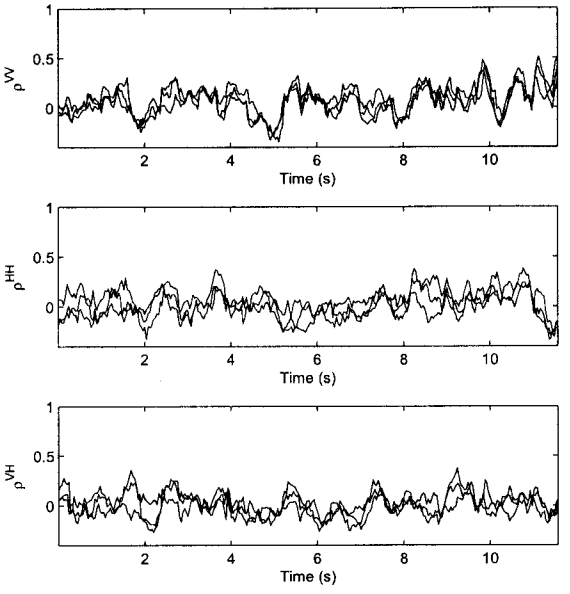

Figure A.29: Slater St. DSA correlations from transmitter 7

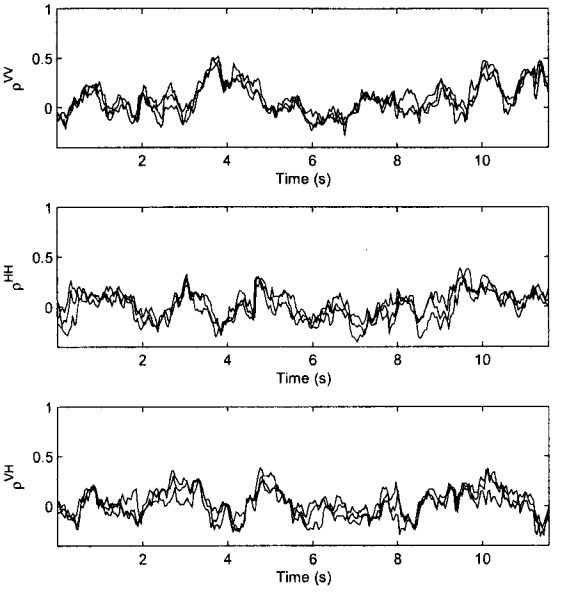

Figure A.30: Slater St. PSA correlations from transmitter 7

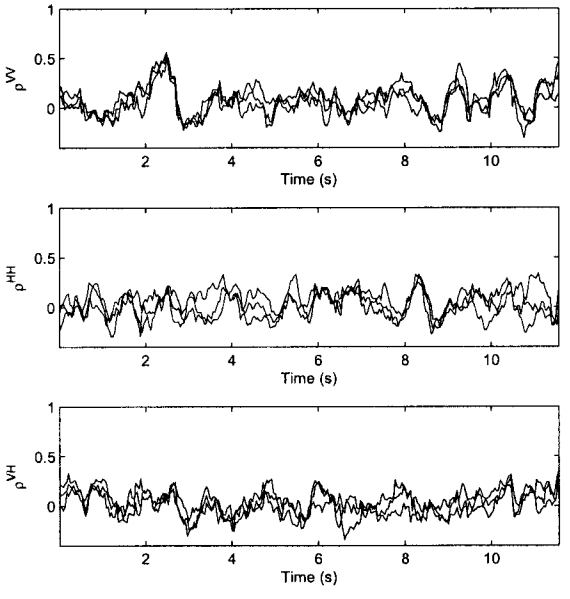

Figure A.31: Slater St. DSA correlations from transmitter 8

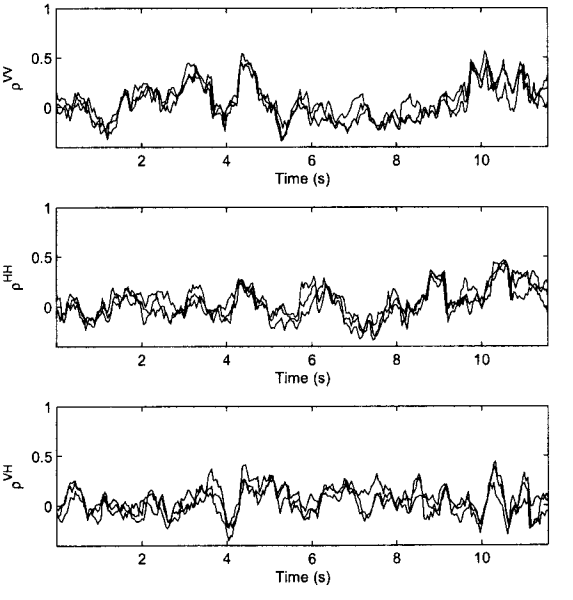

Figure A.32: Slater St. PSA correlations from transmitter 8

A.3 Kent Street

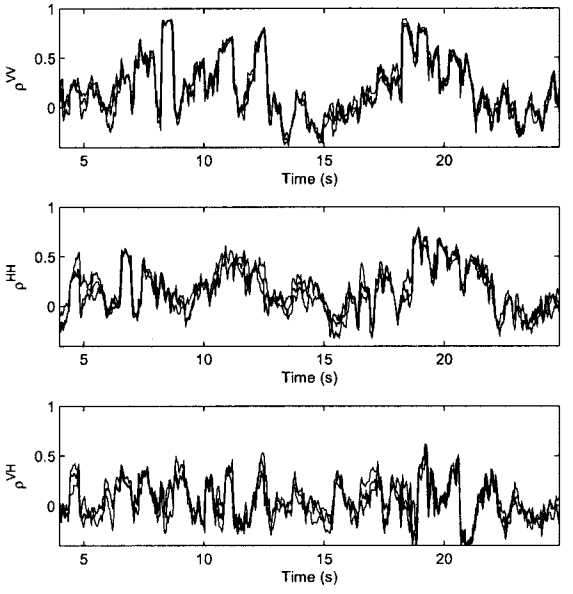

Figure A.33: Kent St. DSA correlations from transmitter 1

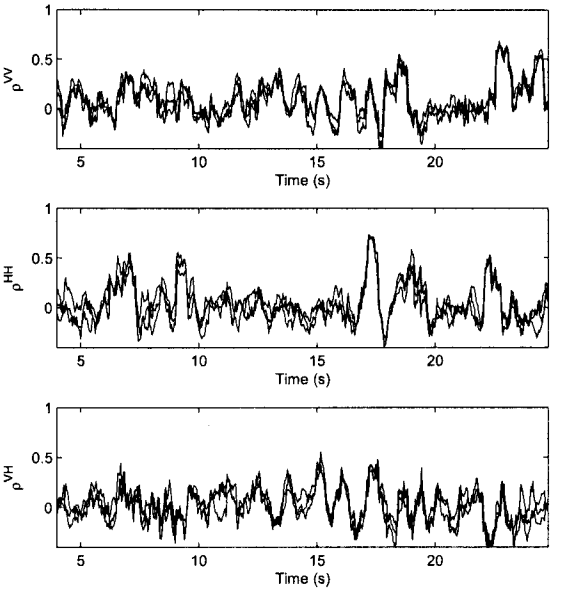

Figure A.34: Kent St. PSA correlations from transmitter 1

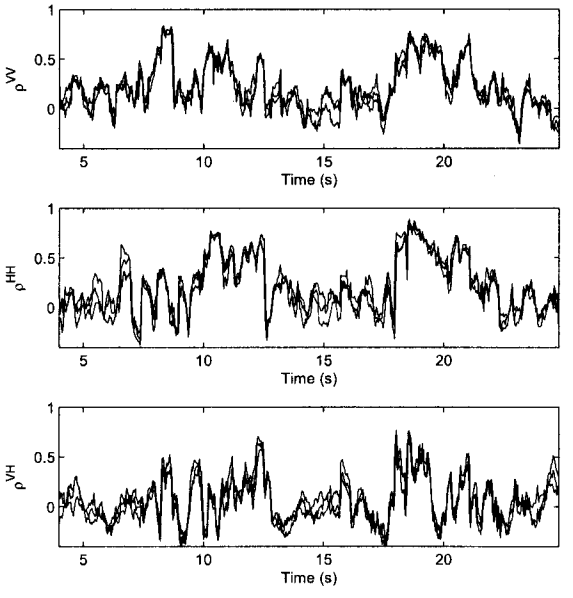

Figure A.35: Kent St. DSA correlations from transmitter 2

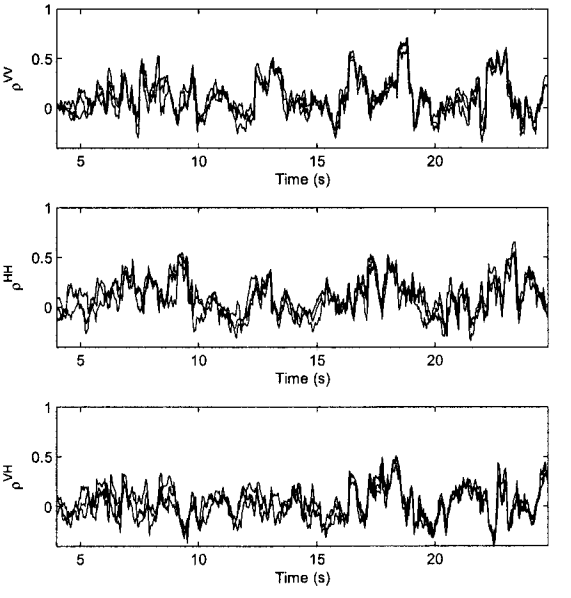

Figure A.36: Kent St. PSA correlations from transmitter 2

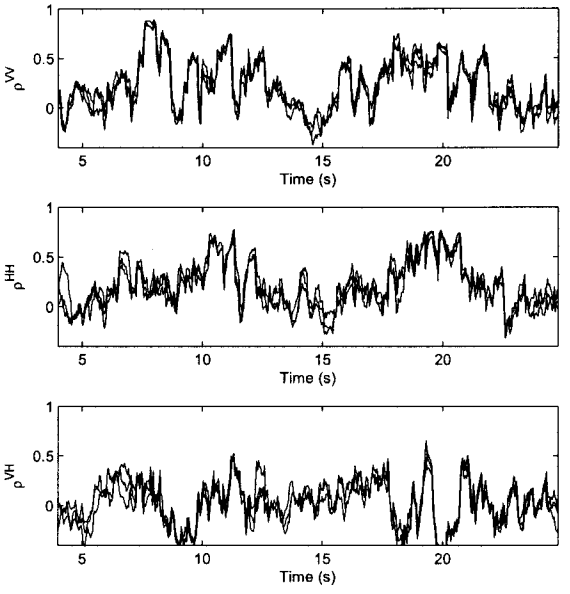

Figure A.37: Kent St. DSA correlations from transmitter 3

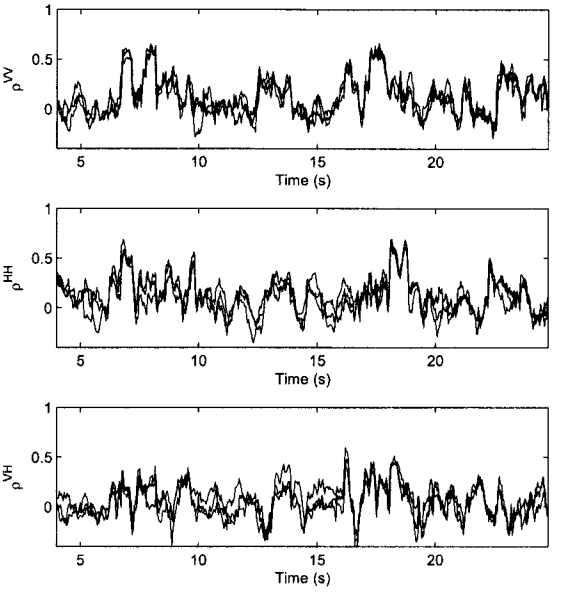

Figure A.38: Kent St. PSA correlations from transmitter 3

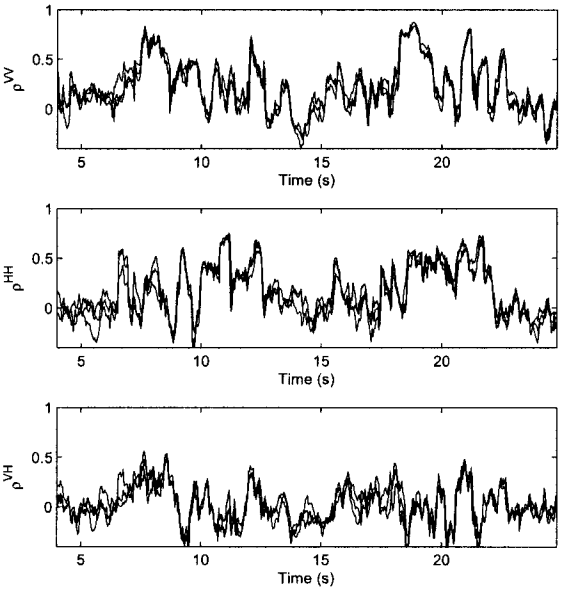

Figure A.39: Kent St. DSA correlations from transmitter 4

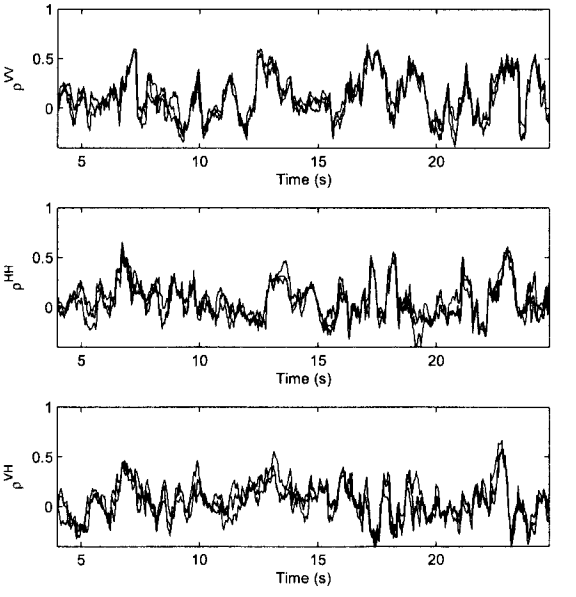

Figure A.40: Kent St. PSA correlations from transmitter 4

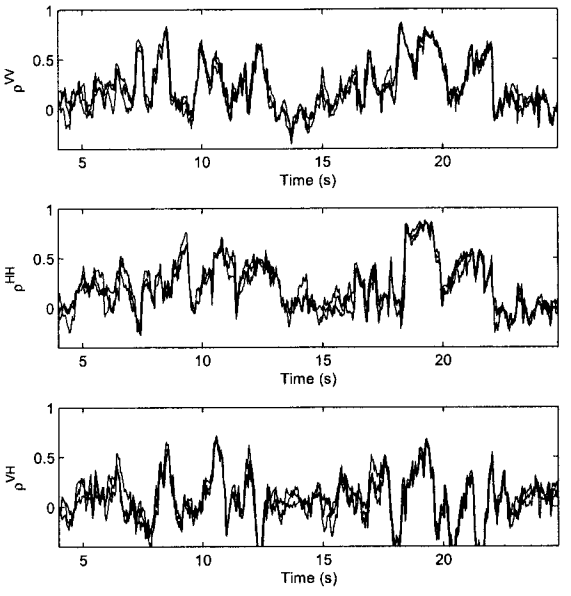

Figure A.41: Kent St. DSA correlations from transmitter 5

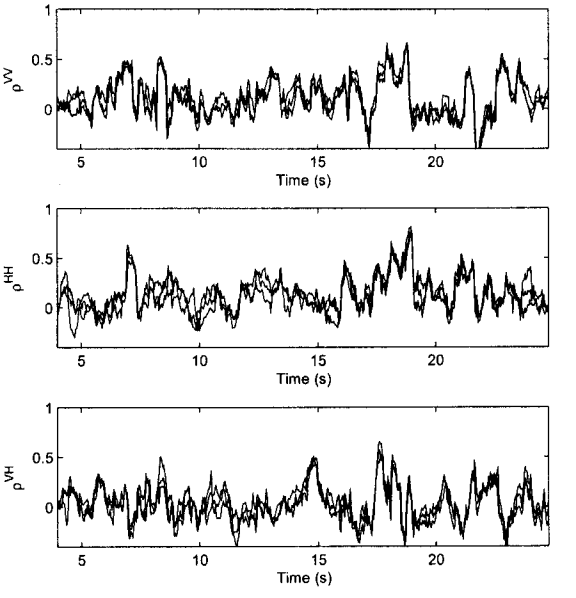

Figure A.42: Kent St. PSA correlations from transmitter 5

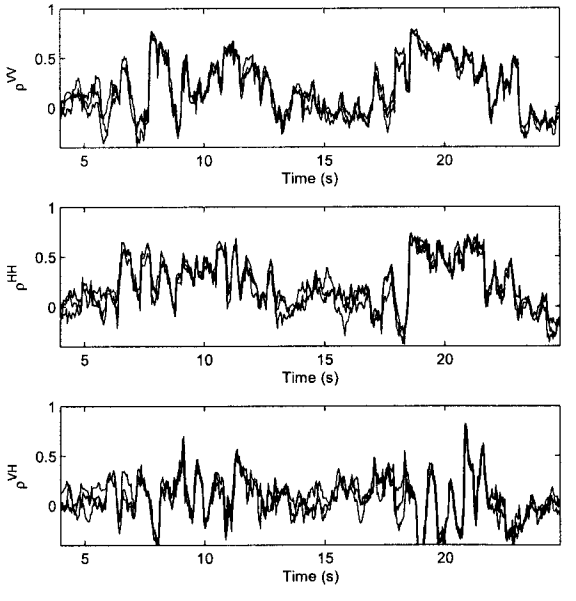

Figure A.43: Kent St. DSA correlations from transmitter 6

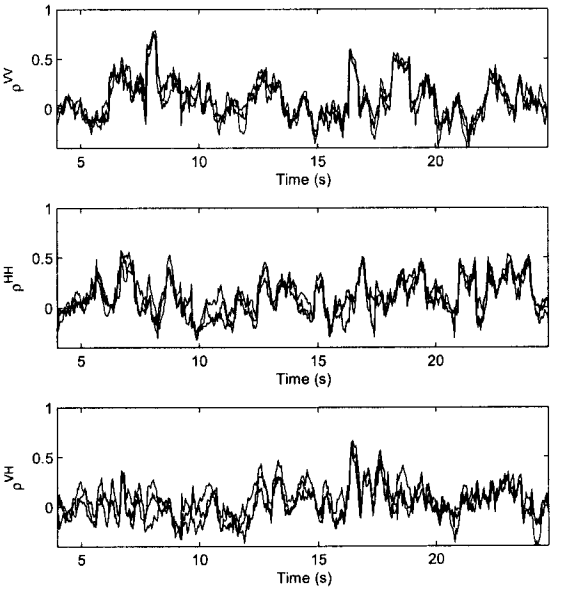

Figure A.44: Kent St. PSA correlations from transmitter 6

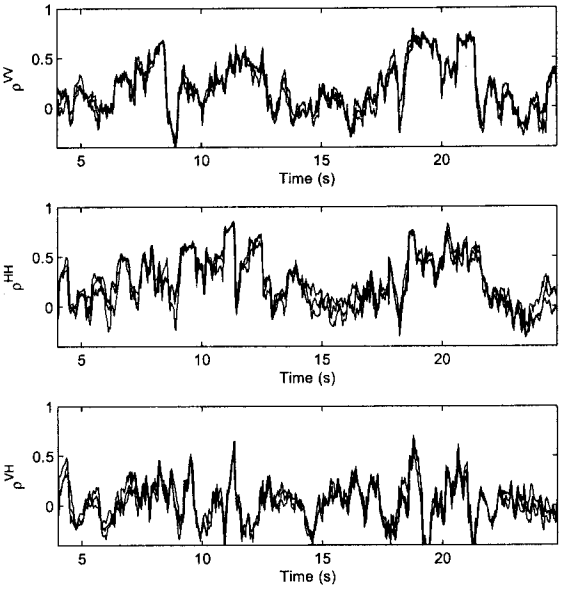

Figure A.45: Kent St. DSA correlations from transmitter 7

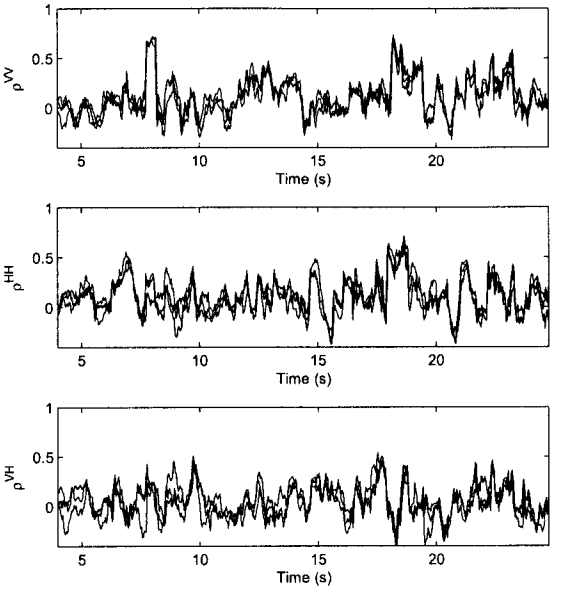

Figure A.46: Kent St. PSA correlations from transmitter 7

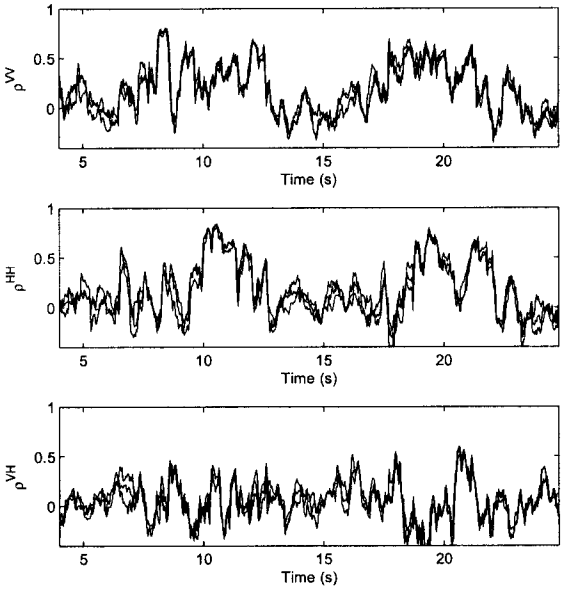

Figure A.47: Kent St. DSA correlations from transmitter 8

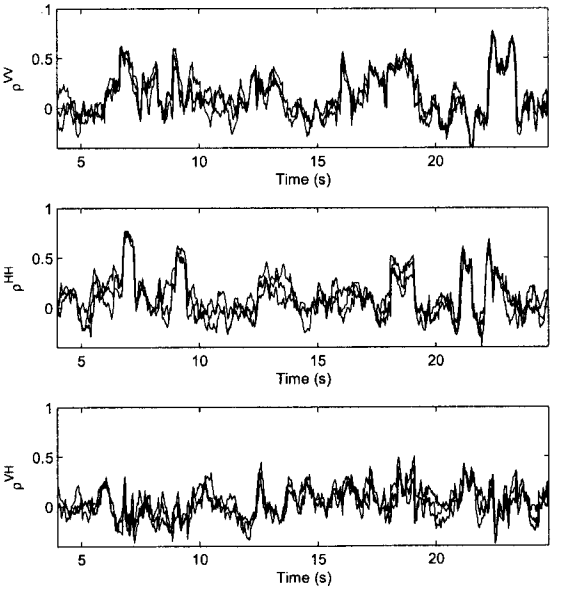

Figure A.48: Kent St. PSA correlations from transmitter 8

A.4 Bank Street

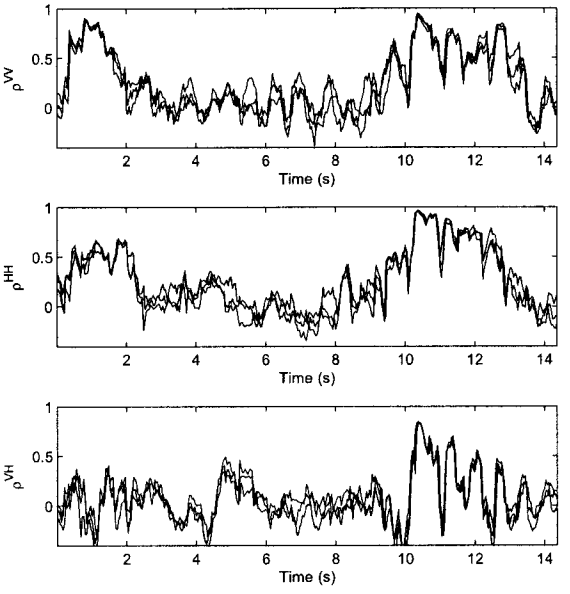

Figure A.49: Bank St. DSA correlations from transmitter 1

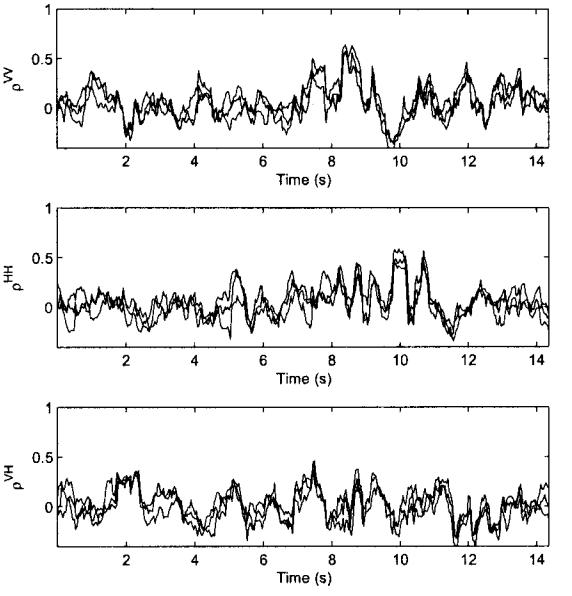

Figure A.50: Bank St. PSA correlations from transmitter 1

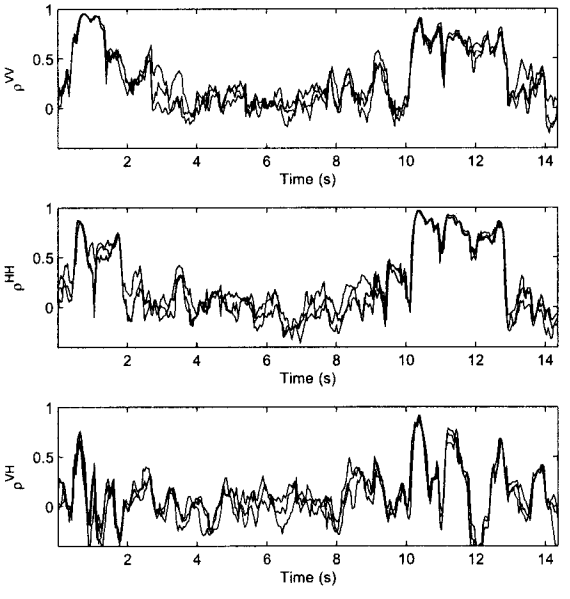

Figure A.51: Bank St. DSA correlations from transmitter 2

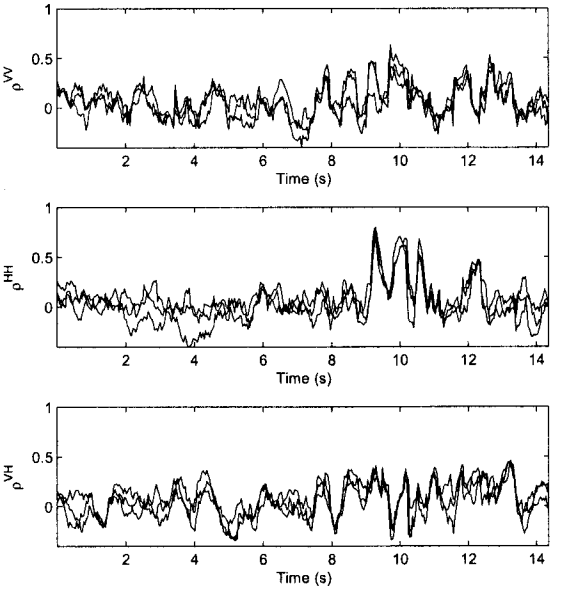

Figure A.52: Bank St. PSA correlations from transmitter 2

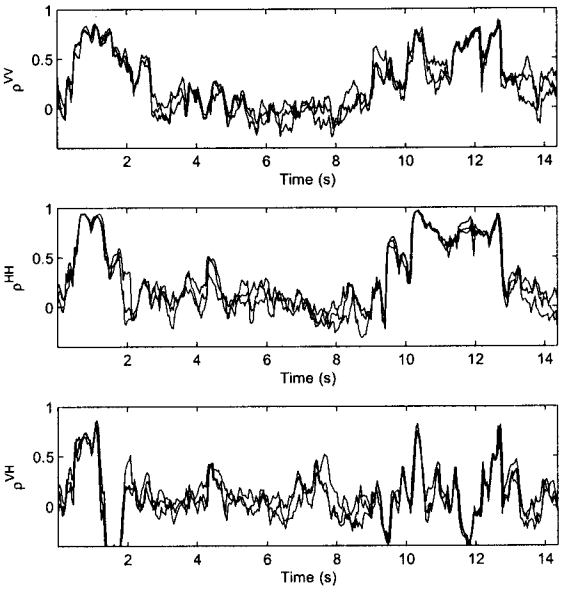

Figure A.53: Bank St. DSA correlations from transmitter 3

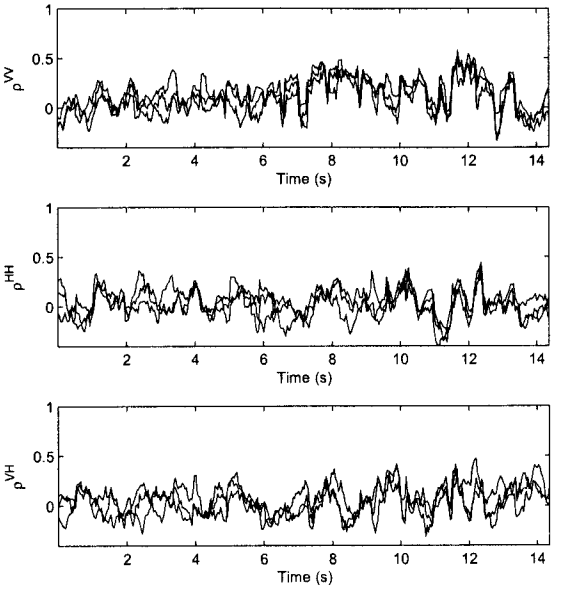

Figure A.54: Bank St. PSA correlations from transmitter 3

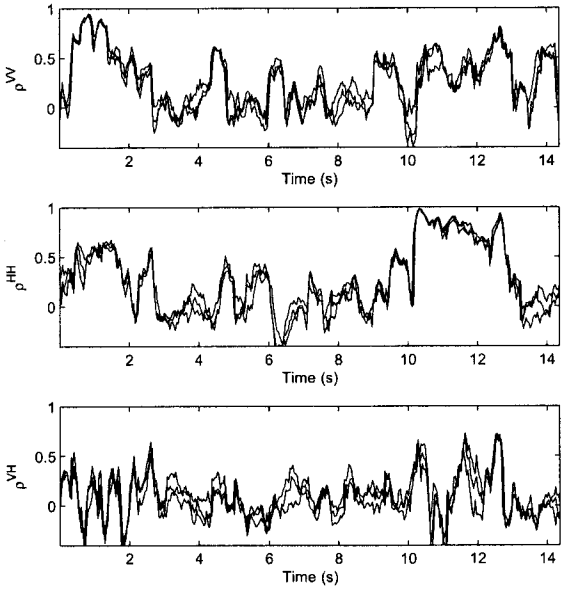

Figure A.55: Bank St. DSA correlations from transmitter 4

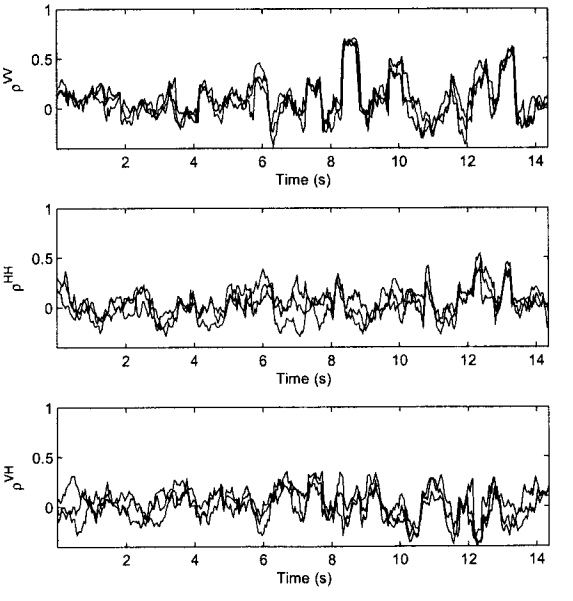

Figure A.56: Bank St. PSA correlations from transmitter 4

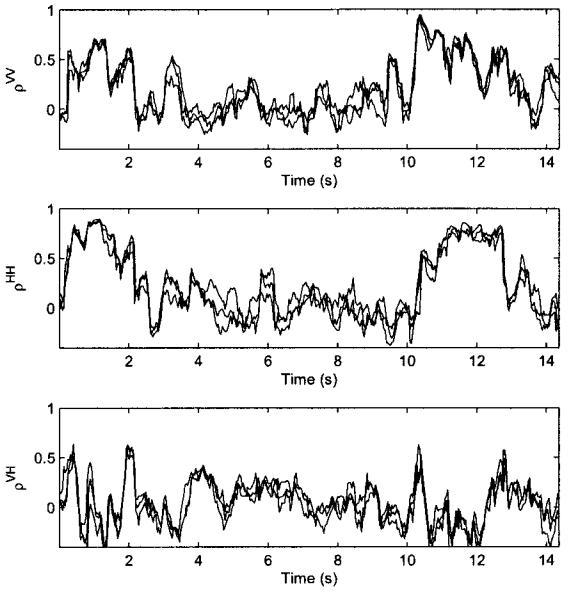

Figure A.57: Bank St. DSA correlations from transmitter 5

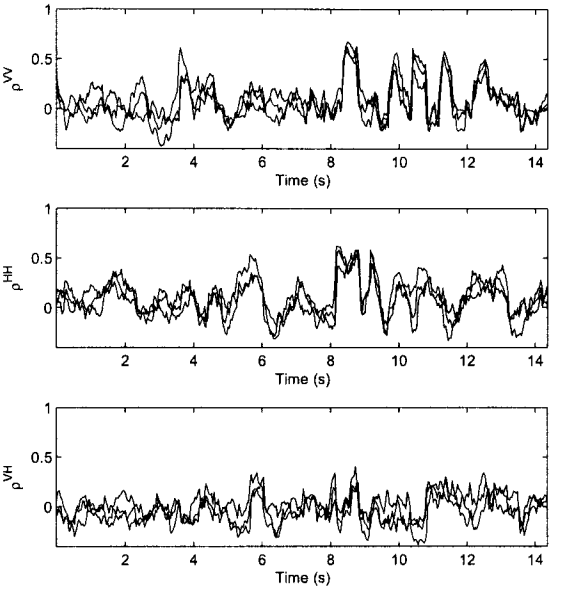

Figure A.58: Bank St. PSA correlations from transmitter 5

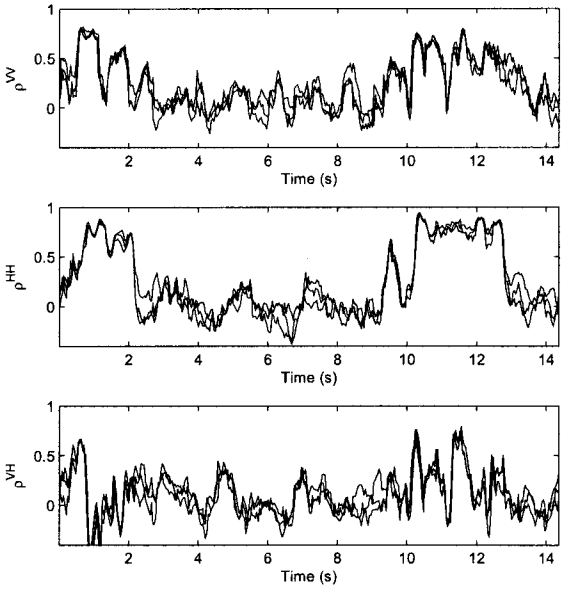

Figure A.59: Bank St. DSA correlations from transmitter 6

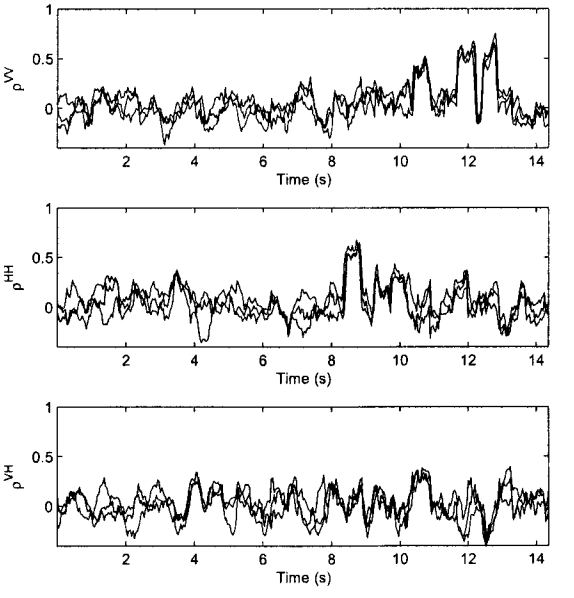

Figure A.60: Bank St. PSA correlations from transmitter 6

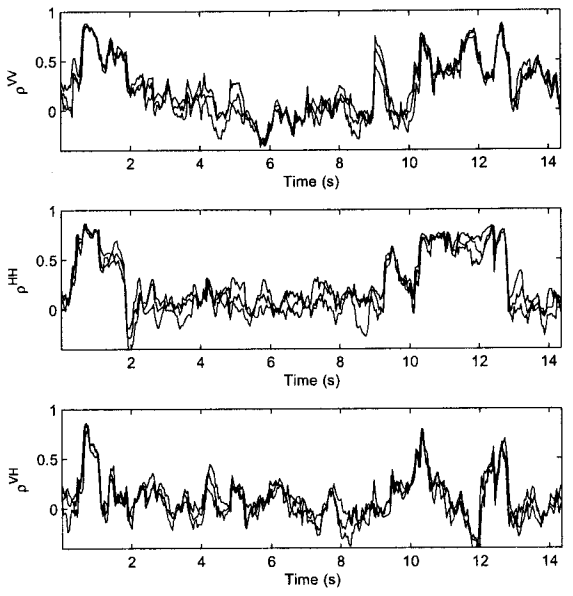

Figure A.61: Bank St. DSA correlations from transmitter 7

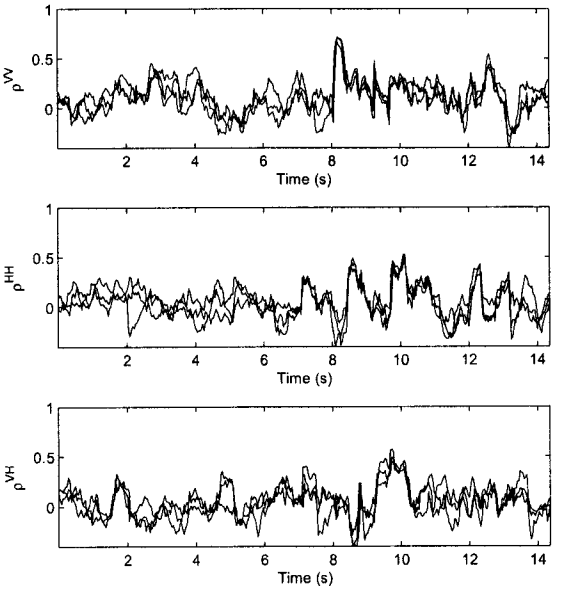

Figure A.62: Bank St. PSA correlations from transmitter 7

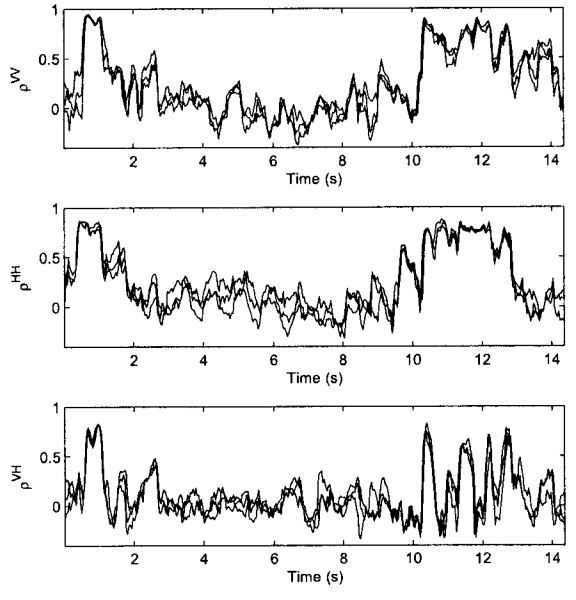

Figure A.63: Bank St. DSA correlations from transmitter 8

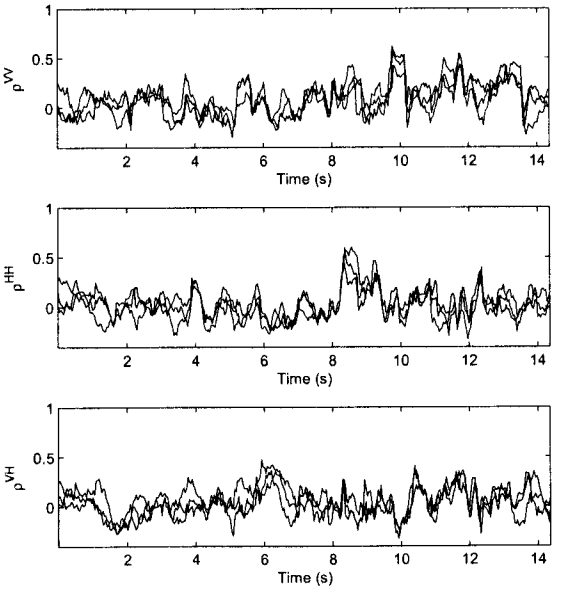

Figure A.64: Bank St. PSA correlations from transmitter 8